

DEVELOPMENT OF A THOMSON SCATTERING
DIAGNOSTIC ON A PULSED POWER MACHINE
AND ITS USE IN STUDYING LABORATORY
PLASMA JETS FOCUSING ON THE EFFECT OF
CURRENT POLARITY

A Dissertation

Presented to the Faculty of the Graduate School
of Cornell University

in Partial Fulfillment of the Requirements for the Degree of
Doctor of Philosophy

by

Jacob Thomas Banasek

December 2019

© 2019 Jacob Thomas Banasek

ALL RIGHTS RESERVED

DEVELOPMENT OF A THOMSON SCATTERING DIAGNOSTIC ON A
PULSED POWER MACHINE AND ITS USE IN STUDYING LABORATORY
PLASMA JETS FOCUSING ON THE EFFECT OF CURRENT POLARITY

Jacob Thomas Banasek, Ph.D.

Cornell University 2019

This research primarily focused on the development of a collective Thomson scattering system for experiments on a 1 MA 100 ns pulsed power generator at Cornell University (COBRA). This diagnostic is capable of determining, at a minimum, the electron temperature, electron density and the flow velocity in the plasma. It was used in experiments on plasma jets created using a radial Al foil (thin disk of foil) load on COBRA. These jets served as a good load as they were long-lasting and at the center of the experimental chamber. The first set of experiments explored the rotation of the jet when an external magnetic field is applied and found the jet to be rotating at about 20 km/s. During these experiments, it was discovered that the Thomson scatter laser energy (10 J) was sufficient to heat the 20 eV jet plasma by inverse bremsstrahlung. While this did not affect the velocity measurements, it did significantly affect the measured temperature of the plasma. To better study this perturbation, a streak camera was set up to measure the changing temperature during the laser pulse. The plasma was found to be heated from about 20 to 80 eV in the first half of the laser pulse, before cooling down due to the expansion of the plasma. We also started developing a system to record the high-frequency Thomson scattering spectral feature to measure the density of the plasma. This showed some initial promising results and suggested densities of at least $5 \times 10^{18} \text{ cm}^{-3}$. Finally, using

low enough laser energy to avoid laser heating of the plasma, the effect of current polarity on the plasma jets was studied experimentally. It was found that while jets with a radial outward current flow were denser and wider than jets with a radial inward current, both jets had a similar electron temperature. These experiments were also compared to extended magnetohydrodynamic (XMHD) simulations. While experimental jets had about the same width as those in the simulation, they were found to be slightly colder and significantly less dense than the simulations.

BIOGRAPHICAL SKETCH

Jacob Thomas Banasek was born the day after October 3 nineteen ninety in Glendale Heights, Illinois to Mark and Christina Banasek. His younger brother, Sam, was born three years later the day after December 15. Shortly thereafter, the 2 of them, along with their parents, moved to Wellington, Ohio, where they grew up. There, Jacob went to Black River School District, which he graduated at the age of 18. He then attended Wright State University and earned a BS degree in engineering physics with a minor in computer science. Jacob then decided to attend Cornell University to earn a Ph.D. in applied physics and was planning to research optics. Shortly after choosing Cornell, however, he was approached by Dave Hammer about the Laboratory of Plasma Studies. Jacob decided to join the lab, and this work is about his research there.

In his free time, Jacob enjoys playing his saxophone, about any type of game (board, card, video), and solving puzzles. 1 particular interest of his is puzzle hunts, where about anything can be a puzzle. For example, the rest of the thesis is not a puzzle (except for the kind that science gives us).

To my grandfather, Dr. Arthur W. Moore (AKA Papacs).
Even though you're not here anymore, I have followed in your footsteps.

ACKNOWLEDGEMENTS

First off, I would like to thank my adviser, Prof. Dave Hammer, for introducing me to the field of plasma physics and the Laboratory of Plasma Studies. Without his recruitment and encouragement to join the lab, I would never have joined this field. Thanks for all the guidance enabling me to grow as a researcher and scientist. And finally, thanks for all the time helping me become a better writer and editing my numerous (but at least sometimes funny) typos.

Thanks to my other committee members, Prof. Lovelace and Prof. Loring, for being on my committee and supporting my minors in applied physics and applied math, respectively.

Thanks to Prof. Bruce Kusse for numerous discussions on the fundamentals of Thomson scattering, which I think helped both of our understanding. Never forget the funky k-vectors.

Thanks to Prof. Charlie Seyler, whose work with PERSEUS allowed me to make comparisons between experiments and simulations. I appreciated the opportunity to dabble a little with the simulations, but that you ran and improved the code when we noticed significant differences between the models and the experiments.

Thanks to Dr. Tania Shelkovenko and Dr. Sergei Pikuz for all of their help in learning how to do spectroscopy experiments, which were the start of my research in the lab. Also thanks to Dr. John Greenly for all the help with various experiments.

Thanks to the amazing technical staff at the Laboratory of Plasma Studies. Thanks to Harry Wilhelm for running COBRA, and normally giving me short pulses, as well as being able to solve most issues in the lab. Thanks to Dr. Billy Potter for all the help with the diagnostics and making sure that the 10 J laser

worked, as I would not have a thesis without it. Thanks to Todd Blanchard for machining any needed parts. And, thanks to Dan Hawkes for all the help around the lab.

Thanks To Cindy VanOstrad for taking care of all the administrative stuff.

Thanks to Dr. Dustin Froula and his group at LLE for their openness to share their experiences in Thomson scattering, helping us to improve our system.

Thanks to all my fellow lab mates who made work an enjoyable experience. This includes but is not limited to: Jay Angel, Lavon Atoyan, Tom Byvank, Adam Cahill, Chiatai Chen, Phil de Grouchy, Ahmed Elshafiey, Joey Engelbrecht, Euan Freeman, Jason Hamilton, Nat Hamlin, Cad Hoyt, Sander Lavine, Jeff Musk, and Sophia Rocco.

Thanks to my Ithaca and Wright State friends who have made college and grad school an enjoyable experience. Especially to my group of AEP friends who went through the battle of grad school along with me.

And of course, a big thanks to my family for all their love and support and always pushing me to work hard and try my best.

Finally, I need to thank my funding sources, without who this work would not have been possible. This research was supported by NNSA Stewardship Sciences Academic Programs under DOE Cooperative Agreement - DE-NA0001836 and DE-NA0003764.

TABLE OF CONTENTS

Biographical Sketch	iii
Dedication	iv
Acknowledgements	v
Table of Contents	vii
List of Tables	ix
List of Figures	x
1 Introduction	1
1.1 Motivation	1
1.2 Outline	6
2 Experimental Platform	8
2.1 COBRA	8
2.2 Plasma Jets	9
2.3 Diagnostics	12
2.3.1 Extreme Ultraviolet Self-Emission Pinhole Cameras	12
2.3.2 Laser Interferometry and Shadowgraphy	14
2.3.3 Thomson Scattering	18
3 Thomson Scattering Theory	26
3.1 Overview	26
3.1.1 Salpeter Approximation	40
3.2 Electron Plasma Wave	44
3.2.1 Peak Separation	45
3.2.2 Peak Shape	46
3.3 Ion Acoustic Wave	48
3.3.1 Peak Shifts	48
3.3.2 Peak Separation	51
3.3.3 Peak Widths	53
3.3.4 Peak Intensities	56
3.4 Analysis Techniques	58
3.5 Spectral Fitting Techniques	61
3.5.1 Ion Acoustic Wave Fitting	62
3.5.2 Electron Plasma Wave Fitting	65
3.5.3 Error Bars	66
4 Plasma Jet Simulation Overview	70
4.1 Plasma Model	70
4.2 Simulation Method	73

5 Thomson Scattering Results	78
5.1 Jet Rotation Measurements	78
5.2 Preliminary Jet Heating	83
5.3 Time Resolved Jet Heating	86
5.3.1 Ti Results	92
5.4 Density Measurements	95
5.4.1 Ion Acoustic Wave Feature	96
5.4.2 Electron Plasma Wave Feature	99
5.5 Current Polarity Effects	108
5.5.1 Experimental Results	108
5.5.2 Comparison with Simulations	112
6 Conclusion	122
6.1 Conclusion	122
6.2 Next Steps	125
6.2.1 Thomson Scattering Development	125
6.2.2 Thomson Scattering on Plasma Jets	129
A Code for Thomson Scattering Profile	132
B Code for Super Gaussian Thomson Scattering Profile	140
Bibliography	151

LIST OF TABLES

3.1	Table of the FWHM for the parameters that were varied for each synthetic spectrum for the MC error bar calculations. Each of the columns represents a different fitting model. All these fitting models assumed that the plasma was non-collisional and Maxwellian. The N/A parts of the table do not apply to that fitting model as the parameters in that row are used in the model to find the best fit for each synthetic spectrum.	67
3.2	Table of the values used for parameters to try to find a possible range for T_e	69

LIST OF FIGURES

2.1	CAD drawing of COBRA.	9
2.2	Picture of radial foil load hardware in reverse current polarity. The foil is held in the cathode ring and the anode pin is slightly higher than the ring in order to make good contact with the foil. In order to switch to standard polarity, the pieces labeled 1 and 2 are aligned (instead of being at 90°) and the outside ring is connected to the anode by 4 posts.	10
2.3	Schematic of the plasma jet created from a radial foil in SP current polarity	11
2.4	Schematic of the general setup for XUV self-emission pinholes.	14
2.5	Sample image of the fringe patterns before a shot (a) and during a shot (b). These were taken from a large shift shearing interferometer configuration.	15
2.6	Schematic of a Mach-Zender interferometer.	17
2.7	Diagram of the optics and path used to delay part of the laser beam. The path length difference, or the time delay, between paths A and B is controlled by the distance between the 'X' labeled optics and the 'Y' labeled optics. The orange part of the beam indicates that the infrared (IR) and the green beams are both present. The upper two optics both allow the IR beam (in red) to pass, thereby separating it from the frequency doubled green beam. The two beam dumps collect the unused IR beam and the unused half of the green beam. Reproduced from [2], with the permission of AIP Publishing.	20
2.8	A schematic of a Czerny-Turner spectrometer [44].	23
2.9	Schematic of the setup to allow light from two fibers to enter the spectrometer. This setup is shown with four fibers being blocked by the tape.	25
3.1	Figure of a single particle scattering system.	27
3.2	A plot showing the real and imaginary parts of W , and where the resonances will occur for an arbitrary value of ζ . ζ is the subscript of the $\Gamma_{\zeta}(x)$ function, Eq. 3.75, and is either α or β , see Eq. 3.76, based on whether we are looking at the electron or ion term.	40
3.3	Plots showing how the profile changes based on changes in n_e or T_e . These profiles are normalized to 1 and show the longer wavelength peak when the laser wavelength is 526.5 nm. In (a) $T_e = 50$ eV and in (b) $n_e = 5 \times 10^{18}$ cm ⁻³	46

3.4	A plot showing two profiles of the EPW spectra based on including a gradient or not. The blue profile is generated from a $T_e = 50$ eV and a density profile with 50 % of the scattering volume at $n_e = 5 \times 10^{18} \text{ cm}^{-3}$ and 25% at $\pm 20\%$. The orange profile is a best fit to this profile, assuming no density gradients, and measures $T_e = 55$ eV and $n_e = 4.8 \times 10^{18} \text{ cm}^{-3}$. This shows that failing to account for gradients causes the measured T_e to be higher than the true value and n_e to be lower than the average value.	47
3.5	A diagram of a sample Thomson scattering IAW spectral profile.	49
3.6	Plots showing the effect of a flow velocity gradient in the scattering volume. (a) shows a plot of the 10 individual Thomson scattering profiles if the flow velocity had a FWHM of 10 km/s, and the resulting profile. The temperatures used for this profile were $T_e = T_i = 40$ eV. (b) shows the composite profile from the left image as well as an attempt to fit it without accounting for gradients. In this case $T_i = 60$ eV, and $T_e = 31$ eV.	55
3.7	A comparison of a fit without (a) and with (b) an additional Gaussian profile. Blue is the raw data, green is the best fit result without any convolution, and red is the best fit, a result of convolving the green profile with the instrumental function on the left, and both an instrumental and additional Gaussian on the right.	56
3.8	Shows the effect of having a relative drift velocity between the electrons and the ions. For parts (a) and (c) the $\alpha^2 W_{im}(x_e)$ and $\alpha^2 \frac{ZT_e}{T_i} W_{im}(x_i)$ are plotted for the electrons and the ions, respectively. For $u_d = 0$ ((a) and (b)) the imaginary electron term is symmetric about the laser wavelength and so the peaks are the same height. When $u_d = 25$ km/s, though, ((c) and (d)) the imaginary electron term has been shifted, causing the higher energy peak to become less damped, and, therefore, the stronger of the two peaks.	57
3.9	Shows a representation of the three different k vectors.	59
3.10	A plot showing the effect of changing m on the $\frac{\Gamma(1/m)\Gamma(5/m)}{3\Gamma^2(3/m)}$ term in the peak separation. We see by increasing m this term decreases, meaning that the peaks are further apart for a given temperature.	65
4.1	Diagram of the simulation space at the start of the FV simulation. The red region is the 2.5 mm radius pin, and the foil is 4 mm above the bottom of the simulation grid. The line across the grid at 5 mm represents the height of the Thomson scattering laser beam in the experiments.	75

4.2	Comparison between experimental current traces and the computational model of the current (in red) from Eq. 4.17. We see that the shape agrees well with the experiment, though the intensity of the first peak could have been increased slightly. We also show the temporal range during which most Thomson scattering measurements were taken in the experiments.	75
4.3	Diagram of the simulation space at the start of the DG simulation. The red region is the 2.5 mm radius pin, and the foil is 2.5 mm above the bottom of the simulation grid, at $z = 0$. The line across the grid at 5 mm represents the height of the Thomson scattering laser beam in the experiments.	76
5.1	(a) shows an r - θ plane slice of the plasma at a height of 5 mm. It shows a representation of the alignment of the fibers in the r - θ plane relative to the jet and \mathbf{k} , \mathbf{k}_s , and \mathbf{k}_l in this plane. (b) shows the same jet, but now in the r - z plane. We see a representation of the alignment of the fibers that were along the z -axis, as well as all \mathbf{k} , \mathbf{k}_s , and \mathbf{k}_l that are in this plane. (c) shows the 3-D representation of \mathbf{k} for the 3 scattering directions, along with the representation of v_k along all three directions for an arbitrary ion velocity. Reproduced from [8], with the permission of AIP Publishing.	79
5.2	Here we show the raw spectra from the individual fibers for a typical shot in reverse polarity with $-0.9 \text{ T } B_z$. The plots show the spectrum from the fiber collecting scattering along \mathbf{k}_{s1} in black, while the fiber along \mathbf{k}_{s2} is in red, and the laser wavelength is in blue. Reproduced from [8], with the permission of AIP Publishing.	80
5.3	Shows the measured velocity components, v_r and v_θ , at $z = 5 \text{ mm}$, for a typical shot in reverse polarity with $-0.9 \text{ T } B_z$. The gray shaded regions in this figure represents the dense conical shell of the jet, estimated from fibers with increased Thomson scattering intensity. Reproduced from [8], with the permission of AIP Publishing.	80
5.4	Here we see the effect on v_θ when changing either the direction of B_z or the polarity of the current. The blue squares show the same results as Fig. 5.3, and are in reverse polarity, RP, with $-0.9 \text{ T } B_z$. The green circles show the results when B_z changes signs, $+0.9 \text{ T } B_z$, and the red diamonds show the results of changing the current polarity (to standard polarity, SP, with a cathode pin). We see that both of these changes switch directions of the plasma rotation, consistent with the $J_r B_z$ component of the $\mathbf{J} \times \mathbf{B}$ force that causes the rotation. Reproduced from [8], with the permission of AIP Publishing.	81

5.5	Measure of ion flow velocity at 160 ns along all 3 axes for shot 4236. We see that in the jet the ions are rotating at 15-20 km/s. Two measurements for the radial component are shown with blue squares and cyan triangles. The jet was moving upward at a velocity of between 40-90 km/s, with increasing velocity going away from the center of the jet. The gray shaded region represents the location of the jet. Reproduced from [8], with the permission of AIP Publishing.	82
5.6	Simulation ion velocities in the radial, axial, and azimuthal directions for a lineout 5 mm above the foil at 160 ns after the start of current rise. Overlaid ion density (gray dotted line) helps to indicate the region of the jet. Reproduced from [8], with the permission of AIP Publishing.	82
5.7	An XUV image of the plasma jet with the laser going through it. The intensity bubble in the image is a result of the laser perturbing and heating the plasma jet.	84
5.8	Averaged results showing the radial velocity as a function of position (a) and electron temperature (b) based on the probe laser energy and the current polarity. Though T_e is clearly affected by the input laser energy, there does not seem to be any effect on the radial velocity of the plasma.	85
5.9	The electron temperature for a typical Al jet with 10 J of laser energy. Time zero for all these plots is the peak intensity of the scattered radiation, which in this figure is 170 ns after the start of the current pulse. The blue circles are the data for each time segment (time width of 270 ps), the green line and region is the best fit and error bars if the entire streak signal is time integrated, and the red region is the measurement from the gated camera. The y-axis error bars represent one sigma errors from the Monte Carlo simulation, while the x-axis error bars are the time period of a single measurement. [1]. ©2018 IEEE	87
5.10	Comparison between experimental data (blue) and a model (red) of the laser heating the plasma. For part (a) the model had $v_z = 60$ km/s and for part (b) $v_z = 0.6$ km/s. Both graphs show similar cooling, which means that cooling is due to plasma expansion and not the heated plasma leaving the scattering volume.	91
5.11	Results for a 10 J shot at 190 ns (a) and 1 J shot at 180 ns (b). The later time shot has a similar profile to that of the shot taken at 170 ns, showing that the plasma jets have similar plasma parameters over a time scale of 10s of ns. For the 1 J shot, the jet temperature stays relatively constant, unlike when using 10 J of laser energy [1]. ©2018 IEEE	91
5.12	The electron temperature for a typical Ti jet with 10 J of laser energy in (a) and with 1 J of laser energy in (b) [1]. ©2018 IEEE	93

5.13	The raw data from the 1 J Ti shot. Shows that we have one bright sharp peak for the start of the laser pulse, making it impossible to make measurements of the electron temperature. Peaks could be moving apart at early times, suggesting we are even heating the plasma with 1 J.	93
5.14	A comparison between the streaked spectra for an Al jet (a) and a Ti jet (b). During the first half of the laser pulse the Ti jet has significantly narrower ion-acoustic peaks than the Al jet does [1]. ©2018 IEEE	94
5.15	Results from a Ti shot where there were possibly four IAW peaks. This could suggest two different species in the scattering volume, or some complex wave. Assuming they are all IAW features, the resulting electron temperatures are 230 and 42 eV. . . .	95
5.16	Comparison of the ratio of the best fit electron temperature between the two different scattering angles based on the assumed electron density. This data was taken with 2.5 J of laser energy and the different colors show the ratio at different times into the laser pulse. Reproduced from [2], with the permission of AIP Publishing.	97
5.17	Plots showing the viability of using Thomson scattering from 2 different wave vectors in order to measure density of the plasma, with the viable region in between the two blue lines, and the green dot being our estimated plasma parameters. In (a) we see our current setup, using a laser wavelength of 526.5 nm and scattering angles of 60° and 150°. (b) shows a proposed set up that involves collecting from 2 different laser wavelengths (526.5 nm and 263.25 nm) both at 150°. Reproduced from [2], with the permission of AIP Publishing.	98
5.18	(a) is the raw data from a single SP shot where clear EPW waves were seen. We see that the density of the plasma increases as we approach the axis of the plasma jet, as the EPW peaks are further apart there. (b) shows the line outs from each fiber, with the red trace being on the axis of the plasma.	100
5.19	Results from fitting the data shown in Fig. 5.18. (b) is just a zoomed in version of (a) to focus on the low-density region. We see on axis, the density of the jet is $5 \times 10^{18} \text{ cm}^{-3}$, while outside of the jet the density is about $6 \times 10^{17} \text{ cm}^{-3}$	101
5.20	Results from both the EPW feature (blue dots) and the interferometry (solid lines). For the interferometry data the blue is the result of the fringe trace and the orange and green traces are the upper and lower error bars from the Abel inversion, which are removed near the axis. This is because Abel inversion struggles near the axis. We see reasonable agreement between the density measurements from the two diagnostic techniques.	101

5.21	(a) shows raw data from a shot that was denser than the previous shot, however, the EPW feature was harder to see. (b) shows the same shot but with the intensity increased to emphasize the fact that one of the fibers appeared to have two sets of EPW peaks. (c) shows the line outs from each fiber, with the axis of the plasma being between the two red traces.	102
5.22	Results from fitting the data shown in Fig. 5.21. (b) is just a zoomed in version of (a) to focus on the low-density region. We see on axis, the density of the jet is higher than for shot 5077, over $1 \times 10^{19} \text{ cm}^{-3}$, but outside of the jet the density is still about $5 \times 10^{17} \text{ cm}^{-3}$	103
5.23	Results from both the EPW feature (blue dots) and the interferometry (solid lines). In this shot we see differences in the measured density from the two diagnostics, though both show higher density than shot 5077.	104
5.24	The raw interferogram from shot 5078, with the blue line being where we believe the Thomson scattering laser is. We see in this shot that in the region of the laser the fringes are complicated, suggesting that we have already perturbed the plasma, which would cause this diagnostic to be inaccurate.	104
5.25	Comparison of the measured value for T_e between the EPW feature (a) and the IAW (b). The EPW was from 90° and was recorded on a gated camera. The IAW feature was recorded at 150° from the axis of the plasma jet and was streaked in time. While both diagnostics measured higher temperatures for shot 5078, the EPW spectral feature measured significantly higher temperatures compared to the IAW spectral feature.	105
5.26	Comparison between T_e vs. time for standard and reverse polarity from Thomson scattering for shots centered at 180 ns (a) and 120 ns (b) into the current pulse. We see that the shots at 180 ns heat more than the shots at 120 ns and that at both times the jet in RP is heated more. In addition, we see relatively good agreement between the measured T_e from the two different scattering angles.	109
5.27	Results of the density from interferometry measurements for the same shots as shown in Fig. 5.26. We see that RP jets are denser than SP jets and that the density increases as time progresses. This density difference agrees with the difference we see in the heating of the jets. The cyan and magenta colors represent the error bars on the Abel inversion for the interferometry.	110
5.28	Schematic of the coupling system used to improve the coupling between the fiber bundle and the spectrometer in order to match the f-numbers. This setup significantly improves the light collection. However, it decreases the spectral resolution as the slit width is $200 \mu\text{m}$ instead of $100 \mu\text{m}$	112

5.29	Results from T_e measurements with either 0.5 J (a) or 1 J (b) of laser energy for both current polarities. RP shots are shown in blue and SP shots are in red. Since the temperature is relatively constant throughout the laser pulse and the temperature is similar between the two laser energies, we are no longer in a region where the laser affects the measured value for T_e . We see that T_e is similar between the two jets and is about 15 eV.	113
5.30	Results from T_e measurements with 2.5 J of laser energy for both current polarities. We see in this case we are heating the jet, and that the RP jets heat up more than the SP jet, which agrees with previous results.	113
5.31	T_e measurements from an bin in time of the entire streak signal as a function of laser energy. We see for low laser energies the temperature of the two jets is very similar. As the laser energy increases both jets begin to heat up, but RP jets heat up more. . .	114
5.32	T_e measurements from time integrated streaked signals for 0.5 J (a) and 1 J (b). This data does not use the MC method for the error bar calculation, but instead tries to find the maximum and minimum possible value for T_e within a reasonable range of fitting methods.	115
5.33	(a) shows n_e and (b) shows T_e for FV simulations of the two jets at 170 ns into the current pulse, with SP on the left and RP on the right. We clearly see in these simulations the RP jet is hotter and wider than the SP jet. The horizontal line is 5 mm above the pin, where we aligned the Thomson scattering laser.	115
5.34	Plots comparing experiments and FV simulation at 170 ns and 5 mm above the pin with n_e in (a) and T_e in (b). We see that the jet widths are in good agreement, T_e is slightly higher in the simulations, and n_e is much higher in the simulations.	116
5.35	(a) Shows n_e and (b) shows T for the two jets at 170 ns into the current pulse from DG simulations, with SP on the left and RP on the right. We clearly see in these simulations that the RP jet is wider than the SP jet. The horizontal line is 5 mm above the pin, where we aligned the Thomson scattering laser.	117
5.36	Plots comparing experiments and DG simulations at 170 ns and 5 mm above the pin with n_e in (a) and T in (b). We see jet widths, densities, and on-axis temperatures disagree between the simulations and experiments.	117
5.37	Plots comparing experiments, FV simulations, and DG simulations at 170 ns and 5 mm above the pin with n_e in (a) and T in (b). These results were shown separately in Fig. 5.34 and Fig. 5.36 but are repeated here for easy comparison between the two different simulation techniques.	118

6.1	A possible setup to collect IAW and EPW spectral features from the same scattering volume. Using a beam splitter enables both spectral features to be recorded from the same line of sight. Each fiber takes the light to a different spectrometer.	126
6.2	Figure demonstrating how we could split the beam into two pulses without wasting half of the laser energy. The first prism splits the beam in half, while the second prism acts as a retro reflector. This may have issues at focus as the beam profile is no longer circular, but would allow most of the laser energy to propagate along a nearly collinear path. To expand this system to enable 4 pulses, another pair of prisms would be needed, this time with the laser coming out of the page, which would split the laser into quarters.	127
6.3	A setup that could be used to collect scattering from 4 pulses each at 1.25 J of laser energy. This setup has less energy than Fig. 6.2, but does not disrupt the shape of the beam. There would be 4 paths: AC, AD, BC and BD. A possible setup for this would be to make B 6 ns longer than A and D 3 ns longer than C to get a continuous 12 ns pulse.	128

CHAPTER 1

INTRODUCTION

1.1 Motivation

A key challenge to high energy density plasma physics (HEDP) is diagnosing the plasma. This is difficult in HEDP plasmas due to the short time scales, typically on the order of 10 ps-100 ns, and high temperatures, which are often 10 eV or much higher. One useful diagnostic is Thomson scattering, as it has the capabilities to simultaneously measure multiple parameters from a fixed volume of plasma. Though optical non-collective Thomson scattering has been used for many years in lower density plasmas, such as tokamaks (for example, see [51, 52]), few facilities use optical collective Thomson scattering, which is appropriate for the higher densities of HEDP plasmas. Even for plasmas appropriate for collective optical Thomson scattering it is primarily found in labs that use lasers to produce the plasma, including at Lawrence Livermore National Laboratory [57, 27] and at the Omega Laser facility at University of Rochester [58, 42]. For plasma made by pulsed power devices the use of collective Thomson scattering is known to us to be used as a diagnostic only at Imperial College [66] and here at Cornell University.

One of the primary interests of the field of HEDP and plasma physics in general is a reliable fusion energy source, which would help address the growing problem of the world relying on nonrenewable energy sources that harm the environment. Fusion, however, is a very challenging goal where the fusion fuel, often deuterium-tritium, must be confined at a temperature of at least 50,000,000 K for a length of time that inversely depends on the plasma density.

Plausible solutions range from relatively low-density plasmas that use magnetic confinement, such as tokamaks and stellarators [69], all the way up to high density plasmas that use inertia to confine the plasma, such as laser driven plasmas [45]. In the middle of this density range, which is where pulsed power machines come into the picture, are a range of schemes that use both magnetic fields and inertia to confine the plasma, which are called magnetoinertial fusion (MIF). Examples of these include Magnetized Liner Inertial Fusion (MagLIF) [64] and Plasma Liner Experiment-ALPHA (PLX- α) [38]. These experiments are both very expensive and infrequent, due to the low rep rate of the machines. This means that accurate modeling and prediction capabilities are very important in order to help design and improve the experiments. Therefore, getting the most complete picture of the plasma with different types of diagnostics is very important to verify and improve the models. The field of HEDP also enables studying materials in laboratory-based extreme pressure environments, which is useful for a basic physics understanding of materials and for applications to astrophysics. In these types of experiments, it is again important to have diagnostics that can accurately measure what is happening in the plasma.

As will be discussed throughout this thesis, Thomson scattering can measure at least fluid velocity, electron and ion temperatures, and electron density. As all diagnostics have challenges, it is important to compare similar diagnostics and recognize the advantages and disadvantages of each technique. For Thomson scattering the best techniques to compare it to are interferometry for density measurements and spectroscopy, which can measure both the temperatures and density of the plasma [39]. One key advantage compared to these diagnostic techniques is that Thomson scattering is fundamentally a local measurement, determined by the scattering volume, while the other techniques are

line integrated results. This enables measurements to be made without such other assumptions as the symmetry of the plasma for an Abel inversion, or on the location of emitting or absorbing ions for spectroscopy. Also, compared to spectroscopy, where the wavelengths of the useful lines are both material and temperature dependent, Thomson scattering spectra stay in the same general wavelength region. Therefore, the spectrometer does not need to be substantially changed based on the plasma that is being studied. While Thomson scattering does have its own challenges and difficulties, some of which will be discussed in this work, its issues are different from other diagnostic techniques that can measure the same plasma parameters and, therefore, is a key addition to many diagnostic packages.

Most of the research presented in this thesis focuses on the initial development and then two major expansions of the Thomson scattering system as a reliable diagnostic for experiments on the COBRA (COrnell Beam Research Accelerator) pulsed power machine. The first expansion was using the system with a streak camera to perform time resolved measurements of changing plasma conditions on the 2.5 ns time scale of the laser pulse. Though time resolved Thomson scattering has previously been used in laser produced plasma (for example [59, 22]), the work presented in this thesis we believe is the first application of this type of diagnostic capability to pulsed power plasmas. The second major expansion was the use of the system to record the high frequency spectral feature (electron plasma wave) from the Thomson scattering profile. Though this feature is harder to see due to its being significantly weaker than the ion acoustic wave spectral feature, it is useful as a measurement of the density of the plasma and can also provide information on the electron temperature. This again has been used for some time in laser produced plasmas. However, only

recent experiments at Cornell and at Imperial College in London [34] have used this diagnostic on pulsed power produced plasmas.

The load that was used for the COBRA experiments described in this thesis was a thin disk of aluminum foil (we will call it a radial foil) that was used to create a plasma jet along the central axis of the radial foil. In addition to the physics interests that will be discussed shortly, this was chosen as it was a reliable load for diagnostic development. Many pulsed-power-driven HEDP experiments can be challenging for the development of time and location sensitive diagnostics as they tend to involve a Z-pinch, a plasma configuration that can move and change quickly within the time scale of the experiment. This is a complication, as even a few ns of jitter or changes in the current pulse could result in the scattering volume not being in the plasma region of interest. Since many of the experiments in this thesis used Thomson scattering in ways that had not been done before on these types of plasmas it was desired to reduce the inconsistency from the load so that the effectiveness of the Thomson scattering system design could be more accurately diagnosed. Radial foils are a perfect load for these tests, as they form plasma jets that are relatively long lasting, over 100 ns, and are consistently very near the center of the chamber.

While developing this Thomson scattering diagnostic three key areas of the plasma jet were explored. The first was the directional flow velocity of the plasma jet when exposed to an external magnetic field, focusing on decoupling the radial and azimuthal velocities [8]. This study followed earlier experiments that used visible spectroscopy to measure that rotation and addressed some of the difficulties of that work [62]. This part of the work was carried out in conjunction with Tom Byvank's experiments that explored the magnetic field effects

on radial foil plasma jets [8].

The second major area explored on plasma jets was the effect of the Thomson scattering laser on the plasma jet. While ideally a diagnostic should not affect what you are measuring, sometimes this cannot be avoided. In the case of the experiments presented in this thesis, the laser energy density initially needed to get enough scattered signal was about 10 times the energy density of the plasma jet [1]. This meant that the Thomson scattering laser was heating the plasma by inverse bremsstrahlung [15, 16, 3] as we were trying to measure the plasma properties. While this heating is unfortunate from a diagnostic perspective, it did enable exploration of laser heating the plasma jet and showed a limitation of the Thomson scattering diagnostic.

The final area that was explored was using Thomson scattering to help study the effect of current polarity on the formation of the plasma jet. Previous experiments and simulations have shown differences in the jet based on the direction of current flow, both with and without an external magnetic field [9, 30, 31, 32]. The experimental work showed differences in the structure of the jet as well as its density. These differences are caused by the fact that the Hall term in the generalized Ohm's law (GOL) [63], proportional to $\mathbf{J} \times \mathbf{B}$, does not change direction based on the direction of the current while all other terms do, see Eq. 4.16. Here \mathbf{J} is the current density and \mathbf{B} is the magnetic field. The previous experiments, however, did not have the capability of measuring the electron temperature of the plasma jet. By designing the experiment to avoid heating from the probe laser it is possible to use Thomson scattering to measure the electron temperature of the plasma jet. This gives a better experimental picture of the plasma jet and provides data to help improve the physics models in computer simulations.

1.2 Outline

Chapter 2 describes the experimental platform used in this thesis. Section 2.1 briefly describes the machine used to create the plasma jets, Sec. 2.2 gives an overview of the load hardware as well as the basic physics that causes the formation of the plasma being studied, and Sec. 2.3 discusses the diagnostics used to study this plasma with a focus on the experimental setup for Thomson scattering in Sec. 2.3.3.

Chapter 3 gives a theoretical overview of Thomson scattering. Section 3.1 derives the collective Thomson scattering profile and introduces the Salpeter approximation, which helps provide intuition on what plasma properties affect the Thomson scattering profile. Secs. 3.2 and 3.3 use the Salpeter approximation to show how plasma parameters affect the ion acoustic wave and electron plasma wave Thomson scattering features. They also discuss complications to the basic Thomson scattering model. Section 3.4 discusses the mathematical calculation of the plasma dispersion function, a requirement for calculating the Thomson scattering spectra. Section 3.5 discusses how best fits to experimental spectra were obtained using theoretical spectra. It also discusses sources of error and how the error bars were found.

Chapter 4 gives a brief overview of the PERSEUS extended magnetohydrodynamic code that was used in this thesis in order to perform computer simulations of the plasma jet.

Chapter 5 discusses the experimental results and compares them to the simulations. This begins with a discussion of the rotation of the jet when exposed to an external magnetic field in Sec. 5.1. Then the laser heating is discussed in

Secs. 5.2 and 5.3. Results from two methods to use Thomson scattering to measure the electron density are discussed in Sec. 5.4. Finally Sec. 5.5 focuses on the importance of current polarity on the plasma jet; both experimental results as well as comparison to simulations are discussed.

Chapter 6 is the conclusion, which summarizes the research and discusses possible next steps for Thomson scattering diagnostic development. It also suggests possible future physics experiments to study laboratory plasma jets.

Appendix A describes the code used to generate non-collisional Thomson scattering profiles with a Maxwellian distribution function. Appendix B describes the code used to generate non-collisional Thomson scattering profiles with a super Gaussian electron distribution function.

CHAPTER 2

EXPERIMENTAL PLATFORM

2.1 COBRA

Experiments presented in this thesis were performed on the COBRA pulsed power generator [33]. COBRA can deliver up to 1.2 MA with a 100 ns rise time. COBRA is designed with 2 Marx generator capacitor banks, as shown in Fig. 2.1, which has the advantage of enabling one to shape the current pulse based on the application. Each Marx bank contains 16 $1.35 \mu\text{F}$ capacitors that are charged in parallel up to 70 kV, resulting in 53 kJ of energy in each bank. The pulse shape can be controlled by 2 different sets of switches, the main switches (labeled as intermediate switch in the figure) and output switches shown in Fig. 2.1. Both sets of switches are self-breaking, with the breakdown voltage being controlled by the pressure within the switch. Current operating procedure uses the main switches for pulse shaping. When a short pulse is desired (100 ns rise time, which is used in this research) both main switches are set to break down after the intermediate storage capacitor (ISC) has charged for 800 ns. If a long pulse is desired (200 ns or longer rise time) the charging time of the south ISC is shortened to 700 ns. For more information on COBRA see various theses written by previous students [5, 10, 37, 12] as well as [33].

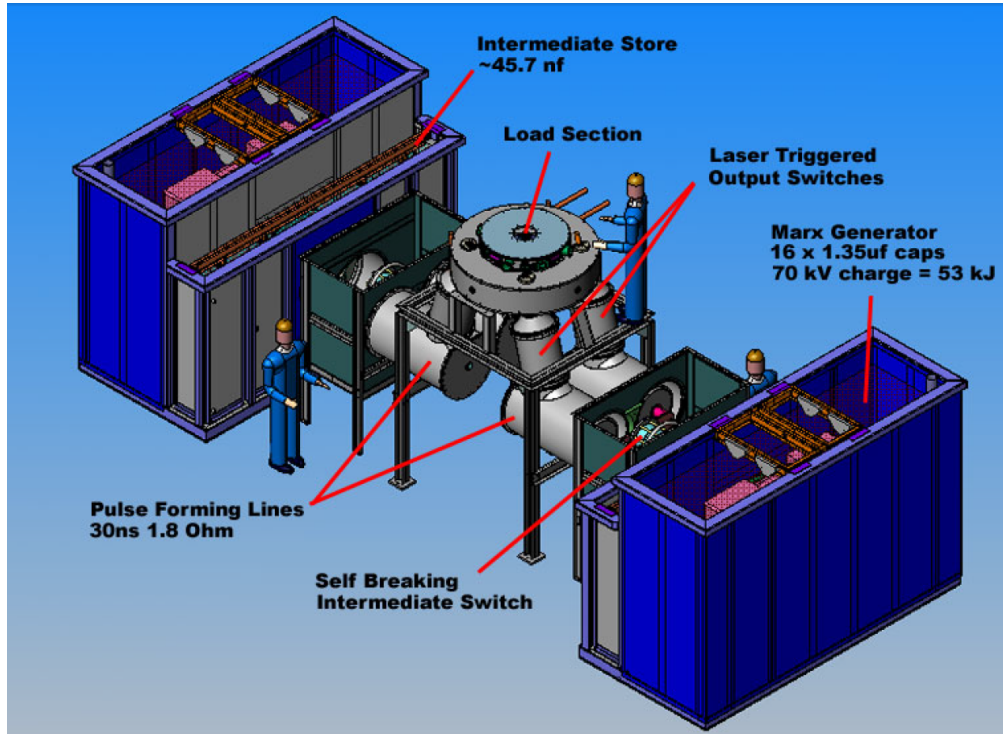


Figure 2.1: CAD drawing of COBRA.

2.2 Plasma Jets

The load used for experiments performed in this thesis was a radial foil that created a plasma jet on axis. A radial foil is a thin metal foil that is connected between the anode and cathode through a ring on the outside and a supporting pin in the center. For most of the experiments a $15\ \mu\text{m}$ Al foil was used; it was Reynolds wrap that you can buy at a grocery store. In addition, experiments were performed with $15\ \mu\text{m}$ Ti foil to see if material properties had significant effects on the Thomson scattering profile or the plasma jet. For all experiments reported here, the center pin was a 5 mm diameter brass pin mounted so that its upper surface was slightly above the outer ring, as shown in Fig. 2.2, in order to ensure good contact with the foil.

As a primary interest of this thesis research was the effect of current polarity

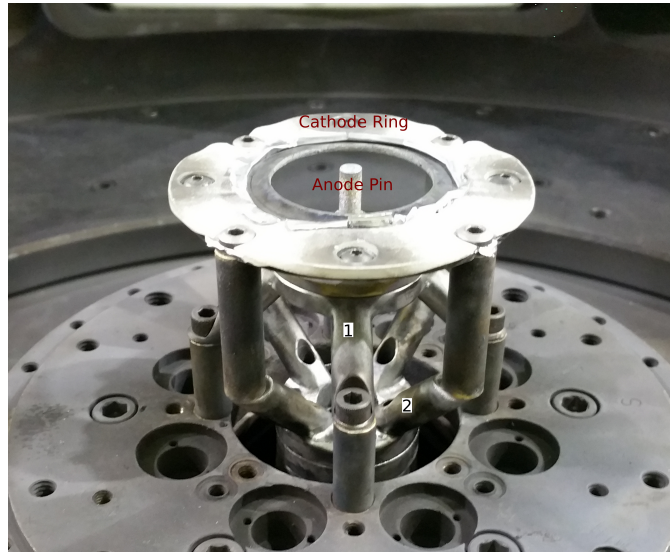


Figure 2.2: Picture of radial foil load hardware in reverse current polarity. The foil is held in the cathode ring and the anode pin is slightly higher than the ring in order to make good contact with the foil. In order to switch to standard polarity, the pieces labeled 1 and 2 are aligned (instead of being at 90°) and the outside ring is connected to the anode by 4 posts.

on the plasma jet, hardware was used to allow switching of the current polarity, which we call the polarity convolute. Standard polarity (SP) is when the center pin is the cathode and the current flows radially inward. If the center pin is setup as the anode, we are in reverse polarity (RP) and, therefore, the current flows radially outward. The hardware setup for RP is shown in Fig. 2.2. In order to switch to standard polarity, the pieces labeled 1 and 2 in the figure need to be aligned, causing the pin to be connected to the cathode instead of the anode.

Figure 2.3 shows the key physics involved in forming the plasma jet. At the start of the current pulse the foil is heated ohmically by the current flowing through it. This heating ablates the top of the foil, creating a layer of plasma. This plasma then is driven onto the axis of the radial foil by the $\mathbf{J} \times \mathbf{B}$ force. This driving force causes the plasma to collimate into a long-lasting plasma jet on axis and is what is studied in this thesis [28]. This jet is collimated by a pres-

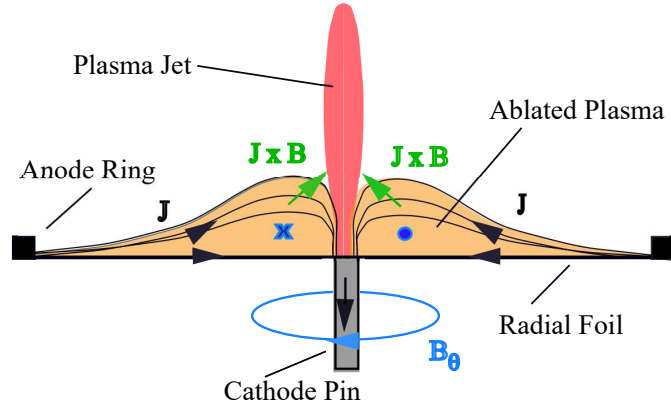


Figure 2.3: Schematic of the plasma jet created from a radial foil in SP current polarity

sure balance between the inward magnetic pressure and the outward thermal pressure, forming a Bennett pinch [4]. Using the experimentally measured temperature (15 eV), density ($6 \times 10^{17} \text{ cm}^{-3}$), and radius (0.9 mm) for a typical jet, we can estimate the required axial current from Bennett's relation [4]

$$I^2 = \frac{8\pi^2 n_e r^2 k_b T}{\mu_0}, \quad (2.1)$$

where r is the radius of the jet, and k_b is Boltzmann's constant. This results in $I = 27 \text{ kA}$, which is only 2.7% of the machine's current at 170 ns into the pulse. This calculation is slightly lower than earlier measurements of the jet current being between 3 and 10% of the machine's current, which were made using B-dot probes on jets made from thinner foils and smaller pins [28, 29].

2.3 Diagnostics

2.3.1 Extreme Ultraviolet Self-Emission Pinhole Cameras

An imaging diagnostic technique used during these experiments was extreme ultraviolet (XUV) self-emission pinhole photography, which recorded time-gated images of the XUV (10-100 eV) range of the plasma emission. In order to record the XUV emission a microchannel plate (MCP), which creates an image on a phosphor fluorescent screen, and a charge coupled device (CCD) camera, which images that phosphor fluorescent screen, were used. The MCP is gold coated and has 4 independently triggerable regions, arranged in the form of quadrants, giving these cameras the jargon name, “quad cams”. The thickness of the gold coating controls what photon energy the MCP is sensitive to, with lower energies being reflected off the surface, while higher energies are absorbed by the MCP. The photons with energies that are absorbed by the gold coating then enter the photomultiplier tubes (PMT) of the MCP where a photoelectron initiates an electron avalanche when the PMT is gated on by an applied voltage pulse of about 5 kV. These electrons then hit a phosphor fluorescent screen that is viewed by an external CCD camera (a Canon camera in our case). For this experiment the external voltage was applied to each quadrant of the MCP for 5 ns. Each of these MCP quadrants viewed the plasma through a different pinhole, with an example of light going through one pinhole and hitting a single quadrant being shown in Fig. 2.4. Through the differences in cable lengths between the power supply and the MCP, successive frames were delayed by an additional 10 ns relative to the first frame, which allowed a single quad-cam to record a 30 ns time history of the plasma in XUV emission. Since we had two of

these cameras it was possible to record the plasma for 70 ns with 10 ns between each of the 5 ns frames.

The photon energies that were resolvable by the detector are function of both the detector itself and the optical arrangement being used. Figure 2.4 shows the general setup for the XUV pinhole cameras; for these experiments $o = 53$ cm, $i = 38$ cm, D (the pinhole size) was $200 \mu\text{m}$, and ΔL (the resolution of the MCP) was $27 \mu\text{m}$. This $27 \mu\text{m}$ is a combination of the $12 \mu\text{m}$ size of the PMT channels and the $15 \mu\text{m}$ separation between those channels. The minimum size feature that can be resolved by our detector, Δx , is determined by the larger of the values obtained from the following two equations:

$$\Delta x = \frac{o}{i}\Delta L, \quad (2.2)$$

$$\Delta x = (1 + \frac{i}{o})D. \quad (2.3)$$

The first is the limit of the detector and is $38 \mu\text{m}$, while the second is a limit because the pinhole will cause a point object to spread out and is $344 \mu\text{m}$ for our setup. Using this and the diffraction limit of light we then can find what photon energies are resolvable on the detector. The diffraction limit is

$$\Delta x = 1.22i\frac{\lambda}{D} \quad (2.4)$$

with λ being the wavelength of the self-emission. Solving this using our resolution of $344 \mu\text{m}$ shows that photon energies levels above 8.3 eV ($\lambda < 150$ nm) are resolvable by our detector.

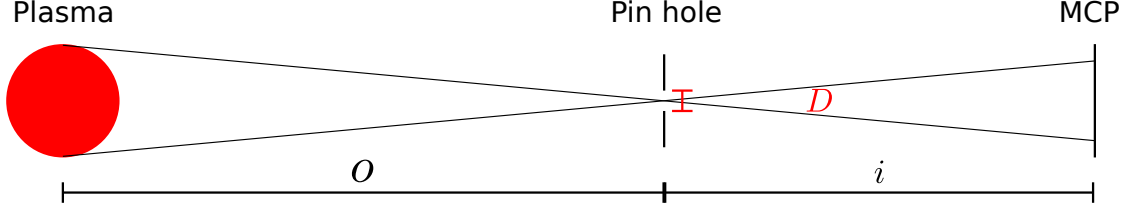


Figure 2.4: Schematic of the general setup for XUV self-emission pinholes.

2.3.2 Laser Interferometry and Shadowgraphy

In these experiments we used an EKSPLA laser to study the plasma density and density gradients through laser interferometry and laser backlighting shadowgraphy, respectively. The laser uses a Nd:YAG medium to produce a 1064 nm beam that is frequency doubled to 532 nm. This “green beam” has a pulse width of 148 ps, and energy of 140 mJ. We split this laser beam into 3 pulses which were separated by 10 ns. Each pulse went through the plasma along a similar path, giving a time history of the plasma. Each laser path could be used for both interferometry and shadowgraphy measurements.

Key to understanding interferometry is that plasma changes the phase velocity, $v_{ph} = \omega/k$, of an electromagnetic (EM) wave traveling through it, where ω and k are the frequency and wave number of the EM wave in the plasma. In a non-relativistic plasma, ω and k are related by the dispersion relation $\omega^2 = \omega_{pe}^2 + k^2 c^2$, with c being the speed of light in a vacuum and $\omega_{pe} = \sqrt{n_e e^2 / \epsilon_0 m_e}$ being the electron plasma frequency. This means the index of refraction of the plasma is

$$n_p = c/v_{ph} = \sqrt{1 - \frac{\omega_{pe}^2}{\omega^2}}. \quad (2.5)$$

This change in the index of refraction, or speed relative to c of the EM wave, is important as it allows information to be gained by interfering two different

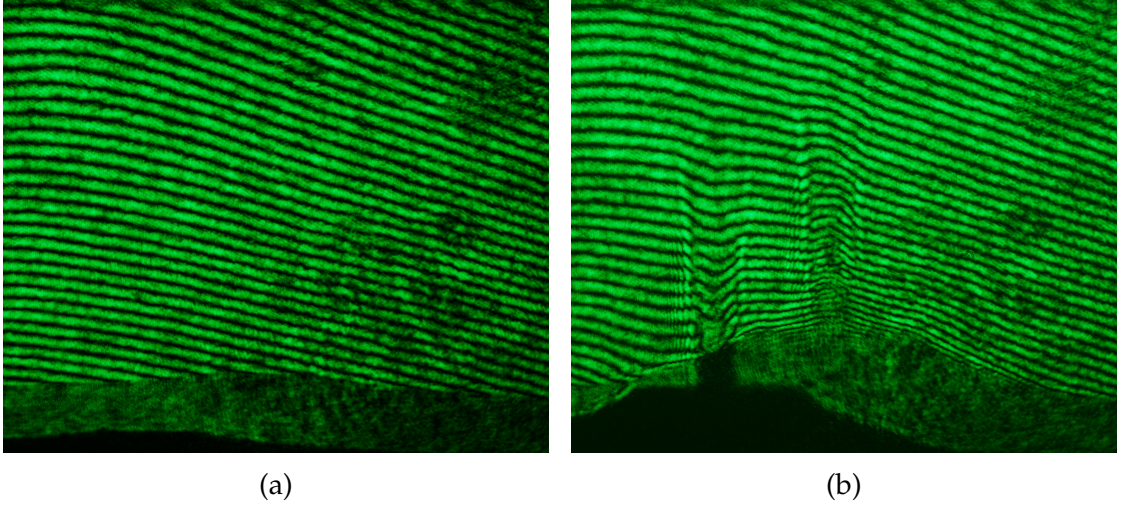


Figure 2.5: Sample image of the fringe patterns before a shot (a) and during a shot (b). These were taken from a large shift shearing interferometer configuration.

parts of the same beam. If one part of the beam goes through the plasma and another part does not, the optical path lengths of the two beams will be different, causing interference fringes to appear when the beams are recombined. By comparing the fringe pattern before a shot to that during a shot (see Fig. 2.5) it is possible to measure the changes in the index of refraction and, therefore, extract the electron density.

The fringes in the interference pattern change based on the change in phase $\Delta\phi$ which corresponds to the optical path length difference ΔL along the line of sight

$$\Delta\phi = \frac{2\pi}{\lambda}\Delta L, \quad (2.6)$$

where λ is the wavelength of the laser. The optical path length difference can be related to the difference in the index of refraction for the probe, n_p , and the reference, which we will call 1 since it is very close to unity in both air and

vacuum along the path of the laser,

$$\Delta L = \int (n_p - 1) dx = \int \left[\left(1 - \frac{\omega_{pe}^2}{\omega^2} \right)^{1/2} - 1 \right] dx = -\frac{1}{2} \int \frac{\omega_{pe}^2}{\omega^2} dx, \quad (2.7)$$

where the last step assumed that $\omega_{pe}^2 \ll \omega^2$.

From Eq. 2.5 we see that if $\omega_{pe} > \omega$ the laser will not be able to propagate through the plasma, as the dispersion function becomes imaginary. The density at which this occurs is called the critical density, n_{cr} . For our laser frequency the critical density is $4 \times 10^{21} \text{ cm}^{-3}$. While this creates a hard maximum for the density that can be found with interferometry, density gradients within the plasma will diffract the laser, causing it to often be impossible to make measurements even an order of magnitude below this limit.

We can now cancel all terms other than density between ω and ω_{pe} which gives

$$\Delta L = -\frac{1}{2} \int \frac{n_e}{n_{cr}} dx, \quad (2.8)$$

and the resulting phase shift is

$$\Delta\phi = -\frac{\pi}{n_{cr}\lambda} \int n_e dx. \quad (2.9)$$

A phase shift of 2π corresponds to a single fringe shift, which means that

$$F = \frac{1}{2n_{cr}\lambda} \int n_e dx, \quad (2.10)$$

where F is the number of fringe-shifts. This means that a shift of one fringe corresponds to a line integrated density of $4.2 \times 10^{17} \text{ cm}^{-2}$ for $\lambda = 532 \text{ nm}$.

One of two different experimental arrangements were used to record interferograms. The first configuration was a Mach-Zender interferometer, like that shown in Fig. 2.6. In this type of interferometer, the reference beam path is separated from the probe beam path using a beam splitter and is routed around the

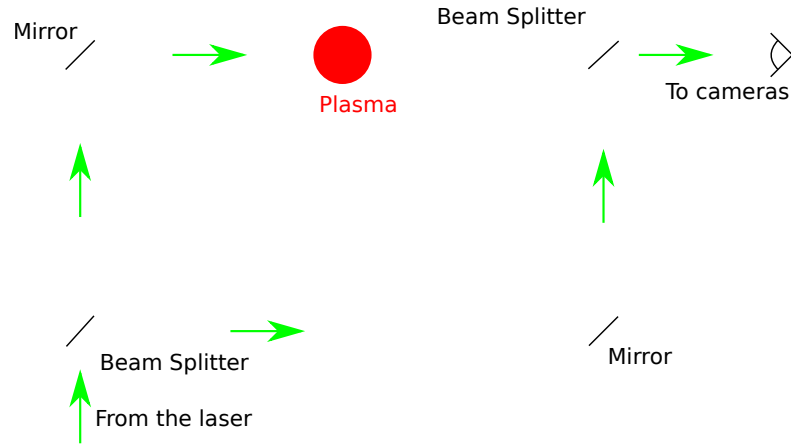


Figure 2.6: Schematic of a Mach-Zender interferometer.

experimental chamber. After the probe beam passes through the chamber, the two beams are recombined using a beam splitter and produce the interferometry pattern. The other technique used was a large shift shearing interferometer. In this setup a single beam passes through the plasma and then the beam is split by two 90° prisms with a small air gap between them [54]. These prisms split the beam into two parts that are close enough together that they can interfere with each other. By separating the images enough that the plasma region of one of these beams overlaps with the vacuum region of the other beam, allows analyzing the interferometry pattern as if it was a Mach-Zender interferometer.

Analysis of interferometry images produces a measure of the areal density of the plasma. However, we are interested in the volumetric density of the plasma. In order to extract the volumetric density from the data, an Abel inversion needs to be performed. This inverse transform requires the assumption of axial symmetry, which is a reasonable first order approximation for our well collimated jets. The Abel transform was performed using the onion peeling method [14] from the PyAbel package in Python. As a note, inverse integration tends to have

large error bars near the axis, but interferometry should give a good idea of at least the general structure of the plasma, as well as a good comparison to density measurements from Thomson scattering, except perhaps near the plasma axis.

The three laser beams were also used for laser shadowgraphy, which shows gradients within the plasma volume. If there is a density gradient in the plasma perpendicular to the laser propagation direction, the change in the optical path length causes the laser to refract. This refraction of light causes bright and dark regions to form in the image. Light is refracted into the bright region while it is refracted away from the dark regions. We use these images primarily for a qualitative image of the structure of the jet. For a more detailed discussion of both of these laser diagnostics the reader is directed to *Principles of Plasma Diagnostics* by I. H. Hutchinson [39].

2.3.3 Thomson Scattering

The primary diagnostic used in these experiments was Thomson scattering. While a detailed theoretical description of Thomson scattering is provided in Ch. 3, here we will outline the experimental arrangement and equipment used to probe and diagnose the plasma. In order to perform Thomson scattering, one needs an adequately powerful probe of EM radiation to overcome plasma continuum radiation, and a way to collect the scattered radiation from the plasma in order to study its spectrum.

To probe our plasma, we used a laser that produces 10 J of radiation at 526.5 nm. The laser has a Nd-YLF diode-pumped master oscillator and 4

flashlamp-driven amplifiers. This produces a 25 J beam of radiation at 1063 nm that passes through a frequency doubling crystal in order to produce the final output pulse at 526.5 nm. The resulting laser pulse is linearly polarized, with a top-hat spatial profile, a beam diameter of 35 mm, and a Gaussian temporal profile with a full width at half maximum (FWHM) of 2.3 ns. If less laser power is desired it is possible to run the system with only 3 of the 4 amplifiers, which produces a 1 J pulse at 526.5 nm.

Before the laser beam is focused to the center of the chamber, it is first passed through a half-wave plate that enables rotation of the linear polarization (i.e., the direction of the electric field) of the beam. The laser is then focused by a 2.5 m f/50 plano-convex lens. When entering the vacuum chamber, the laser passes through a Brewster window, which does not reflect one polarization of light. The polarization of the laser is, therefore, set by rotating the half-wave plate to minimize the reflection off of the Brewster window. The polarization is set along the z-axis of the plasma when all the scattering directions and the laser are in a plane perpendicular to that axis. However, if scattering along the z-axis of the plasma is desired then the polarization must be changed since scattering does not occur in the polarization direction of the probe beam. The final spot size was measured to be 350 μm by moving a knife edge across the laser's focus.

Due to 10 J being significantly more energy than was needed for many scattering experiments, when we wanted to probe the plasma over longer time scales than a single laser pulse, the laser was split into two pulses using the optical setup shown in Fig. 2.7. This design enables a time delay between the two laser pulses, by having a path length difference between path A and path B. This path length can be modified by changing the distance between the 'X' labeled optics

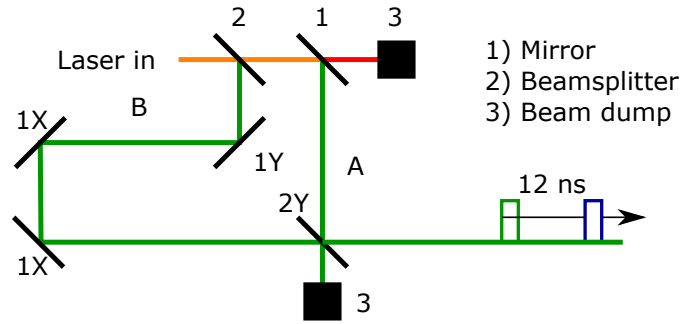


Figure 2.7: Diagram of the optics and path used to delay part of the laser beam. The path length difference, or the time delay, between paths A and B is controlled by the distance between the ‘X’ labeled optics and the ‘Y’ labeled optics. The orange part of the beam indicates that the infrared (IR) and the green beams are both present. The upper two optics both allow the IR beam (in red) to pass, thereby separating it from the frequency doubled green beam. The two beam dumps collect the unused IR beam and the unused half of the green beam. Reproduced from [2], with the permission of AIP Publishing.

and the ‘Y’ labeled optics. Based on space currently available on the 10 J laser optics table, this time delay can be varied from 3 ns, for a continuous pulse, up to about 14 ns in the space available next to the laser. The recombining beamsplitter (labeled 2Y) enables the two split beams to be passed co-linearly into the load region, meaning that the scattering volume is the same for both laser pulses. One disadvantage of this setup is that it causes half of the available laser energy to be lost and each of the laser pulses to be limited to 2.5 J.

To display the spectrum of the scattered light from the probe beam, a collection lens and fiber bundle delivered the scattered light from the plasma into the spectrometers that dispersed it as a function of wavelength, which will be discussed shortly. Two different 18 m long fiber bundles were used in these experiments. The first fiber bundle was made up of a linear array of twenty $100\ \mu\text{m}$ fibers with a numerical aperture of 0.1. At the input end of the fiber bundle, the fibers had a center to center spacing of $125\ \mu\text{m}$, while on the spectrometer end, the fibers had a center to center spacing of $500\ \mu\text{m}$ to help reduce the cross talk

between neighboring fibers. The other fiber bundle was similar in design, except that on the input end the fiber was split into 2 separate bundles, which enabled looking at scattered light from 2 different angles on the same detector.

To couple the light from the experiment into the fiber, a lens or lenses must be used. Within the experiments performed here there were two primary designs. The first, which was used in earlier experiments, utilized a single plano-convex lens to collect the light from the plasma and then focus it into the fiber. The magnification and focal length in this simple arrangement are controlled by the following equations

$$m = \frac{i}{o} \quad \text{and} \quad \frac{1}{f} = \frac{1}{i} + \frac{1}{o}, \quad (2.11)$$

where m , i , o , and f are the magnification, image distance, object distance, and focal length, respectively. Therefore, if a lens with a known focal distance is placed a certain distance from the load, the magnification would be

$$m = \frac{f}{o - f}. \quad (2.12)$$

In order to keep the lens outside of the vacuum chamber, the minimum object distance is about 55 cm. Therefore, changing the focal length is the most flexible way to modify the field of view of a fiber bundle. A typical lens used in these experiments had a focal length of $f = 12.5$ cm, which resulted in a field of view for each fiber of $360 \mu\text{m}$.

Though this was the easiest lens system to setup, it did have some major disadvantages. The first was that a singlet lens has chromatic aberrations. As early experiments looked near the laser wavelength this was not a major consideration. Later experiments, however, required light collection over a wider bandwidth, meaning that chromatic aberrations were not desired. In addition, using a singlet lens for focusing also leads to significant spherical aberrations.

These focus issues were resolved by using a pair of achromatic doublets. One of the doublets was used to collect and collimate the scattered radiation from the plasma, while the second doublet focused the collimated light into the fiber. Since these lenses collected or focused the light at the focal length of the lens, the magnification of the fibers is simply a ratio of the focal lengths of the two lenses. Based on the numerical aperture of the fiber the best f /number of the focusing lens was $f/5$. Therefore, if we are using 50 mm diameter optics, the ideal focal length is 25 cm. The collecting lens focal length can then be varied to get the desired magnification. This scheme was used in all later experiments and appeared to significantly improve the quality of focus over the singlet system. Therefore, it is recommended to be used in all future experiments.

To spectrally resolve the scattered light, a Czerny-Turner spectrometer was used. The basic setup of this type of spectrometer is shown in Fig. 2.8. The diffracting element in this spectrometer is the diffraction grating, which can be rotated to a certain angle based on the desired central wavelength at the exit slit. Our lab has two different length spectrometers that can be used for various experiments, one that is 330 mm long and two that are 750 mm long, both part of the Andor Shamrock series. Each spectrometer has a rotating turret with 3 different diffraction gratings, which gives options for different spectral resolution and bandwidth for each spectrometer.

To choose the best spectrometer and grating it is important to understand the linear dispersion and resolving power of the spectrometer. Key to this problem is the fundamental equation for grating spectrometers [44]

$$\sin(\alpha) + \sin(\beta) = 10^{-6}kn\lambda, \quad (2.13)$$

where α and β are the angles of incidence and diffraction as shown in Fig. 2.8,

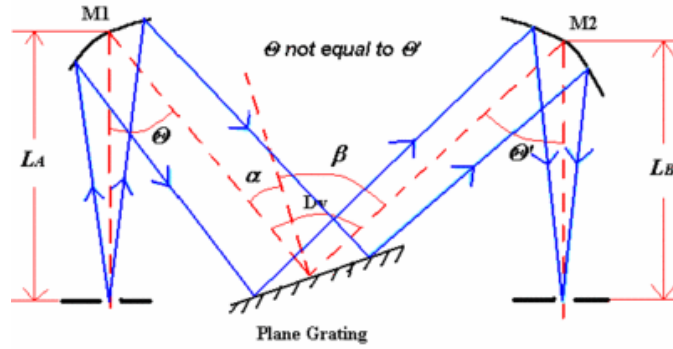


Figure 2.8: A schematic of a Czerny-Turner spectrometer [44].

k is the diffraction order, n is the number of grooves per millimeter, and λ is the central wavelength in nanometers. Since the spectrometer has fixed entrance and exit locations, α and β can be related by

$$D_v = \beta - \alpha \quad (2.14)$$

with D_v being a constant determined by the spectrometer.

Now we are interested in finding the dispersion of the spectrometer, which is in the units of nm/mm. The smaller this number, the higher the dispersion, which means it is easier to resolve finer spectral details. The linear dispersion can be shown to be [44]

$$\frac{d\lambda}{dx} = \frac{10^6 \cos \beta}{knL_B} \quad (2.15)$$

with L_B being the exit focal length of the spectrometer in mm. We clearly see that we can increase the linear dispersion of our spectrometer by increasing either the length of the spectrometer, or the number of grooves per millimeter.

Therefore, for high resolution application we want to use our longest spectrometer with the most grooves per millimeter. This means for high resolution application the 750 mm spectrometer with 2400 1/mm was used. This resulted in a spectral FWHM of 0.6 Å. In applications that did not need as high

resolution, various combinations were used based on the desired bandwidth and resolution for the application. A typical setup used the 330 mm spectrometer with a grating of 150 l/mm, which gave a FWHM of 20 Å and allowed seeing the entire visible light spectrum.

To record spectra from the spectrometer, two different devices were used. One was a time-gated ICCD camera. This enabled capturing the scattered radiation from the plasma from up to 18 different locations (using the previously mentioned fibers) simultaneously. The camera captured a time integrated picture of the scattered light as well as radiation from the plasma during the length of the gate pulse. Gate times were typically between 5 and 10 ns to capture the entire laser pulse, though the camera gate could be reduced to 2 ns gate times if continuum radiation was a problem. This setup gives a useful spatial picture of what is happening within a single experiment. However, it does not give any temporal information about the plasma during the laser pulse.

To record temporal information about the plasma a streak camera was used to record the scattered spectrum, instead of the gated ICCD camera. The streak camera causes the collected light from different moments in time to appear at different location in the "time direction" in the image. Using a full sweep time of either 10 or 20 ns enables 150 ps or 250 ps time resolution, respectively, of the scattered light spectral profile.

A disadvantage of using a streak camera to record the spectrum, however, is that only one spatial location is viewed. To enable recording time-resolved scattered radiation from two different locations a non-traditional setup can be used to couple the fibers into the spectrometer [49]. This setup involves rotating the fiber, so the linear array is perpendicular to the spectral slit. The spectral

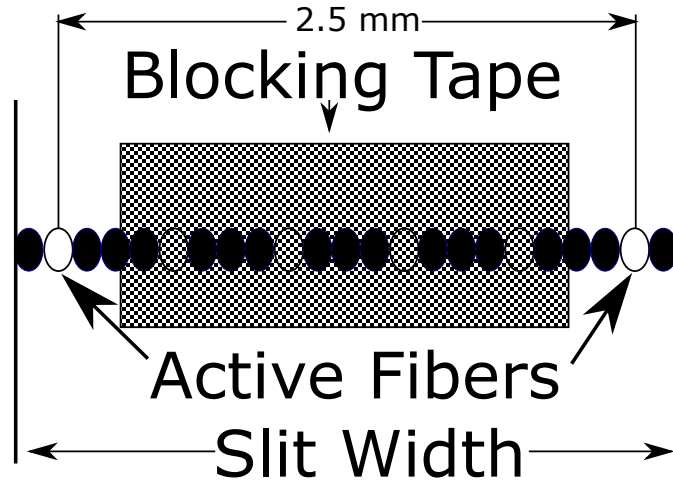


Figure 2.9: Schematic of the setup to allow light from two fibers to enter the spectrometer. This setup is shown with four fibers being blocked by the tape.

slit is then open wide enough that light from multiple fibers passed through it. To ensure that the spectrum from the fibers were clearly resolvable, several of the middle fibers were blocked by a piece of tape, shown in Fig. 2.9. For observing the ion acoustic feature, it was seen that blocking between 3 and 4 middle fibers would allow the spectrum from two fibers to be recorded without overlap. Greater separation than 5 fibers was not possible due to the limits of the size of the spectral entrance slit. Therefore, this method could only be used to record spectra from two fibers simultaneously. These two fibers could be set up to either collect from different volumes of plasma, or, as done in this thesis, using 2 different scattering angles and the split fiber bundle.

CHAPTER 3

THOMSON SCATTERING THEORY

3.1 Overview

A very important diagnostic technique in plasma physics that we have already introduced, and a primary subject of this thesis, is Thomson scattering. Thomson scattering, the elastic-scattering of electromagnetic radiation off of an electron, can simultaneously measure several local plasma parameters. Though a detailed description of Thomson scattering relative to our plasma will be provided here, the reader is directed to the literature for more information [25, 20, 39, 17]. For consistency with the principal references used here, CGS units have been used unless otherwise noted, except that temperatures are in eV.

The simplest place to start a description of Thomson scattering is the scattering of a monochromatic plane wave off of a single low velocity ($v/c \ll 1$) charged particle. We can then extend the scattering of the wave to a volume of plasma. A schematic of the key vectors for the single particle scattering case is shown in Fig. 3.1. Since we are observing these effects at some distance R' from the particle, we are interested in the state of the particle at some retarded time,

$$t' = t - (R'/c). \quad (3.1)$$

We will describe the position and velocity of this particle with a charge, q , and mass, m , as $\mathbf{r}(t')$ and $\mathbf{v}(t')$. The incident plane wave can be described by

$$\mathbf{E}_l(\mathbf{r}, t') = \mathbf{E}_{l0} \cos(\mathbf{k}_l \cdot \mathbf{r}(t') - \omega_l t'), \quad \mathbf{B}_l(\mathbf{r}, t') = \hat{l} \times \mathbf{E}_l, \quad (3.2)$$

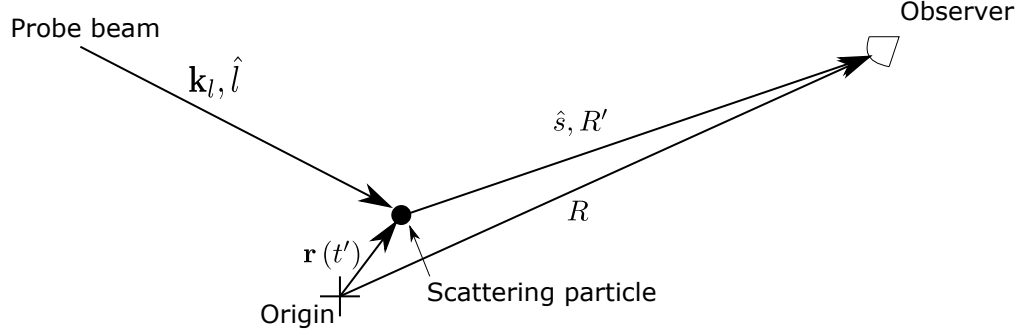


Figure 3.1: Figure of a single particle scattering system.

where the laser wave number, wavelength and frequency are indicated by $k_l = 2\pi/\lambda_l$, λ_l , and ω_l . To find the power scattered from this charged particle, the acceleration of the charge due to the plane wave must be determined. Taking the Lorentz force equation

$$m \frac{d\mathbf{v}}{dt'} = q \left(\mathbf{E}_l(t') + \frac{\mathbf{v}(t')}{c} \times \mathbf{B}_l(t') \right), \quad (3.3)$$

and ignoring the magnetic field contribution since we are assuming $v/c \ll 1$, gives [25]

$$m \frac{d\mathbf{v}}{dt'} = q \mathbf{E}_{l0} \cos [\mathbf{k}_l \cdot \mathbf{r}(t') - \omega_l t']. \quad (3.4)$$

The location of the electron can be described as

$$\mathbf{r}(t') = \mathbf{r}(0) + \mathbf{v}t'. \quad (3.5)$$

Since $R' \approx R - \hat{s} \cdot \mathbf{r}(t')$ (as $R \gg \mathbf{r}(t')$), we can approximate the retarded time as,

$$t' \approx t - \frac{|R - \hat{s} \cdot \mathbf{r}(t')|}{c}. \quad (3.6)$$

Now by substituting Eq. 3.5 into Eq. 3.6 and solving for t' gives

$$t' = \left(t - \frac{R}{c} + \frac{\hat{s} \cdot \mathbf{r}(0)}{c} \right) / (1 - \hat{s} \cdot \boldsymbol{\beta}), \quad (3.7)$$

where $\boldsymbol{\beta} = \mathbf{v}/c$. Plugging this into the cos term of Eq. 3.4 gives

$$\mathbf{k}_l \cdot \mathbf{r}(t') - \omega_l t' = k_s R - \omega_s t - (\mathbf{k}_s - \mathbf{k}_l) \cdot \mathbf{r}(0), \quad (3.8)$$

where we have defined the following

$$\omega_s = \omega_l \frac{1 - \hat{l} \cdot \boldsymbol{\beta}}{1 - \hat{s} \cdot \boldsymbol{\beta}} \text{ and } \mathbf{k}_s = \frac{\omega_s}{c} \hat{s}. \quad (3.9)$$

We can now work in terms of the shift in frequency, ω , and wave-vector \mathbf{k} which are defined as

$$\omega = \omega_s - \omega_l, \quad (3.10)$$

$$\mathbf{k} = \mathbf{k}_s - \mathbf{k}_l, \quad (3.11)$$

which are statements of conservation of energy and momentum, respectively. With these definitions, it can be shown that ω is related to the Doppler shift of the particle along \mathbf{k}

$$\omega = \mathbf{k}_s \cdot \mathbf{v} - \mathbf{k}_l \cdot \mathbf{v} = \mathbf{k} \cdot \mathbf{v}. \quad (3.12)$$

Therefore, by measuring the frequency of the scattered radiation, it is possible to know the velocity of the particle along \mathbf{k} .

The equations for the electric field and power from an accelerating charge can be found in literature (Jackson pg.665) [40]

$$E_s(R, t) = \frac{q}{cR} \left[\hat{s} \times (\hat{s} \times \dot{\boldsymbol{\beta}}) \right], \quad (3.13)$$

$$\frac{dP_s}{d\Omega} = \frac{cR^2}{4\pi} E_s^2. \quad (3.14)$$

Solving for $\dot{\mathbf{v}}$ from Eq. 3.4) gives the scattered field and power from a single charge as

$$E_s(R, t) = \frac{q^2}{c^2 m R} \left[\hat{s} \times (\hat{s} \times \mathbf{E}_{l0}) \right] \cos(k_s R - \omega_s t - \mathbf{k} \cdot \mathbf{r}(0)), \quad (3.15)$$

$$\frac{dP_s}{d\Omega} = \frac{q^4 E_{l0}^2}{4\pi c^3 m^2} \left[\hat{s} \times (\hat{s} \times \hat{E}_{l0}) \right]^2 \cos^2(k_s R - \omega_s t - \mathbf{k} \cdot \mathbf{r}(0)). \quad (3.16)$$

Focusing now only on electrons, because of the clear mass dependence in the scattered power, the time averaged scattered power in the unit solid angle, $d\Omega$, from a single electron is

$$\frac{\overline{dP_s(\mathbf{R})}}{d\Omega} = \frac{cE_{l0}^2 r_0^2}{8\pi} \left[\hat{s} \times (\hat{s} \times \hat{E}_{l0}) \right]^2, \quad (3.17)$$

where $r_0 = e^2/m_e c^2$ is the classical electron radius. The ending term is related to the scattering angle, θ , and the angle between \mathbf{E}_{l0} and the projection of \mathbf{k}_s onto the plane of the laser, ϕ ,

$$\left[\hat{s} \times (\hat{s} \times \hat{E}_{l0}) \right]^2 = 1 - \sin^2 \theta \cos^2 \phi. \quad (3.18)$$

Now integrating the scattered power over all viewing angles, and comparing that to the incident intensity, $P_l/A = \frac{cE_l^2}{8\pi}$ gives the Thomson cross section

$$\sigma_T = \frac{8\pi}{3} r_0^2 = 6.65 \times 10^{-25} \text{cm}^2. \quad (3.19)$$

We now see that a big challenge in Thomson scattering is getting enough scattered signal as the scattering cross section is so small.

While this single particle picture is useful for the foundation of the scattered power, we are interested in scattered signal from a plasma. Assuming there is negligible attenuation, so that each electron sees the same intensity of the incident wave, as well as that the laser does not perturb the plasma, the total scattered electric field is the vector sum of scattered electric fields from each electron, where N is the number of electrons in the scattering volume. This therefor, gives a total scattered power of

$$\frac{dP_s}{d\Omega} = \frac{cR^2}{4\pi} \sum_{i=1}^N \mathbf{E}_{is} \cdot \sum_{j=1}^N \mathbf{E}_{js}, \quad (3.20)$$

which can be rewritten as

$$\frac{dP_s}{d\Omega} = \frac{cR^2}{4\pi} N E_s^2 + \frac{cR^2}{4\pi} N(N-1) \overline{(\mathbf{E}_i \cdot \mathbf{E}_j)_{i \neq j}}, \quad (3.21)$$

by separating the terms for which $i = j$ and $i \neq j$. The first term here is the power scattered from randomly distributed electrons, while the second term is non-zero if the positions of the electrons are correlated. The primary source of scattering, random electrons or correlated electrons, is determined by $\alpha = 1/k\lambda_{De}$, where $\lambda_{De} = \sqrt{T_e/4\pi n_e e^2}$ is the electron Debye length. When $\alpha \ll 1$, the non-collective regime, the observed plasma fluctuations are small compared to the Debye shielding length, and therefore the electrons appear random and uncorrelated. The collective regime occurs when $\alpha \gtrsim 1$, and in this region the observed plasma fluctuations are on a similar scale to, or larger than the Debye shielding length. In this case the scattering is primarily from correlated electrons within the plasma, and we are observing the effects of plasma waves. For our laser wavelength of 526.5 nm and for scattering at 90° degrees α can be estimated by

$$\alpha \approx 8 \sqrt{n_e[10^{18}\text{cm}^{-3}]/T_e[\text{eV}]}.$$
 (3.22)

For our plasmas, typically around $n_e = 5 \times 10^{18} \text{ cm}^{-3}$ and $T_e = 20 \text{ eV}$, $\alpha \approx 4$, which puts us in the collective regime. Though the non-collective region is commonly used for electron density and electron temperature measurements in lower-density plasma (for example, [51, 52]), because α for our plasmas is over 1, we are interested in collective regime measurements in this thesis. Therefore, in the discussion that follows, we will focus our attention on the scattered spectral profile in the collective regime.

Now that the power scattered from each individual particle is known, and the total scattered power is just the vector sum of the scattering from all particles, it is now time to build up the scattering problem for a volume of plasma.

We now define an arbitrary distribution function for particles of species σ by

$$F_\sigma(\mathbf{r}, \mathbf{v}, t') = \sum_{s=1}^N \delta(\mathbf{r} - \mathbf{r}_s(t')) \delta(\mathbf{v} - \mathbf{v}_s(t')). \quad (3.23)$$

We can take the first velocity moment of this distribution function to find the density

$$n_\sigma(\mathbf{r}, t') = \int F_\sigma(\mathbf{r}, \mathbf{v}, t') d\mathbf{v}. \quad (3.24)$$

The total scattered electric field, E_s^T can be expressed as the sum of the scattering from each electron

$$E_s^T(R, t) = \int d\mathbf{r} n_e(\mathbf{r}, t') E_s(r, t), \quad (3.25)$$

where E_s is the scattering from a single particle found earlier, Eq. 3.15, and we are still assuming the low velocity limit. Plugging this into the total scattered power, and taking the time average, which we take over infinite time by assuming that the time scale of the observation is much greater than the coherence time of the plasma fluctuations, gives

$$\frac{\partial P_s}{\partial \Omega} = \frac{cR^2}{4\pi} \lim_{T \rightarrow \infty} \frac{1}{T} \int_{-\infty}^{\infty} dt |E_s^T(R, t)|^2. \quad (3.26)$$

Since we are interested in observing the scattered radiation over a particular frequency range we can use Parseval's theorem to go between the time and frequency domains, $\int_{-\infty}^{\infty} dt |x(t)|^2 = \frac{1}{2\pi} \int_{-\infty}^{\infty} d\omega |x(\omega)|^2$. Taking the Fourier transform of the scattered electric field,

$$E_s^T(\omega_s) = \int_{-\infty}^{\infty} dt E_s^T(t) e^{-i\omega_s t}, \quad (3.27)$$

gives

$$\frac{\partial P_s}{\partial \Omega} = \frac{cR^2}{4\pi} \lim_{T \rightarrow \infty} \frac{1}{2\pi T} \int_{-\infty}^{\infty} d\omega_s \left| \int_{-\infty}^{\infty} dt E_s^T(R, t) e^{-i\omega_s t} \right|^2. \quad (3.28)$$

Since we are in the low velocity limit, we can say that $dt = dt'$. Rewriting the integral in terms of t' and plugging in the value for E_s^T makes the integral over t

become,

$$\int_{-\infty}^{\infty} dt' \int d\mathbf{r} n_e(\mathbf{r}, t') \frac{e^2 E_{l0}}{c^2 m_e R} \left[\hat{s} \times (\hat{s} \times \hat{E}_{l0}) \right] \times \cos(\mathbf{k}_l \cdot \mathbf{r}(t') - \omega_l t') \exp \left[-i\omega_s \left(t' - \frac{\hat{s} \cdot \mathbf{r}(t')}{c} + \frac{R}{c} \right) \right]. \quad (3.29)$$

Now we are interested in taking the Fourier time and space transformation of the density

$$n_e(\mathbf{r}, t') = \int d\mathbf{k} \int d\omega \frac{n_e(\mathbf{k}, \omega)}{(2\pi)^4} e^{-i(\mathbf{k} \cdot \mathbf{r}(t') - \omega t')}. \quad (3.30)$$

Using this, and the fact that $\cos(x) = \frac{1}{2}(e^{-ix} + e^{ix})$ allows us to rewrite Eq. 3.29 as a sum of two terms that have the following exponents

$$i \left[(\omega - (\omega_s - \omega_l))t' - (\mathbf{k} - (\mathbf{k}_s - \mathbf{k}_l)) \cdot \mathbf{r}(t') - \frac{\omega_s}{c} R \right], \quad (3.31)$$

$$i \left[(\omega - (\omega_s + \omega_l))t' - (\mathbf{k} - (\mathbf{k}_s + \mathbf{k}_l)) \cdot \mathbf{r}(t') - \frac{\omega_s}{c} R \right], \quad (3.32)$$

where $\mathbf{k}_s = \frac{\omega_s \hat{s}}{c}$. Looking at the first of these two functions and taking the integral over t' gives a delta function $2\pi\delta[\omega - (\omega_s - \omega_l)]$, and the integral over \mathbf{r} gives the delta function $(2\pi)^3\delta[\mathbf{k} - (\mathbf{k}_s - \mathbf{k}_l)]$. This means that after integrating $n(\mathbf{k}, \omega)$ over \mathbf{k} and ω we will get $n_e(\mathbf{k}_s - \mathbf{k}_l, \omega_s - \omega_l)$. Similar arguments can be used for the second term, which gives a scattered power of

$$\frac{\partial P_s}{\partial \Omega} = \frac{c E_{l0}^2 r_0^2}{4\pi} \left[\hat{s} \times (\hat{s} \times \hat{E}_{l0}) \right]^2 \lim_{T \rightarrow \infty} \frac{1}{8\pi T} \times \int_{-\infty}^{\infty} d\omega_s |n_e(\mathbf{k}_s - \mathbf{k}_l, \omega_s - \omega_l) + n_e(\mathbf{k}_s + \mathbf{k}_l, \omega_s + \omega_l)|^2. \quad (3.33)$$

We are interested in the ensemble average of the electrons since it is impossible to model the exact state of the system. We define the ensemble average for some parameter X as

$$\langle X \rangle \equiv \frac{\text{all } q \int dq X(q) P(q)}{\text{all } q \int dq P(q)}, \quad (3.34)$$

where $P(q)$ is the probability of being in a state q , and we are interested in averaging over \mathbf{r} and \mathbf{v} , which are the electron positions and velocities. When taking the ensemble average the cross-density term drops out, giving

$$\begin{aligned} \frac{\partial P_s}{\partial \Omega} &= \frac{P_l r_0^2}{A4\pi} \left[\hat{s} \times (\hat{s} \times \hat{E}_{l0}) \right]^2 \lim_{T \rightarrow \infty} \frac{1}{T} \\ &\times \int_{-\infty}^{\infty} d\omega_s \langle |n_e(\mathbf{k}_s - \mathbf{k}_l, \omega_s - \omega_l)|^2 \rangle + \langle |n_e(\mathbf{k}_s + \mathbf{k}_l, \omega_s + \omega_l)|^2 \rangle. \end{aligned} \quad (3.35)$$

Since $|n_e(\mathbf{k}, \omega)|^2 = |n_e(-\mathbf{k}, -\omega)|^2$ we can combine the two density terms in order to get

$$\frac{\partial P_s}{\partial \Omega} = \frac{P_l r_0^2}{A4\pi} \left[\hat{s} \times (\hat{s} \times \hat{E}_{l0}) \right]^2 \lim_{T \rightarrow \infty} \frac{1}{T} \int_{-\infty}^{\infty} d\omega_s 2 \langle |n_e(\mathbf{k}_s - \mathbf{k}_l, \omega_s - \omega_l)|^2 \rangle. \quad (3.36)$$

By using $\mathbf{k} = \mathbf{k}_s - \mathbf{k}_l$ and $\omega = \omega_s - \omega_l$ as well as differentiating with respect to ω_s we can find the scattered power per unit scattering frequency along a scattering length of L , which is

$$\frac{\partial^2 P_s}{\partial \Omega \partial \omega_s} = \frac{P_l r_0^2 L}{2\pi} \left[\hat{s} \times (\hat{s} \times \hat{E}_{l0}) \right]^2 n_{e0} S(\mathbf{k}, \omega). \quad (3.37)$$

In this equation $S(\mathbf{k}, \omega)$ is called the spectral density function and is defined as

$$S(\mathbf{k}, \omega) \equiv \lim_{T \rightarrow \infty, V \rightarrow \infty} \frac{1}{VT} \left\langle \frac{|n_e(\mathbf{k}, \omega)|^2}{n_{e0}} \right\rangle, \quad (3.38)$$

where n_{e0} is the mean electron density, and V is the scattering volume.

While this serves as a good introduction to how the scattering problem works, there are several key additions that need to be made before going further. The first is that the full problem needs to be solved with a Laplace transform in time instead of a Fourier transform. This is due to the poles in the susceptibility, χ_{σ} , to be discussed shortly (see Eq. 3.57), which would make the form factor ill-defined if only Fourier transforms were used. Approaching the problem in this manner causes the spectral density function to be rewritten as [25]

$$S(\mathbf{k}, \omega) \equiv \lim_{\gamma \rightarrow 0} \frac{2\gamma}{V} \left\langle \frac{|n_e(\mathbf{k}, \omega - i\gamma)|^2}{n_{e0}} \right\rangle. \quad (3.39)$$

The second necessary correction is to account for lowest order relativistic effects. Assuming $(v/c)^2 \ll 1$, it can be shown that the only correction needed is a $(1 + 2\frac{\omega}{\omega_l})$ term in the scattered power [25]. This results in the scattered power from the plasma being

$$\frac{\partial^2 P_s}{\partial \Omega \partial \omega_s} = \frac{P_l r_0^2 L}{2\pi} \left(1 + 2\frac{\omega}{\omega_l}\right) [\hat{s} \times (\hat{s} \times \hat{E}_{l0})]^2 n_{e0} S(\mathbf{k}, \omega). \quad (3.40)$$

This correction affects the intensity of the high frequency modes and accounts for any small order relativistic effects that occur in our plasmas. As a reminder, $\omega = \omega_s - \omega_l$, and therefore, is the shift relative to the laser frequency.

Now having solved for the power scattered in terms of the form factor, or spectral density function, $S(\mathbf{k}, \omega)$, we now need to solve for the fluctuations in the electron density, $n_e(\mathbf{k}, \omega)$. One approach follows a method similar to the solution to the Landau problem [25]. Other methods include solving the Nyquist fluctuation-dissipation theorem [18] or the method of ‘dressed test particles’ [20]. We now will derive the fluctuations in density for a collisionless, non-relativistic plasma without the influence of a magnetic field using Klimontovich equation, following the procedure of Landau’s problem, and show the resulting form factor [25]. To solve this problem, we need three fundamental equations: Klimontovich Equation, Lorentz force equation (ignoring the $\mathbf{v} \times \mathbf{B}$ as we assume no influence from the magnetic field), and Poisson equation

$$\frac{\partial F_\sigma}{\partial t} + \mathbf{v} \cdot \frac{\partial F_\sigma}{\partial \mathbf{r}} + \mathbf{a} \cdot \frac{\partial F_\sigma}{\partial \mathbf{v}} = 0, \quad (3.41)$$

$$\mathbf{a} = (q/m)\mathbf{E}, \quad (3.42)$$

$$\nabla^2 \phi = - \sum_{\sigma} 4\pi n_{\sigma}. \quad (3.43)$$

Where F_σ and n_σ follow the same definitions as Eq. 3.23 and Eq. 3.24 and $\phi(\mathbf{r}, t)$ is the electrostatic potential. We will now linearize these equations terminating

at two-particle interactions. For this linearization we will define

$$F_{1\sigma}(\mathbf{r}, \mathbf{v}, t) = F_{\sigma}(\mathbf{r}, \mathbf{v}, t) - F_{0\sigma}(\mathbf{v}), \quad (3.44)$$

and

$$n_{1\sigma}(\mathbf{r}, t) = n_{\sigma}(\mathbf{r}, t) - n_{0\sigma}, \quad (3.45)$$

where $F_{0\sigma}$ and $n_{0\sigma}$ are the mean levels. Linearizing the fundamental equations above gives

$$\frac{\partial F_{0\sigma}}{\partial t} + \mathbf{v} \cdot \frac{\partial F_{0\sigma}}{\partial \mathbf{r}} = 0, \quad (3.46)$$

$$\frac{\partial F_{1\sigma}}{\partial t} + \mathbf{v} \cdot \frac{\partial F_{1\sigma}}{\partial \mathbf{r}} + \frac{q}{m} \mathbf{E}_1 \cdot \frac{\partial F_{0\sigma}}{\partial \mathbf{v}} = 0, \quad (3.47)$$

$$\nabla^2 \phi_1 = - \sum_{\sigma} 4\pi n_{1\sigma}, \quad \mathbf{E}_0 = 0. \quad (3.48)$$

In these equations for electrons $q = -e$, $m = m_e$, and $F_{0\sigma}(\mathbf{v}) = n_{0e} f_{0e}(\mathbf{v})$, and for ions $q = Ze$, $m = m_i$, and $F_{0\sigma}(\mathbf{v}) = (n_{0e}/Z) f_{0i}(\mathbf{v})$, where f_{0e} and f_{0i} are the single particle mean distribution functions.

To solve these equations, we will need to take the Fourier transform in space and Laplace transform in time of various functions. For an arbitrary function, $A(\mathbf{r}, t)$, we will define these transforms as

$$A(\mathbf{k}, \omega - i\gamma) = \int_0^{\infty} dt e^{-(i\omega + \gamma)t} \int_{-\infty}^{\infty} d\mathbf{r} e^{i\mathbf{k}\cdot\mathbf{r}} A(\mathbf{r}, t), \quad (3.49)$$

and the inverse

$$A(\mathbf{r}, t) = \int_0^{\infty} \frac{d\omega}{2\pi} e^{(i\omega + \gamma)t} \int_{-\infty}^{\infty} \frac{d\mathbf{k}}{(2\pi)^3} e^{-i\mathbf{k}\cdot\mathbf{r}} A(\mathbf{k}, \omega - i\gamma). \quad (3.50)$$

We will first solve for the perturbed electric field from Poisson's equation and then use that in Klimontovich equation to find the fluctuations in density. The potential of the plasma is given by

$$\nabla^2 \phi_1(\mathbf{r}, t) = -4\pi(Zen_{1i} - en_{1e}) = -4\pi\rho_1(\mathbf{r}, t) \quad (3.51)$$

where ρ_1 is the charge density. Rewriting the charge density in terms of its Fourier transform and then integrating the equation over \mathbf{r} gives

$$\phi_1(\mathbf{r}, t) = \frac{4\pi}{(2\pi)^3} \int_{-\infty}^{\infty} d\mathbf{k} \rho_1(\mathbf{k}, t) \frac{e^{-i\mathbf{k}\cdot\mathbf{r}}}{k^2}. \quad (3.52)$$

This allows us to write the perturbed electric field, $\mathbf{E}_1 = -\nabla\phi_1$, as

$$\mathbf{E}_1(\mathbf{r}, t) = \frac{4\pi i}{(2\pi)^3} \int_{-\infty}^{\infty} d\mathbf{k} \frac{\mathbf{k}}{k^2} \rho_1(\mathbf{k}, t) e^{-i\mathbf{k}\cdot\mathbf{r}}. \quad (3.53)$$

The next step is to substitute this for the electric field and take the Fourier-Laplace transform of Eq. 3.47. It should be noted that since the system is assumed to be stationary, $F_{0\sigma}$ is not a function of time, and therefore, by Eq. 3.46, not of position either. This allows us to write Eq. 3.47 as

$$-F_{1\sigma}(\mathbf{k}, \mathbf{v}, 0) + (i\omega + \gamma - i\mathbf{k})F_{1\sigma}(\mathbf{k}, \mathbf{v}, \omega - i\gamma) + \frac{4\pi q i}{mk^2} \rho_1(\mathbf{k}, \omega - i\gamma) \mathbf{k} \cdot \frac{\partial F_{0\sigma}(\mathbf{v})}{\partial \mathbf{v}} = 0. \quad (3.54)$$

Which can be solved for $F_{1\sigma}(\mathbf{k}, \mathbf{v}, \omega - i\gamma)$ to give

$$F_{1\sigma}(\mathbf{k}, \mathbf{v}, \omega - i\gamma) = \frac{-iF_{1\sigma}(\mathbf{k}, \mathbf{v}, 0) - \frac{4\pi q}{mk^2} \rho_1(\mathbf{k}, \omega - i\gamma) \mathbf{k} \cdot \frac{\partial F_{0\sigma}(\mathbf{v})}{\partial \mathbf{v}}}{\omega - \mathbf{k} \cdot \mathbf{v} - i\gamma}. \quad (3.55)$$

This equation can then be integrated over velocity space to find the fluctuating density of the species

$$n_{1\sigma}(\mathbf{k}, \omega - i\gamma) = -i \sum_{j=1}^{N_\sigma} \frac{e^{i\mathbf{k}\cdot\mathbf{r}_j(0)}}{\omega - \mathbf{k} \cdot \mathbf{v}_j(0) - i\gamma} + \frac{\chi_\sigma(\mathbf{k}, \omega - i\gamma)}{q} \rho_1(\mathbf{k}, \omega - i\gamma). \quad (3.56)$$

Here χ_σ is the susceptibility of the species, which is defined as

$$\chi_\sigma(\mathbf{k}, \omega - i\gamma) = \int_{-\infty}^{\infty} d\mathbf{v} \frac{4\pi q^2 n_\sigma}{mk^2} \frac{\mathbf{k} \cdot \frac{\partial f_{0\sigma}}{\partial \mathbf{v}}}{\omega - \mathbf{k} \cdot \mathbf{v} - i\gamma}. \quad (3.57)$$

We will also define the dielectric function as $\epsilon = 1 + \chi_e + \chi_i$. Plugging the density of each species back into the equation for charge density allows us to solve for

the fluctuating electron density

$$n_{1e}(\mathbf{k}, \omega - i\gamma) = -i \left[\sum_{j=1}^N \frac{e^{i\mathbf{k}\cdot\mathbf{r}_j(0)}}{\omega - \mathbf{k}\cdot\mathbf{v}_j(0) - i\gamma} - \frac{\chi_e}{\epsilon} \sum_{j=1}^N \frac{e^{i\mathbf{k}\cdot\mathbf{r}_j(0)}}{\omega - \mathbf{k}\cdot\mathbf{v}_j(0) - i\gamma} + \frac{Z\chi_e}{\epsilon} \sum_{l=1}^{N/Z} \frac{e^{i\mathbf{k}\cdot\mathbf{r}_l(0)}}{\omega - \mathbf{k}\cdot\mathbf{v}_l(0) - i\gamma} \right]. \quad (3.58)$$

We now have the fluctuating electron density spectrum expressed as a sum of three terms. Before plugging this density into the form factor, several things can be noted about each term in this density. The first term is scattering from electrons that are not affected by other particles in the plasma. The second and third terms scale as χ_e/ϵ , which can be shown to be proportional to α^2 . Therefore, when $\alpha^2 \ll 1$, the first term will dominate the spectrum, which leads to the non-collective scattering spectrum. The second and third terms are a result of electrons trying to shield either a test electron or ion, respectively. Thus, these terms include correlations in the plasma and result in the collective scattering spectrum.

We are now interested in finding the form factor that was defined by Eq. 3.39. Since n_{0e} does not fluctuate, it does not affect the ensemble average of the density fluctuations. Therefore,

$$S(\mathbf{k}, \omega) = \lim_{\gamma \rightarrow 0} \frac{2\gamma}{Vn_{0e}} \left\langle \left| \left(1 - \frac{\chi_e}{\epsilon} \right) \sum_{j=1}^N \frac{-ie^{i\mathbf{k}\cdot\mathbf{r}_j(0)}}{\omega - \mathbf{k}\cdot\mathbf{v}_j(0) - i\gamma} - \left(\frac{Z\chi_e}{\epsilon} \right) \sum_{l=1}^{N/Z} \frac{ie^{i\mathbf{k}\cdot\mathbf{r}_l(0)}}{\omega - \mathbf{k}\cdot\mathbf{v}_l(0) - i\gamma} \right|^2 \right\rangle. \quad (3.59)$$

In order to proceed, we will now assume that the charges are initially uncorrelated to simplify the problem. This assumption may seem inconsistent with the problem at hand as we are trying to look for collective effects of the charges. However, if the integration time, T , is much greater than the plasma time, $1/\omega_{pe}$, accounting for the charges being correlated will have the same result as this dis-

cussion [25]. With initially uncorrelated charges, then, the ensemble average of the cross terms goes to zero [25], which allows us to write

$$S(\mathbf{k}, \omega) = \lim_{\gamma \rightarrow 0} \frac{2\gamma}{Vn_{0e}} \left\langle \left| 1 - \frac{\chi_e}{\epsilon} \right|^2 \sum_{j=1}^N \frac{e^{i\mathbf{k} \cdot \mathbf{r}_j(0)}}{\omega - \mathbf{k} \cdot \mathbf{v}_j(0) - i\gamma} \sum_{m=1}^N \frac{e^{-i\mathbf{k} \cdot \mathbf{r}_m(0)}}{\omega - \mathbf{k} \cdot \mathbf{v}_m(0) + i\gamma} + \left| Z \frac{\chi_e}{\epsilon} \right|^2 \sum_{l=1}^{N/Z} \frac{e^{i\mathbf{k} \cdot \mathbf{r}_l(0)}}{\omega - \mathbf{k} \cdot \mathbf{v}_l(0) - i\gamma} \sum_{n=1}^{N/Z} \frac{e^{-i\mathbf{k} \cdot \mathbf{r}_n(0)}}{\omega - \mathbf{k} \cdot \mathbf{v}_n(0) + i\gamma} \right\rangle. \quad (3.60)$$

Initially uncorrelated charges also allow us to drop the terms where $j \neq m$ and $l \neq n$, as their ensemble average will be zero. Looking now at just the first term when $j = m$

$$\lim_{\gamma \rightarrow 0} \frac{2\gamma}{Vn_{0e}} \left| 1 - \frac{\chi_e}{\epsilon} \right|^2 \left\langle N \frac{1}{(\omega - \mathbf{k} \cdot \mathbf{v}(0))^2 + \gamma^2} \right\rangle. \quad (3.61)$$

The ensemble average of this can then be found by multiplying by the probability to be in the various velocities states, $f_{0e}(\mathbf{v})$, and then integrating over velocity space

$$\lim_{\gamma \rightarrow 0} \frac{2\gamma}{Vn_{0e}} \left| 1 - \frac{\chi_e}{\epsilon} \right|^2 N \int_{-\infty}^{\infty} d\mathbf{v} \frac{f_{0e}(\mathbf{v})}{(\omega - \mathbf{k} \cdot \mathbf{v}(0))^2 + \gamma^2}. \quad (3.62)$$

This integral is solvable analytically [25] allowing us to rewrite this equation as

$$\lim_{\gamma \rightarrow 0} \frac{2\gamma}{Vn_{0e}} \left| 1 - \frac{\chi_e}{\epsilon} \right|^2 N \frac{\pi f_{0e}(\omega/k)}{k\gamma}, \quad (3.63)$$

where $f_{0e}(\omega/k)$ represents the one-dimensional electron velocity distribution along the \mathbf{k} direction. Simplifying this ($N/V = n_{0e}$), and then doing a similar thing for the ion distribution in the second term, allows us to write the general form of the form factor for a plasma with a single ion species as

$$S(\mathbf{k}, \omega) = \frac{2\pi}{k} \left| 1 - \frac{\chi_e}{\epsilon} \right|^2 f_{0e} \left(\frac{\omega}{k} \right) + \frac{2\pi Z}{k} \left| \frac{\chi_e}{\epsilon} \right|^2 f_{0i} \left(\frac{\omega}{k} \right). \quad (3.64)$$

The form factor is challenging to solve due to the poles in χ_e and χ_i . However, a Maxwellian distribution function, which is a reasonable approximation of a plasma close to thermodynamic equilibrium, can lead to a numeric solution to

these equations. The Maxwellian distribution function for the electrons and ions are

$$f_{0e}(v) = \sqrt{\frac{1}{\pi a^2}} \exp(-v^2/a^2) \quad \text{and} \quad f_{0i}(v) = \sqrt{\frac{1}{\pi b^2}} \exp(-v^2/b^2). \quad (3.65)$$

We have allowed electrons and ions to have their own temperatures, and defined their mean thermal speeds as

$$a = \sqrt{\frac{2T_e}{m_e}} \quad \text{and} \quad b = \sqrt{\frac{2T_i}{m_i}}. \quad (3.66)$$

Using this, χ_e and χ_i can be related to the plasma dispersion function, $Z(x)$ [23], by

$$\chi_e(\mathbf{k}, \omega) = -\frac{\alpha^2}{2} Z'(x_e), \quad (3.67)$$

$$\chi_i(\mathbf{k}, \omega) = -\frac{\alpha^2}{2} \frac{ZT_e}{T_i} Z'(x_i), \quad (3.68)$$

where

$$x_e = \omega/ka \quad \text{and} \quad x_i = \omega/kb. \quad (3.69)$$

The numerical solution to the plasma dispersion will be discussed in Sec. 3.4, and a plot of the real and imaginary parts of $W(x) \equiv -Z'(x)/2$ is shown in Fig. 3.2. Using this we can now show that the solution for the form factor under a Maxwellian distribution is

$$S(\mathbf{k}, \omega) = \frac{2\sqrt{\pi}}{ka} \left| \frac{1 + \alpha^2 \frac{ZT_e}{T_i} W(x_i)}{\epsilon} \right|^2 e^{-x_e^2} + \frac{2\sqrt{\pi}Z}{kb} \left| \frac{\alpha^2 W(x_e)}{\epsilon} \right|^2 e^{-x_i^2}, \quad (3.70)$$

with

$$\epsilon = 1 + \alpha^2 W(x_e) + \alpha^2 \frac{ZT_e}{T_i} W(x_i). \quad (3.71)$$

This complete form factor, though numerically solvable (see Sec. 3.4), is very complicated, making it hard to get an intuitive picture of how different plasma features affect the Thomson scattering spectral profile. At least around the resonances (when $\epsilon = 0$), $S(\mathbf{k}, \omega)$ can be broken into two terms, one that is a function

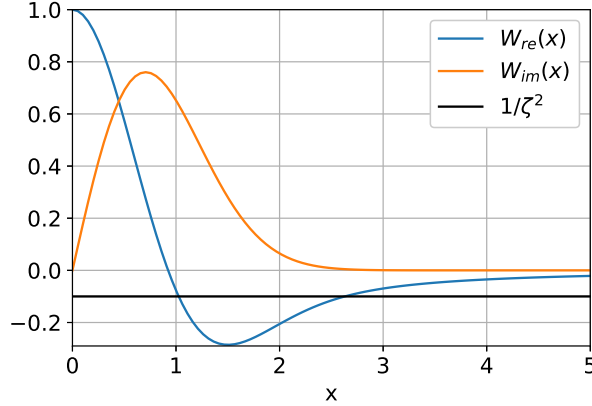


Figure 3.2: A plot showing the real and imaginary parts of W , and where the resonances will occur for an arbitrary value of ζ . ζ is the subscript of the $\Gamma_\zeta(x)$ function, Eq. 3.75, and is either α or β , see Eq. 3.76, based on whether we are looking at the electron or ion term.

of x_e and another a function of x_i . As will be discussed, these two terms will dominate at the high-frequency electron plasma wave and at the low-frequency ion acoustic wave, respectively. This approximation, known as the Salpeter approximation, is very useful for gaining intuition in how the Thomson scattering spectrum depends on various plasma parameters [61].

3.1.1 Salpeter Approximation

The basic idea of the Salpeter approximation is that in the regions of interest, around the resonances, when $\epsilon = 0$, only one of the two terms in Eq. 3.70 will be important. The first (electron) term, which we will label $S_e(\mathbf{k}, \omega)$, dominates in the high-frequency region, while the second (ion) term, which we will label $S_i(\mathbf{k}, \omega)$, dominates for lower frequencies. The ion term falls off at high frequencies due to the $\exp(-x_\sigma^2)$ dependence in each term. Since $x_i \gg x_e$, and in the high frequency regime $x_e > 1$, we can ignore $S_i(\mathbf{k}, \omega)$. In the low frequency

regime, $S_i(\mathbf{k}, \omega)$ dominates, as the exponent terms tend to be similar, allowing the $\frac{kT_i}{m_i} = b \ll a = \frac{kT_e}{m_e}$ difference to be the primary factor in the spectral feature intensity of the two terms.

Looking more closely at the high frequency region of the spectrum, we can make several approximations to remove the ion dependence in the electron term. In this region $x_i \gg x_e \gg 1$, so we can ignore $W(x_i)$, as it will be much smaller than either x_e or 1 (see Fig. 3.2). This, therefore, gives for the electron term,

$$S_e(\mathbf{k}, \omega) \approx \frac{2\sqrt{\pi} \exp(-x_e^2)}{ka \left[(1 + \alpha^2 W_{re}(x_e))^2 + (\alpha^2 W_{im}(x_e))^2 \right]}, \quad (3.72)$$

which has no dependence on x_i .

In the low frequency regime, similar approximations can be made to remove terms with the electron thermal velocity. In this case $x_i \gg 1$, but $x_e \ll 1$ means that $W(x_e) \approx W(0) = 1 + i0$. This means we can rewrite $S_i(\mathbf{k}, \omega)$ as

$$S_i(\mathbf{k}, \omega) \approx \frac{2\sqrt{\pi} Z \alpha^4 \exp(-x_i^2)}{kb \left[(1 + \alpha^2 + \alpha^2 (ZT_e/T_i) W_{re}(x_i))^2 + (\alpha^2 (ZT_e/T_i) W_{im}(x_i))^2 \right]}. \quad (3.73)$$

which has no dependence on x_e .

Now by combining Eq. 3.72 and Eq. 3.73 into one equation, we get the complete Salpeter approximation,

$$S(\mathbf{k}, \omega) \approx \frac{2\sqrt{\pi}}{ka} \Gamma_\alpha(x_e) + \frac{2\sqrt{\pi}}{kb} Z \left(\frac{\alpha^2}{1 + \alpha^2} \right)^2 \Gamma_\beta(x_i), \quad (3.74)$$

where

$$\Gamma_\zeta(x) = \frac{\exp(-x^2)}{\left[(1 + \zeta^2 W_{re}(x))^2 + (\zeta^2 W_{im}(x))^2 \right]}, \quad (3.75)$$

and

$$\beta^2 = \frac{\alpha^2}{1 + \alpha^2} \frac{ZT_e}{T_i}. \quad (3.76)$$

We now have $S(\mathbf{k}, \omega)$ expressed as two terms, where the first term, $S_e(\mathbf{k}, \omega)$, is dependent on x_e and dominates at high frequencies and the second term, $S_i(\mathbf{k}, \omega)$, is dependent on x_i and is important at low frequencies.

Before going into a detailed discussion of both S_e and S_i , we will first discuss the behavior of $\Gamma_\zeta(x)$. In order to try to find the location of the resonances of this function, we need to find the minimum of the denominator, $|\epsilon|^2$, of Γ_ζ . This minimum can be found by setting the real part of ϵ equal to zero. This means that we are solving the following equation

$$1 + \zeta^2 W_{re}(x) = 0, \quad (3.77)$$

or when $W_{re}(x) = -1/\zeta^2$. Figure 3.2 shows a plot of W_{im} , W_{re} , and $1/\zeta^2$. We see that if $1/\zeta^2 < 0.29$ then there are two solutions to this equation. However, the higher x solution has a significantly smaller value for $W_{im}(x)$, meaning it will be the less damped mode and is the solution of interest. Since we are working with large values of x , we can use the $x \gg 1$ approximation for $W_{re}(x)$, which to second order, is [25]

$$W_{re}(x) \approx -\frac{1}{2x^2} \left[1 + \frac{3}{2x^2} \right]. \quad (3.78)$$

Plugging this into the above equation and solving for x gives

$$x^2 = \frac{\zeta^2}{2} \left(1 + \frac{3}{2x^2} \right). \quad (3.79)$$

Now we are interested in the solution to this equation in frequency space. Using x_σ as defined by Eq. 3.69 for x give $x = \frac{\omega}{\sqrt{2}k v_{T\sigma}}$, where $v_{T\sigma} = \sqrt{T_\sigma/m_\sigma}$ is the thermal velocity. In addition, the second term on the right-hand side of Eq. 3.79 is a small correction factor, and therefore we can replace the x^2 there with the first order solution, $x^2 = \zeta^2/2$. Using all of this allows us to estimate the resonance of the peaks as

$$\omega^2 = \zeta^2 k^2 v_{T\sigma}^2 + 3k^2 v_{T\sigma}^2, \quad (3.80)$$

where the ζ^2 term can be replaced by either α^2 or β^2 (from Eq. 3.76) based on the term being studied. This leads to a pair of peaks for the two spectral features as there is both a positive and negative solution for ω .

The next thing of interest to consider is the shape of the profile near the resonance. For this we should note that

$$W_{im}(x) = \sqrt{\pi} x e^{-x^2}. \quad (3.81)$$

This allows rewriting $\Gamma_\zeta(x)$ as

$$\Gamma_\zeta(x) = \frac{e^{-x^2}}{\left[\left(1 - \frac{\zeta^2}{2x^2} \left(1 + \frac{3}{2x^2} \right) \right)^2 + \left(\zeta^2 \sqrt{\pi} x e^{-x^2} \right)^2 \right]}. \quad (3.82)$$

If we say that x_0 is a resonance, and assume that we are near it, we can use x_0 instead of x , except when there is a difference involved, which is the first term of the denominator. Therefore, we can rewrite $\Gamma_\zeta(x)$ as

$$\Gamma_\zeta(x) = \frac{e^{-x_0^2}}{\left[\frac{1}{x_0^4} (x^2 - x_0^2)^2 + \left(\zeta^2 \sqrt{\pi} x_0 e^{-x_0^2} \right)^2 \right]}. \quad (3.83)$$

The first term in the denominator then can be manipulated to put $\Gamma_\zeta(x)$ in the form of a Lorentz profile

$$\Gamma_\zeta \approx \frac{x_0^2 e^{-x_0^2}}{4 \left[(x - x_0)^2 + \left(\frac{\sqrt{\pi}}{2} \zeta^2 x_0^2 e^{-x_0^2} \right)^2 \right]}. \quad (3.84)$$

Being in this form means that the FWHM of the Lorentz profile is

$$\delta x = \sqrt{\pi} \zeta^2 x_0^2 e^{-x_0^2}. \quad (3.85)$$

Expressing this in terms of $\delta\omega$ and ω instead of δx and x_0 , and using the value for the resonance, Eq. 3.80, for ω , results in the frequency space FWHM of the Lorenz profile,

$$\delta\omega = \sqrt{\frac{\pi}{2}} \zeta^2 k v_{T\sigma} (\zeta^2 + 3) e^{-\frac{\zeta^2+3}{2}}. \quad (3.86)$$

So now for either S_e or S_i we have a generic solution to the resonances and the shape of the profile near the resonance. The location of the resonance is given by Eq. 3.80 and the shape is Lorentzian with a FWHM given by Eq. 3.86. It should be noted that these are approximations and that a full numerical solution to the form factor, Eq. 3.70, should be used for actual fitting measurements. The Salpeter approximation however is very useful for building intuition on the primary effects of different plasma parameters, as discussed in the next two sections. The accuracy of these approximations is better for higher values of ζ^2 as it will cause the resonance to occur at a location where the $x \gg 1$ approximation of W_{re} is more valid.

We will now look individually at how each of the terms of this approximation affect the resonances in their respective regions. Though the ion feature, having a resonance at the ion acoustic wave (IAW) frequency, is the stronger feature, and is the focus of most of this work, we will first look at the high-frequency electron feature, which has a resonance at the electron plasma wave (EPW) frequency, as that is the simpler spectrum.

3.2 Electron Plasma Wave

The EPW feature in the TS spectrum arises from the high-frequency resonance and depends primarily on the $S_e(\mathbf{k}, \omega)$ term in the form factor. Thus, it is an effect of the electrons interacting with each other. When looking at the peaks caused by this resonance, we are looking at two features of interest, the location of the peaks and the shape of the peaks. The generic solution to these were found in the previous section (Eq. 3.80 and 3.86), but now we use $\zeta = \alpha$. We also

discuss other things that can affect this profile, and when more complicated theory is needed.

3.2.1 Peak Separation

To find the location of the peaks we need to use Eq. 3.80 with $\zeta^2 = \alpha^2$, and $\alpha > 1$. It should be also noted that $\omega_{pe}\lambda_{De} = v_{Te}$. Plugging these values into Eq. 3.80, we see that the frequency of the EPW is

$$\omega_{EPW}^2 \approx \omega_{pe}^2 + \frac{3T_e}{m_e}k^2. \quad (3.87)$$

This means that the location of the peak depends primarily on the electron density, in the ω_{pe} term, and the second term gives a slight dependence on the electron temperature.

We can now use further approximations to estimate the density of the plasma based on the separation of the two peaks. As most of the plasmas in this thesis are of low temperature, 10-100 eV, we will assume that $\omega_{pe} \gg 3k^2v_{Ti}^2$ and, therefore, we can ignore the second term when estimating the density based on the peak separation. Solving the above equation for the separation of the two EPW peaks in terms of scattered wavelength, $\Delta\lambda_{epw}$, gives

$$\Delta\lambda_{epw} \approx \frac{\omega_{pe}\lambda_l^2}{\pi c} = 16.5 \sqrt{n_e[10^{18}\text{cm}^{-3}]} \text{nm}. \quad (3.88)$$

where the last part is based on our laser wavelength. For a measured peak separation this should give a maximum possible density, as the electron temperature slightly increases the separation.

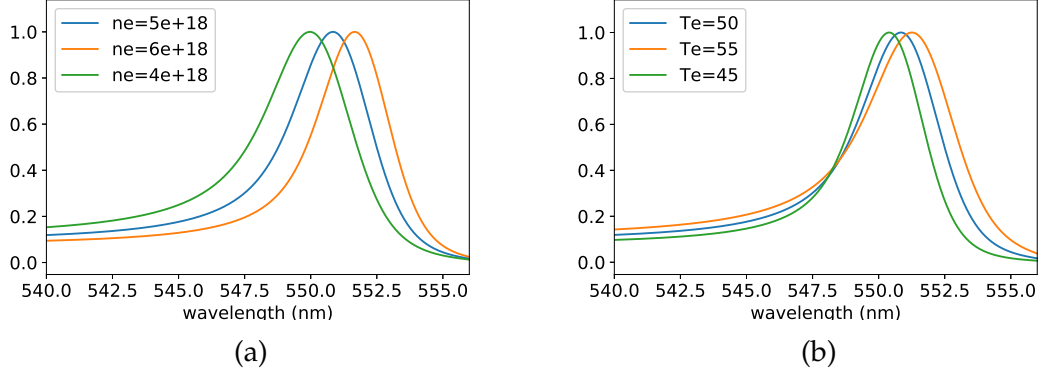


Figure 3.3: Plots showing how the profile changes based on changes in n_e or T_e . These profiles are normalized to 1 and show the longer wavelength peak when the laser wavelength is 526.5 nm. In (a) $T_e = 50$ eV and in (b) $n_e = 5 \times 10^{18} \text{ cm}^{-3}$.

3.2.2 Peak Shape

The other important EPW spectral feature is the shape, or the width, of the peaks, which is controlled by how strongly the EPW is damped. In the collisionless case this damping is Landau damping, which was found in the general form for the Salpeter approximation in Eq. 3.86. Plugging in the appropriate values we see that

$$\delta\omega_{epw} = \sqrt{\frac{\pi}{2}} \frac{\omega_{pe}}{k^3 \lambda_{De}^3} (1 + 3k^2 \lambda_{De}^2) e^{-\frac{1}{2k^2 \lambda_{De}^2} - \frac{3}{2}}. \quad (3.89)$$

From this we see that the peak width is largely dependent on the n_e/T_e term included in the λ_{De}^2 factor in the exponent. Since the peak separation is largely dependent on n_e , this means that we can use the peak shape to find T_e . As T_e increases the wave becomes more damped, and broader. Samples of how n_e and T_e affect the EPW peak profile are shown in Fig. 3.3.

Though in the ideal non-collisional case, the widths of the profiles can determine the electron temperature, other factors can also affect the widths of the peaks of the EPW. The first of these factors is a density gradient in the scattering

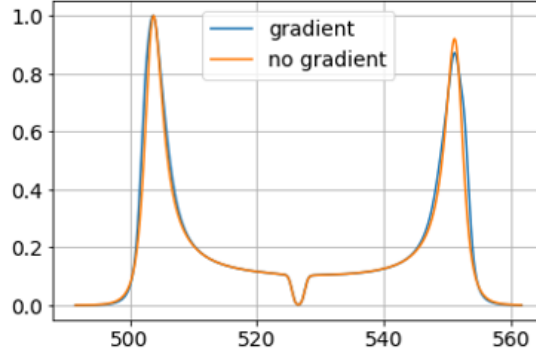


Figure 3.4: A plot showing two profiles of the EPW spectra based on including a gradient or not. The blue profile is generated from a $T_e = 50$ eV and a density profile with 50 % of the scattering volume at $n_e = 5 \times 10^{18} \text{ cm}^{-3}$ and 25% at $\pm 20\%$. The orange profile is a best fit to this profile, assuming no density gradients, and measures $T_e = 55$ eV and $n_e = 4.8 \times 10^{18} \text{ cm}^{-3}$. This shows that failing to account for gradients causes the measured T_e to be higher than the true value and n_e to be lower than the average value.

volume, which broadens the peaks due to the density dependence on the location of the peak. As shown in Fig. 3.4, failing to account for a gradient will cause the electron temperature to be lower than measured, and the average density to be higher.

Another major factor that can affect the widths of the EPW is collisions, as collisions tend to damp the wave even more [60]. The collisionality of the plasma depends on how k times the mean free path of the collision, λ_{ab} , compares to 1, with a high value being non-collisional. Since for the EPW we are interested in collisions involving electrons, and $\lambda_{ei} < \lambda_{ee}$, we will find λ_{ei} to see if we need to worry about collisions affecting the EPW. In general, $\lambda_{ab} = v_{Ta}/\nu_{ab}$, where ν_{ab} is the collision frequency. We define the momentum transfer collision frequency as [60]

$$\nu_{ab} = \frac{4\sqrt{2\pi}n_b(e_a e_b)^2 \Lambda}{3m_a^2 v_{Ta}^3} \quad \text{and} \quad \nu_{aa} = \frac{4\sqrt{\pi}n_a(e_a)^4 \Lambda}{3m_a^2 v_{Ta}^3}, \quad (3.90)$$

with Λ being the Coulomb logarithm. The Coulomb logarithm can be ap-

proximated by $\Lambda = 23.4 - 1.15 \log_{10} n_e + 3.45 \log_{10} T_e$ for $T_e < 50$ eV, and $\Lambda = 25.3 - 1.15 \log_{10} n_e + 2.3 \log_{10} T_e$ for $T_e > 50$ [6]. Using this then we see for our plasma ($Z = 6$, $n_e = 5 \times 10^{18} \text{ cm}^{-3}$ and $T_e = 20$ eV) $k\lambda_{ei} \approx 5$ which means that collisions may slightly affect the EPW profile, but they should not be significant.

3.3 Ion Acoustic Wave

The other resonance of the non-collisional theory without including a magnetic field is an effect of the electrons shielding the ions and occurs at the ion acoustic frequency. This is the low-frequency feature and primarily depends on the $S_i(\mathbf{k}, \omega)$ term in the form factor. Because this is a lower frequency mode, the shift relative to the laser frequency is small, and a higher spectral resolution is required to resolve it than the EPW feature. This enables also seeing a Doppler shift in the spectrum that corresponds to a fluid velocity in the plasma. In this regime the relative drift velocity between the electrons and the ions also affects the spectrum. Figure 3.5 shows a sample IAW spectral profile and how the major plasma parameters affect it.

3.3.1 Peak Shifts

The most straightforward feature to measure in the spectrum is the Doppler shift of the profile. If there is a net fluid velocity, v , within the plasma then there will be a shift of the center of the scattering profile relative to the laser wavelength based on $\Delta\omega_d = \mathbf{k} \cdot \mathbf{v}$. This shift is due to a Doppler shift of the scattered photons by plasma either moving relative to the laser, $\mathbf{k}_l \cdot \mathbf{v}$, or the

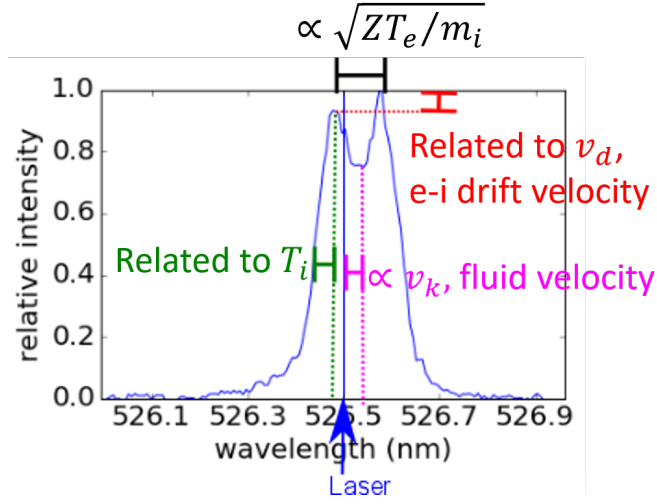


Figure 3.5: A diagram of a sample Thomson scattering IAW spectral profile.

collection optics, $\mathbf{k}_s \cdot \mathbf{v}$. Solving this in terms of a shifted wavelength gives

$$v_k = \frac{c \Delta \lambda_d}{\lambda_l \sqrt{2(1 - \cos \theta)}}, \quad (3.91)$$

where v_k is the velocity of the particle along \mathbf{k} and θ is again the scattering angle. For our laser wavelength and a scattering angle of 90° , a shift of 1 \AA corresponds to 40 km/s along \mathbf{k} . This, therefore, can give a measure of the directed flow velocity of the plasma, either when the direction of motion is known (e.g., radial) or through a comparison of shifts from two or more collection angles.

If the exact direction of motion is not known, then it is possible to use scattering from two different viewing angles to decouple the components of the velocity in the scattering plane [8]. For example, this can be used to differentiate between a radial flow velocity, v_r , and an azimuthal flow velocity, v_θ . We will start in xy -coordinates and then transform into polar coordinates as that is the easiest way to set up the most general problem of solving for the velocity for any location of the scattering volume. In this discussion we will call the scattering angle θ_s to differentiate it from the polar θ coordinate. We will assume \mathbf{k} to be in the xy -plane and assume that \mathbf{k}_l is along $\hat{\mathbf{y}}$. The $\hat{\mathbf{k}}$ direction in Cartesian

coordinates, therefore, is defined as

$$\hat{\mathbf{k}} = \cos(\theta_s/2)\text{sign}(\hat{\mathbf{x}} \cdot \hat{\mathbf{k}}_s)\hat{\mathbf{x}} - \sin(\theta_s/2)\hat{\mathbf{y}}. \quad (3.92)$$

Converting this into polar coordinates allows us to write $\hat{\mathbf{k}}$ as

$$\hat{\mathbf{k}} = k_r\hat{\mathbf{r}} + k_\theta\hat{\theta}, \quad (3.93)$$

$$k_r = \cos\left(\frac{\theta_s}{2}\right)\cos(\theta)\text{sign}(\hat{\mathbf{x}} \cdot \hat{\mathbf{k}}_s) - \sin\left(\frac{\theta_s}{2}\right)\sin(\theta), \quad (3.94)$$

$$k_\theta = -\cos\left(\frac{\theta_s}{2}\right)\sin(\theta)\text{sign}(\hat{\mathbf{x}} \cdot \hat{\mathbf{k}}_s) - \sin\left(\frac{\theta_s}{2}\right)\cos(\theta), \quad (3.95)$$

$$\theta = \arctan(y/x), \quad (3.96)$$

where y and x are the coordinates relative to the central axis of the plasma, the center of the jet for the research in this thesis. This allows writing the velocity of the plasma along the k direction as

$$v_k = v_r k_r + v_\theta k_\theta. \quad (3.97)$$

This can be used to decouple the velocity components of the plasma by collecting from any two scattering angles. Focusing on the case where we are collecting scattered light at opposing $\theta_s = 90^\circ$, and the laser passes through the axis of the plasma, reduces these equations to

$$v_k = \frac{v_r}{\sqrt{2}}\text{sign}(\hat{\mathbf{k}} \cdot \hat{\mathbf{r}}) + \frac{v_\theta}{\sqrt{2}}\text{sign}(\hat{\mathbf{k}} \cdot \hat{\theta}). \quad (3.98)$$

Therefore, it is possible to decouple the v_r and v_θ components of velocity as $\text{sign}(\hat{\mathbf{k}} \cdot \hat{\theta})$ will change between the scattering angles, but $\text{sign}(\hat{\mathbf{k}} \cdot \hat{\mathbf{r}})$ does not. Taking two scattering vectors \mathbf{k}_1 and \mathbf{k}_2 and if $\hat{\mathbf{k}}_1 \cdot \hat{\mathbf{r}} > 0$ and $\hat{\mathbf{k}}_1 \cdot \hat{\theta} > 0$ results in

$$v_{k1} = (v_r + v_\theta) / \sqrt{2}, \quad v_{k2} = (v_r - v_\theta) / \sqrt{2}. \quad (3.99)$$

Solving these give the following components of velocity

$$v_r = (v_{k1} + v_{k2}) / \sqrt{2}, \quad v_\theta = (v_{k1} - v_{k2}) / \sqrt{2}. \quad (3.100)$$

Similar techniques can also be used to measure v_r and v_z by collecting scattering along the z-axis [8]. We will note that unlike the v_θ and v_r , this can be done from a single viewing angle, assuming symmetry, as $\text{sign}(\hat{\mathbf{k}} \cdot \hat{\mathbf{r}})$ switches signs but $\text{sign}(\hat{\mathbf{k}} \cdot \hat{\mathbf{z}})$ does not.

3.3.2 Peak Separation

A prominent feature of the IAW scattering feature is the separation between the two peaks. This can be approximated in a similar manner to the peak locations for the EPW feature. However, now we are using the $S_i(\mathbf{k}, \omega)$ term, so we are using β instead of α in Eq. 3.80, which gives

$$\omega_{iaw}^2 = k^2 \left(\frac{ZT_e}{m_i(1 + k^2\lambda_{De}^2)} + \frac{3T_i}{m_i} \right). \quad (3.101)$$

Since this is the low-frequency mode, we can say that $|\mathbf{k}_l| \approx |\mathbf{k}_s|$, and therefore, can use the following approximation for k

$$k \approx 2k_l \sin\left(\frac{\theta}{2}\right). \quad (3.102)$$

Using this and the location of the peaks, we can find an estimate of the separation between the ion-acoustic peaks as

$$\Delta\lambda_{iaw} \approx \frac{4}{c} \lambda_l \sin(\theta/2) \sqrt{\frac{T_e}{m_i} \left[\frac{Z}{1 + k^2\lambda_{De}^2} + \frac{3T_i}{T_e} \right]}. \quad (3.103)$$

We see that in this case if $ZT_e \gg 3T_i$, and $k^2\lambda_{De}^2 \ll 1$ then ZT_e is the dominant factor in peak separation. Therefore, if we know or have some estimate of Z we can have a good estimate of T_e by simply measuring the separation of the two peaks. The first assumption is valid in our plasmas for high Z if $T_e \approx T_i$. The second assumption is related to how collective the plasma is since $k^2\lambda_{De}^2 = 1/\alpha^2$.

Therefore, if we are in the highly collective regime, we do not have to worry about n_e affecting the peak separation.

We can make some approximations in Eq. 3.103 to estimate the minimum possible density of the plasma based on the peak separation, as well as regions where density should not affect the peak separation. For these assumptions we rewrite $k^2 \lambda_{De}^2 = aT_e/n_e$, where $a = (1486k_l \sin(\theta/2))^2$, and assume that $ZT_e \gg 3T_i$. This allows us to rewrite Eq. 3.103 as

$$\Delta\lambda_{iaw} \approx \frac{4}{c} \lambda_l \sin(\theta/2) \sqrt{\frac{T_e}{m_i} \left[\frac{Z}{1 + aT_e/n_e} \right]}. \quad (3.104)$$

To find the minimum density for a given peak separation, we rewrite the equation one more time

$$\Delta\lambda_{iaw} \approx \frac{4}{c} \lambda_l \sin(\theta/2) \sqrt{\frac{Zn_e}{m_i}} \sqrt{\frac{T_e}{n_e + aT_e}}. \quad (3.105)$$

In this equation, as T_e approaches infinity the peak separation will increase to an asymptomatic limit. Taking this limit gives

$$\Delta\lambda_{iawmax} \approx \frac{4}{c} \lambda_l \sin(\theta/2) \sqrt{\frac{Zn_e}{m_i}} \sqrt{\frac{1}{a}} \approx 0.387 \sqrt{\frac{Zn_e[10^{18}cm^{-3}]}{A}}. \quad (3.106)$$

Where the last equation is for our laser wavelength and scattering at 90° , and A is the atomic number of the atom. For Al jets, with $A = 27$, $Z = 6$, and a separation of 0.15 nm, the minimum value for n_e is $8 \times 10^{17} cm^{-3}$. This means that for any lower density it would be impossible for the profile to reach a peak separation of 0.15 nm.

To see how high the density needs to be to stop affecting the peak separation, one can look at the denominator of Eq. 3.104, $1 + aT_e/n_e$, and assume $aT_e/n_e \ll 1$, for example $aT_e/n_e \leq 0.1$. For our scattering at 90° this results in

$$T_e[\text{eV}] < 6.3n_e[10^{18}cm^{-3}], \quad (3.107)$$

which means that if the density is $5 \times 10^{18} \text{ cm}^{-3}$, it will not significantly affect the peak separation unless T_e is 30 eV or higher.

An interesting feature of this slight density dependence on the peak separation, is that in the right parameter region it can be used as a method to measure the density of the plasma [24]. Through the collection from significantly different values of k , an experiment can be designed where one k-vector, k_1 , will have significantly more density dependence than the other k-vector, k_2 . This second k-vector can be used to find T_e as there is little dependence in that profile on the density, and then use that temperature to find n_e from the k_1 scattering profile. These two different values of k can be created by either collecting from 2 different angles, or by using two different laser wavelengths. For this idea to work, the difference in peak separation due to density between the two angles through the factor $1 + k^2 \lambda_{De}^2$ must be significant.

3.3.3 Peak Widths

A third feature of the ion acoustic wave feature of the Thomson scattering profile that can be used as a diagnostic is the peak shape or peak width. This feature can be more complicated than the previously mentioned features. However, if certain plasma conditions can be isolated, it can still prove to be useful. In basic collisionless Thomson scattering theory, as for the EPW features, the IAW peak width depends on how strongly Landau damped the waves are. Using Eq. 3.86, which is valid when $ZT_e/T_i \approx 1$, causing the ion Landau damping to dominate over the electron Landau damping, the widths of the ion-acoustic peaks can be

estimated as

$$\delta\omega_{iaw} = \sqrt{\frac{\pi}{2}} k v_{Ti} \left[\frac{ZT_e}{T_i(1 + k^2 \lambda_{De}^2)} \right]^2 \left[1 + \frac{3T_i(1 + k^2 \lambda_{De}^2)}{ZT_e} \right] e^{-\frac{ZT_e}{2T_i(1 + k^2 \lambda_{De}^2)} - \frac{3}{2}}. \quad (3.108)$$

As before, the Landau damping is dependent primarily on the exponential factor. Thus, the IAW peak width is related to ZT_e/T_i . Since we already know ZT_e from the peak separation, the peak widths could be used to find T_i . Therefore, if basic Thomson scattering is valid, the widths of the peaks can be used to measure the ion temperature.

However, going beyond basic collisionless Thomson scattering theory, other factors can significantly affect the shape of the peaks. These factors include collisions [60, 71], velocity gradients, and turbulence [22, 26]. The factor that is easiest to see affecting the spectral profile is a velocity gradient in the scattering volume, which is illustrated in Fig. 3.6. In this figure we have accounted for a flow velocity gradient by assuming that we could model the flow velocity as a Gaussian profile, and then broke that profile into 10 different regions. We then determined the Thomson scattering spectrum for each of the 10 regions (the smaller peaks on the left figure) and added them up to get the resulting Thomson scattering profile in blue. We see here that failing to account for this spread in fluid velocity with a Gaussian profile and a FWHM of 10 km/s, will cause the measured value of T_i to increase from 40 eV to 60 eV. This velocity gradient could be reasonable in the jet region of the plasma, as plasma outside the jet is converging onto the jet with a velocity of around 20 km/s. Though this primarily affects the inferred ion temperature, we see that T_e also drops some due to the increase in T_i .

We have already discussed how collisions affect the EPW feature, and a similar discussion is relevant here. However, we are now interested in collisions that

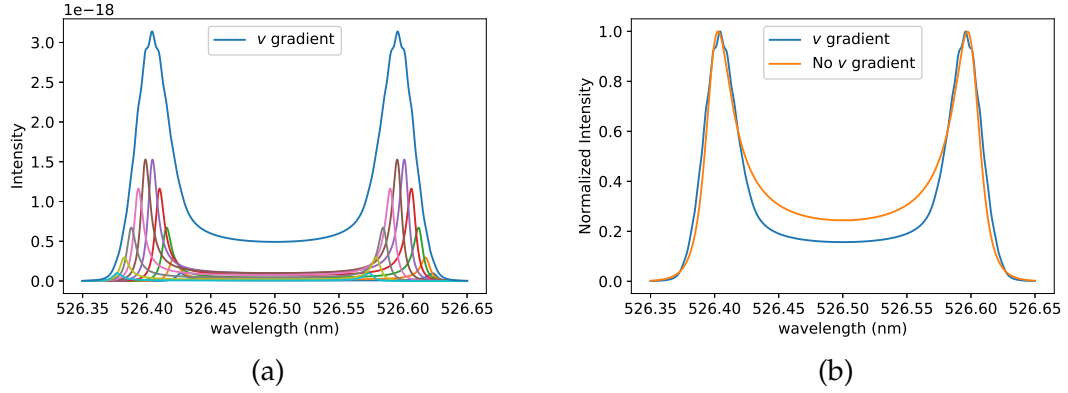


Figure 3.6: Plots showing the effect of a flow velocity gradient in the scattering volume. (a) shows a plot of the 10 individual Thomson scattering profiles if the flow velocity had a FWHM of 10 km/s, and the resulting profile. The temperatures used for this profile were $T_e = T_i = 40$ eV. (b) shows the composite profile from the left image as well as an attempt to fit it without accounting for gradients. In this case $T_i = 60$ eV, and $T_e = 31$ eV.

involve ions. Since λ_{ii} tends to be smaller than λ_{ei} for high energy density plasmas, we will focus on λ_{ii} . Our typical set of plasma parameters ($T_e = T_i = 20$ eV, $n_e = 5 \times 10^{18}$ cm $^{-3}$, and $Z = 6$) gives a value for $k\lambda_{ii}$ of 0.2. This suggests that collisions will affect the widths of the ion-acoustic peaks.

While each of these factors can significantly contribute to the width of the peaks of the ion acoustic wave, increasing the ion temperature inferred from the width, they are challenging to model accurately. The first order way to account for the three additional broadening mechanisms is to convolve the profile with an additional Gaussian profile [22]. As we see in Fig. 3.7 this approach can significantly improve the fit to the scattered profile, mainly the central dip.

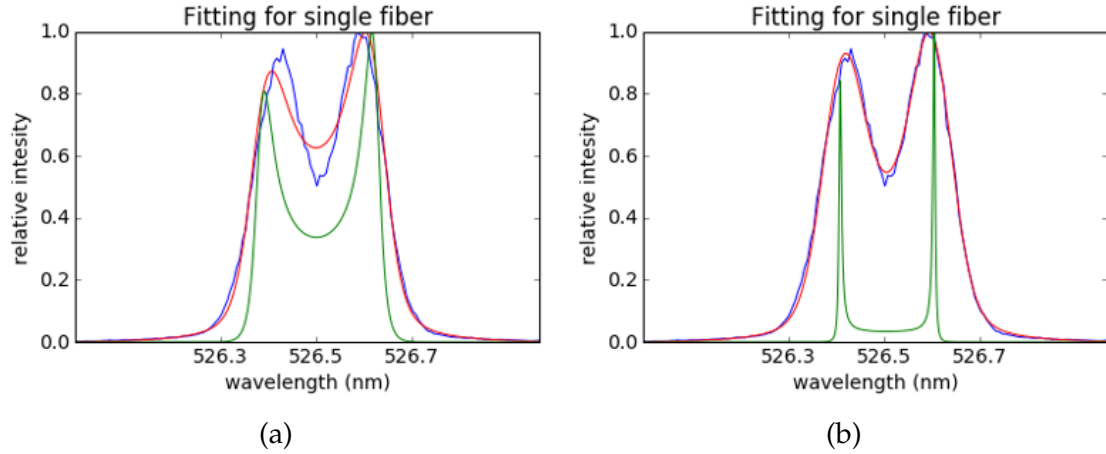


Figure 3.7: A comparison of a fit without (a) and with (b) an additional Gaussian profile. Blue is the raw data, green is the best fit result without any convolution, and red is the best fit, a result of convolving the green profile with the instrumental function on the left, and both an instrumental and additional Gaussian on the right.

3.3.4 Peak Intensities

The IAW spectral feature to be discussed here is that the two peaks can have different intensities. Most often this difference is attributed to a difference in flow velocity between the electron and the ion fluids, which we will call the relative electron-ion drift velocity, u_d . Accounting for this relative drift velocity affects the calculation of $S(\mathbf{k}, \omega)$ by replacing all the x_e terms with $x_e - x_d$. Here x_d is the relative drift velocity scaled to the electron thermal velocity, $x_d = u_d/a \cos \chi$, where χ is the angle between \mathbf{u}_d and \mathbf{k} . The ions are not affected by x_d as the ion velocity has already been accounted for in both the x_i and x_e terms. The primary effect of the relative drift velocity is to cause electron damping to be shifted relative to the ion damping, see Fig. 3.8. This shift causes the two IAWs to be subject to different damping. The less damped wave will produce stronger scattering. Since this effect is a result of a shift in the electron damping of the wave relative to the ion damping of the wave, it is sensitive to both T_e and T_i . Since T_i

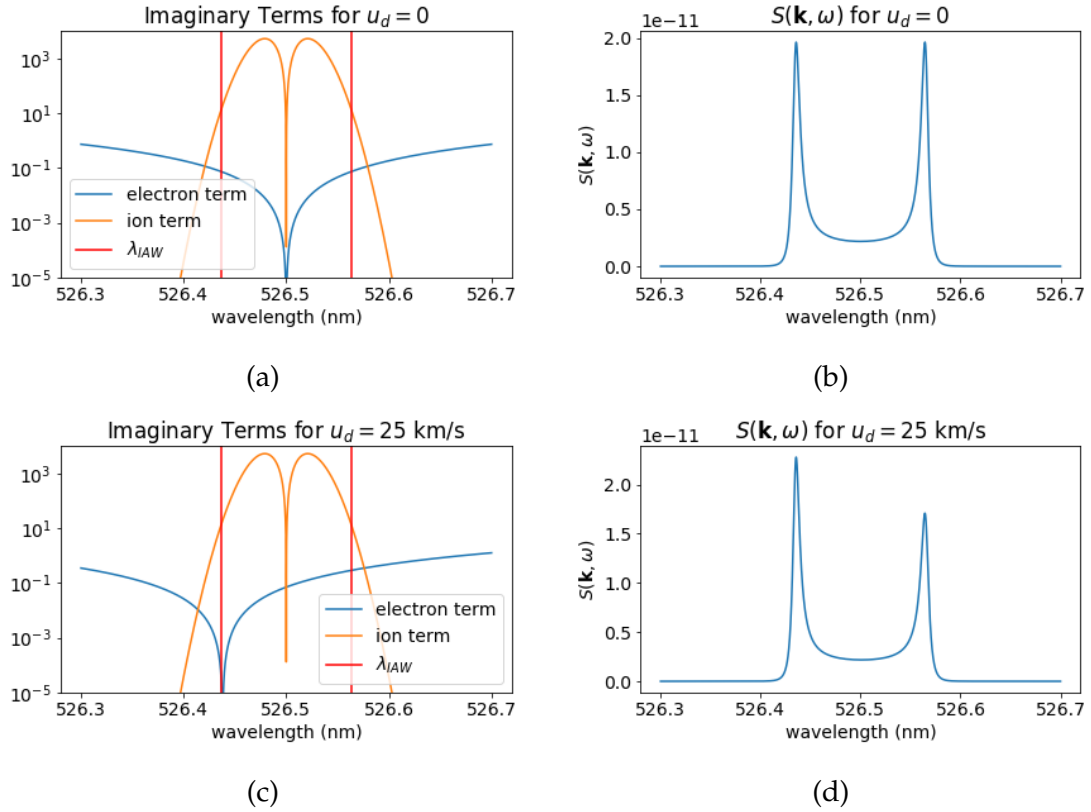


Figure 3.8: Shows the effect of having a relative drift velocity between the electrons and the ions. For parts (a) and (c) the $\alpha^2 W_{im}(x_e)$ and $\alpha^2 \frac{ZT_e}{T_i} W_{im}(x_i)$ are plotted for the electrons and the ions, respectively. For $u_d = 0$ ((a) and (b)) the imaginary electron term is symmetric about the laser wavelength and so the peaks are the same height. When $u_d = 25$ km/s, though, ((c) and (d)) the imaginary electron term has been shifted, causing the higher energy peak to become less damped, and, therefore, the stronger of the two peaks.

from Thomson scattering can be unreliable, u_d measurements are unreliable if it is determined using only Thomson scattering-based plasma parameters.

The peak intensities can also be affected by the use of the finite sized optics needed to collect and focus the light, which means we are really scattering with a range of \mathbf{k} vectors. This can affect the ratio of peak intensities when the plasma is moving at a detectable velocity because the peak separation and the peak shift both scale with k [21]. This means that as you increase \mathbf{k} you will get more Doppler shift from fluid motion, but the peaks will be farther apart,

while the inverse will be true for smaller values of \mathbf{k} . This means that the wavelength of the IAW peak closer to the laser wavelength will be about the same for all observed values of \mathbf{k} , while the peak that is further away from the laser wavelength will have its wavelength shifted based on the values in the range of \mathbf{k} vectors. This will increase the intensity of the peak closer to the laser wavelength, compared to the other peak, which is broadened. Due to the relatively low velocities in the plasma jets and the fact that we use high f/number lenses, this should not be a concern in this thesis. However, future experiments may need to address this if they focus or collect with a smaller f/number lens or observe plasmas with faster fluid velocities.

3.4 Analysis Techniques

Now that we have a good intuition of how Thomson scattering behaves under various conditions, we proceed to detail the numerical calculation of the form factor that was used to generate theoretical Thomson scattering profiles. More details on these calculations can be found in Appendix D of D. Froula *et al.* 2011 and the code used to generate these profiles can be found in Appendix A [25]. As a reminder we are trying to solve the full equation for the form factor, $S(\mathbf{k}, \omega)$, i.e., Eq. 3.70. Since we are solving for the waves within the plasma where the scattering occurs, we must use the dispersion relation for an EM wave within the plasma. Since we are focused in this work on non-relativistic plasmas, we can use the traditional dispersion relation for EM waves in a plasma

$$\omega_{\sigma}^2 = c^2 k_{\sigma}^2 + \omega_{pe}^2, \quad (3.109)$$

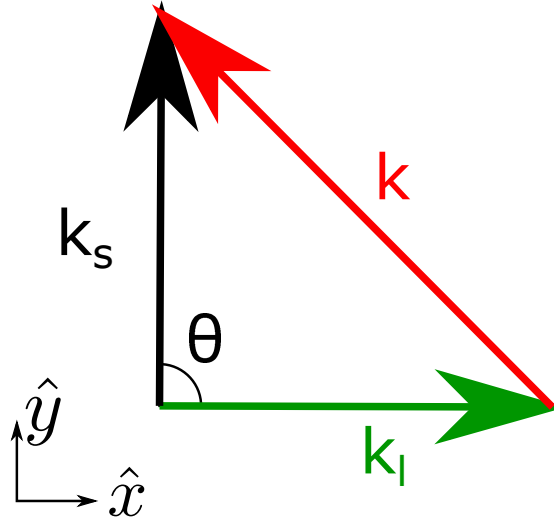


Figure 3.9: Shows a representation of the three different k vectors.

which can be then used to find \mathbf{k}_s and \mathbf{k}_l . These wave vectors can then be used to find k , see Fig. 3.9, by

$$k = \sqrt{k_s^2 + k_l^2 - 2k_s k_l \cos \theta}. \quad (3.110)$$

The difficulty in numerically evaluating the form factor is that the W function, which is related to the plasma dispersion function, Z , is non-analytic, and is needed to solve the electron and ion susceptibilities, Eq. 3.67-3.68. The key advantage, however, is that $W(x)$ is only a function of one variable, meaning that it is possible to make a table of the solutions to $W(x)$ as a function of x and then interpolate from that table for a given problem. As a reminder, the equation we need to solve numerically is

$$W(x) = -1/2 \frac{d}{dx} Z(x), \quad (3.111)$$

where

$$Z(x) = \frac{1}{\sqrt{\pi}} \int_{-\infty}^{\infty} \frac{e^{-z^2}}{z-x} dz, \quad (3.112)$$

which is the plasma dispersion function. This problem cannot be solved analytically due to the pole at $z = x$, and not being able to close the integral in the

complex plane. To approach this problem, we need to break the integral into three parts

$$Z(x) = \frac{1}{\sqrt{\pi}} \left[\int_{-\infty}^{x-\varphi} \frac{e^{-z^2}}{z-x} dz + \int_{x+\varphi}^{\infty} \frac{e^{-z^2}}{z-x} dz + \int_{x-\varphi}^{x+\varphi} \frac{e^{-z^2}}{z-x} dz \right], \quad (3.113)$$

where φ is the distance away from the pole, and should be much smaller than x . The last term in this integral represents the integral around and near the pole. Since the integral goes to zero relatively quickly as z diverges from the pole, we can solve each of the first two integrals numerically. To do this we will define two arrays of steps of z values,

$$z_{-,m} = x - \varphi - (m - 1)\Delta \quad \text{and} \quad z_{+,p} = x + \varphi + (p - 1)\Delta. \quad (3.114)$$

In this equation Δ is the step size for the integration and p or m are integers; ideally Δ is very small and both p and m go from 1 to infinity. However, since the integral goes to 0 relatively quickly, we do not need to take p and m all the way to infinity, and will define M and P as the maximum number of steps. We write the first two parts of the integral as

$$\int_{-\infty}^{x-\varphi} \frac{e^{-z^2}}{z-x} dz + \int_{x+\varphi}^{\infty} \frac{e^{-z^2}}{z-x} dz = \sum_{m=1}^M \frac{\Delta e^{-z_{-,m}^2}}{z_{+,m} - x} + \sum_{p=1}^P \frac{\Delta e^{-z_{+,p}^2}}{z_{+,p} - x}. \quad (3.115)$$

The third part of the integral can be evaluated using the traditional integral around a pole and a Taylor expansion to correct for the small portion of the integral between φ and the pole,

$$\int_{x-\varphi}^{x+\varphi} \frac{e^{-z^2}}{z-x} dz = i\pi e^{-x^2} - 4xe^{-x^2}\varphi. \quad (3.116)$$

Rewriting this slightly, removing the x terms in the denominator, to make the derivative easier gives

$$Z(x) = \frac{1}{\sqrt{\pi}} \left[\sum_{m=1}^M \frac{\Delta e^{-z_{-,m}^2}}{-(\varphi + (m - 1)\Delta)} + \sum_{p=1}^P \frac{\Delta e^{-z_{+,p}^2}}{\varphi + (p - 1)\Delta} + i\pi e^{-x^2} - 4xe^{-x^2}\varphi \right]. \quad (3.117)$$

Now the derivative of this can be taken and used to get a final numerical solution for W ,

$$W(x) = \frac{1}{\sqrt{\pi}} \left[\sum_{m=1}^M \frac{-\Delta z_{-,m} e^{-z_{-,m}^2}}{\varphi + (m-1)\Delta} + \sum_{p=1}^P \frac{\Delta z_{+,p} e^{-z_{+,p}^2}}{\varphi + (p-1)\Delta} + e^{-x^2} (i\pi x + 2\varphi - 4x^2\varphi) \right]. \quad (3.118)$$

This numerical solution to find W can be run a single time to generate a table of solutions to W for different values of x . This table can then be referenced any time one wants to generate a theoretical Thomson Scattering profile. Code for generating this table, interpolating from this table, and generating a theoretical Thomson scattering profile can be found in Appendix A.

3.5 Spectral Fitting Techniques

We have spent a lot of time discussing the theory of the Thomson scattering spectrum, as well as approximations that help to gain intuition on how the different parameters affect the resulting spectrum. In doing this we have seen that the full Thomson scattering profile depends on many different plasma parameters (at least T_e , T_i , Z , n_e , v_k and u_d). However, all these parameters are interrelated, and we do not have the capability to determine all of them as there are only 4 primary degrees of freedom for the IAW and 2 for the EPW. We will now discuss the assumptions and techniques used to fit the scattering spectra from plasma jets to determine several plasma parameters simultaneously. When performing these fits we are using the full solution to the form factor, Eq. 3.70, and not the Salpeter approximation already discussed, but that does help in understanding how different plasma parameters affect the Thomson scattering spectral profile. We will also discuss sources of errors and estimation of error bars.

3.5.1 Ion Acoustic Wave Fitting

As already discussed, there are 4 primary degrees of freedom (spectral shift, peak separation, peak shape, and relative peak intensities) for the IAW spectral feature, enabling its use to determine 4 fitting parameters. The spectral shift is related only to the flow velocity, v_k , so that is easy. The peak separation, however, is determined by several parameters, T_e , T_i , n_e , and Z . However, the largest dependence (see Eq. 3.103) is on the ZT_e term. Since Z can be estimated using tables such as the FLYCHK table [13], we can use T_e as the primary fitting parameter affecting this feature. The FLYCHK table is an nLTE (non-local thermal equilibrium) model of Z as a function of n_e and T_e . The density dependence is handled by using the density measured from either interferometry or from the EPW spectral feature, which normally puts it between 5×10^{18} and $1 \times 10^{19} \text{ cm}^{-3}$, and the T_i dependence will be handled by the peak shape fitting term. The relative peak intensities can be fit using the relative electron-ion drift velocity. However, we note again that this term is sensitive to both T_e and T_i and, therefore, is included more to allow the two peaks to have different intensities rather than to model something actually physical. The final degree of freedom is the peak shape, which is accounted for in one of two ways. The first way is to have T_i be a fitting parameter, since the other terms in the basic collisionless theory of broadening are already accounted for. The other method assumes that $T_i = T_e$ and accounts for any additional broadening by convolving the resulting profile with a Gaussian profile, as discussed earlier, as that seemed to significantly improve the fit to the peak shape. This additional broadening can be justified by the fact that we are in the collisional regime. From simulations, and since the ion-electron transfer energy collision time [67] is around 2 ns (for $T_e = T_i = 20 \text{ eV}$, $Z = 6$, and $n_e = 5 \times 10^{18} \text{ cm}^{-3}$), we do not expect the ions to be significantly colder

than the electrons, so this is a good minimum value for T_i .

Before discussing error bars, it is important to discuss the effects of two deviations on the IAW spectral feature from basic non-collisional Thomson scattering theory, focusing primarily on how they affect the measurement of the electron temperature. The first is the effects of collisions on the spectrum. Though several models have been developed to take the Thomson scattering spectrum from the collisional to the non-collisional regime [60, 50, 7, 71], many tend to be very complicated and to computationally expensive to include as a universal fitting technique for all of our data. In the intermediate collisional regime, $k\lambda_{ii} \approx 1$, the general trend is for the peaks to broaden as well as move closer together. The peak broadening should not influence the measured electron temperature as we already accounted for this when we assumed that $T_i = T_e$. The peaks moving closer together, however, would cause an underestimation of the electron temperature. To see the effect of collisions on the peak separation, look back at Eq. 3.101 with the 3 being replaced with a Γ_i factor

$$\omega_{iaw}^2 = k^2 \left(\frac{ZT_e}{m_i(1 + k^2\lambda_{De}^2)} + \frac{\Gamma_i T_i}{m_i} \right). \quad (3.119)$$

This Γ_i term is determined by collisions, where $\Gamma_i = 3$ for the collisionless case and it decreases to 5/3 when the plasma is strongly collisional. Using the assumption now that $\alpha^2 \gg 1$, meaning that $k^2\lambda_{De}^2 \ll 1$, and that $T_e = T_i$ we can see that the peak separation scales by

$$\omega_{iaw} \propto \sqrt{(Z + \Gamma_i)T_e}. \quad (3.120)$$

If we assume that $Z = 5$, then T_e can vary by 20% from collisionless to the strongly collisional regime in order to keep the peak separation constant. A first order way to correct for errors in this term, assuming all that we care about is the electron temperature, is to still allow peak broadening to be accounted for

with an additional Gaussian, but allow T_i to be lower than T_e , which has the effect of decreasing the Γ_i factor in this approximation.

The other possible deviation from non-collisional Thomson scattering is the effect of a non-Gaussian profile of the electrons. The primary departure we are interested in is the fact that a laser will preferentially heat slower electrons, which will cause the electron distribution function to form a super-Gaussian profile [70, 47, 43]. We define this velocity super-Gaussian distribution as [70]

$$f_{e0}(\mathbf{v}) = \frac{m}{4\pi v_{mT_e}^3 \Gamma(3/m)} \exp\left[-\left(\frac{v}{v_{mT_e}}\right)^m\right], \quad (3.121)$$

where m is between 2 and 5, and

$$v_{mT_e}^2 = \frac{3\Gamma(3/m)}{\Gamma(5/m)} v_{T_e}^2, \quad (3.122)$$

where $\Gamma(x)$ is the gamma function [68], and $v_{T_e} = \sqrt{T_e/m_e}$ is still the electron thermal velocity. Here T_e is defined as [70]

$$T_e = \frac{1}{3} \int_{-\infty}^{\infty} m_e v^2 f_{e0} dv. \quad (3.123)$$

Simulations have shown that m can be reasonably estimated, as a function of laser energy and electron temperature, by the following equations [47]

$$m = 2 + \frac{3}{1 + 1.66/\alpha_l^{0.724}}, \quad \text{and} \quad \alpha_l = 3.74 \times 10^{-16} \frac{I_0 \lambda_0^2 A}{T_e}, \quad (3.124)$$

with I_0 being the laser power density (W/cm^2), λ_0 is the wavelength of the laser (μm), T_e is the electron temperature (keV), and A is the atomic number of the plasma ions. Using $I_0 = 5 \times 10^{12} \text{ W}/\text{cm}^2$, and $T_e = 15 \text{ eV}$ results in $m = 2.29$, meaning that a super-Gaussian profile will be induced by the laser.

Though a super-Gaussian electron distribution function is computationally reasonable and will be discussed in Appendix B, here we will limit discussion

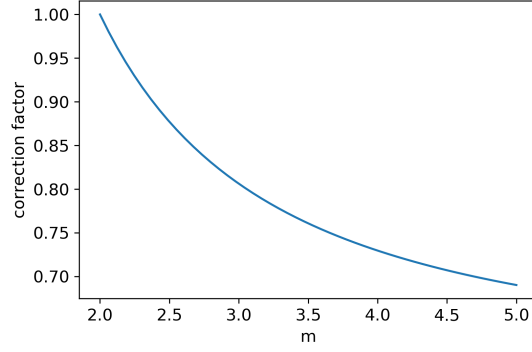


Figure 3.10: A plot showing the effect of changing m on the $\frac{\Gamma(1/m)\Gamma(5/m)}{3\Gamma^2(3/m)}$ term in the peak separation. We see by increasing m this term decreases, meaning that the peaks are further apart for a given temperature.

to the general effect of a super Gaussian profile. In this case, the IAW frequency can be found from [70]

$$\omega_{iaw}^2 = k^2 \left(\frac{ZT_e}{\frac{\Gamma(1/m)\Gamma(5/m)}{3\Gamma^2(3/m)} + k^2 \lambda_{De}^2} + 3T_i \right). \quad (3.125)$$

We see that the primary effect on the location of the peaks is the factor $\Gamma(1/m)\Gamma(5/m)/3\Gamma^2(3/m)$, which is plotted in Fig. 3.10. We see that as m is increased this factor decreases, meaning that the peaks are further apart for a given temperature. This means that failing to account for super-Gaussian effects will in general overestimate the electron temperature of the plasma.

3.5.2 Electron Plasma Wave Fitting

As discussed previously, there are two primary features that can be seen in the spectrum of the EPW, the peak separation and the peak width. These have been shown to be dependent only on n_e and T_e , and so those are clearly two parameters we want to use for our fitting. If we can fit each peak individually and they are far enough away from the IAW scattering feature, that it has no effect on the EPW spectrum, then this would be all that is needed to fit the

spectrum. However, sometimes our peaks are so close to the laser line that the wings of the IAW are important. This can be accounted for by changing the T_i in the generation of the scattering profile. Changes to T_i have no effect on the EPW feature as the plasma frequency is too high for the ions to respond. However, as discussed, T_i does affect the IAW feature. Froula *et al.* [25] shows that the intensity of the IAW increases with increasing T_i , and, therefore, we can use T_i to account for the wings from the IAW in the EPW fitting routine. In addition, there could possibly be useful information in the relative intensities of the two EPW spectral peaks, which is accounted for by adding a scaling factor that enables the two EPW peaks to have different intensities from non-collisional Thomson scattering theory. A possible reason for this difference is instrumental errors. Improving the relative calibration across the spectrum could help correct for this error. Another possibility is heat flux within the plasma, which will cause a slight modification to the electron distribution function that would change the relative number of electrons in resonances with the two EPW. This modification will cause the intensity of the two peaks to be different from non-collisional Thomson scattering with a Maxwellian distribution function [35, 36].

3.5.3 Error Bars

In order to determine the error bars, the primary method used was a Monte Carlo (MC) technique as many of the fitting parameters are closely coupled through complex formulae, making standard error propagation challenging [22, 1]. After finding a best fit profile to the raw data with any of the fitting models discussed in the previous two subsections (Sec. 3.5.1 and 3.5.2), 100 synthetic spectra were generated by adding random noise to the best fit pro-

Table 3.1: Table of the FWHM for the parameters that were varied for each synthetic spectrum for the MC error bar calculations. Each of the columns represents a different fitting model. All these fitting models assumed that the plasma was non-collisional and Maxwellian. The N/A parts of the table do not apply to that fitting model as the parameters in that row are used in the model to find the best fit for each synthetic spectrum.

fitting model	IAW feature		EPW feature
	ν, T_e, T_i, u_d	$\nu, T_e, \text{width}, u_d$	$n_e, T_e, T_i, \text{relative intensity}$
n_e	50%	50%	N/A
\bar{Z}	10%	10%	10%
T_e/T_i	N/A	50%	N/A
λ_l	0.2	0.2	0.2
instrumental width	20%	20%	20%
linear dispersion	1.5%	1.5%	1.5%

file based on the variance between the best fit and the raw data. Each of these synthetic spectra was then fit with the same model as the raw data, but several non-fitting parameters were varied by choosing a random point within a Gaussian distribution. Table 3.1 list these parameters and the standard deviation of their Gaussian distribution based on the fitting model used. For each of the fitting parameters for the chosen fitting model, the results are reported as the median of these 100 fits, with an error bar equal to the standard deviation of the 100 fits.

While the MC calculations above are a good way to get error bars, issues arise when trying to compare the effect of various fitting methods or physical effects that could contribute to the error that are non-Gaussian, as doing Gaussian based MC calculations are then no longer appropriate. The key examples of this are collisions and super Gaussian electron profiles, where we are initially assuming one end of the extreme (non-collisional and Maxwellian electron distribution function) and, therefore, only have errors in one direction. Since we are especially interested in the measured value of T_e , we can study how chan-

ging various parameters will affect the measured T_e and then group together factors that only increase T_e , giving a maximum value, and factors that only decrease T_e to obtain a minimum value.

Key to much of this discussion is the peak separation from the Salpeter approximation, Eq. 3.119. We will use the fitting model which assumed that $T_e = T_i$ and added some extra Gaussian width. It is easy to see from Eq. 3.119 that increasing either Z or T_i will force T_e to decrease in order to keep the same location of the peaks. In addition, increasing n_e will reduce the denominator of the first term, meaning that T_e must decrease. As noted in the super Gaussian discussion, above, increasing m (the power of the exponential term) will increase the peak separation for a given T_e , meaning that increasing m causes T_e to decrease. Additionally, accounting for the effects of collisions lowers the Γ_i term, and therefore, causes the required T_e to be higher.

In addition to these possible errors in the assumptions about the plasma, we also need to account for possible errors in the instrument's calibration, which include the dispersion function (in nm/mm) and the instrumental width. If the dispersion function is increased then the Thomson scattering peaks are farther apart than the initial measurement, meaning that T_e is increased. By decreasing the instrumental width, we increase the width that is needed from the Thomson scattering profile, which causes T_i to increase and therefore decreases T_e .

Using the above facts about the effect of different parameter changes on T_e , together with assumptions about the amount of error we could have for each parameter, we can put together modifications to these parameters to find the minimum and maximum values for T_e . These modifications are summarized in Table 3.2. Some of them need additional discussion. For Z , we base the errors

Table 3.2: Table of the values used for parameters to try to find a possible range for T_e .

Min T_e	Max T_e
$Z = 1.2Z$	$Z = 0.8Z$
$n_e = 1.5n_e$	$n_e = 0.5n_e$
T_i fitting parameter	$T_i = 1 \text{ eV}$
$m = 2.5$	$m = 2$
additional width = 0.001 \AA	additional width is fitting parameter
0.8 * instrumental width	1.2 * instrumental width
0.98 * instrumental dispersion	1.02 * instrumental dispersion

on the temperature from the initial best fit, and not the extreme value found for T_e . This was done because if we are trying to find the minimum for T_e , the value found for Z if the new, lower value of T_e is used to find Z , effectively cancels out the effect of increasing Z in the first place. By allowing for very little extra Gaussian width (0.001 \AA) in the minimum T_e case, we are effectively allowing the entire profile width to be accounted for by T_i , which, therefore, finds not only a minimum to T_e but also a maximum to T_i . In the case of finding the maximum of T_e we set T_i to be small (only 1 eV) to try to account for not only errors in T_i but also the effective decrease in the T_i contributions to the peak separation because of ion-ion collisions.

CHAPTER 4

PLASMA JET SIMULATION OVERVIEW

While most of this work was experimental, it is important to use simulations alongside the experiment. Simulations can help design experiments by giving ideas on regions in the plasma to explore, while the experimental results can help develop the simulation code by providing data to help validate it. The simulation code used was PERSEUS (Plasma as an Extended-MHD Relaxation System using an Efficient Upwind Scheme), which is an extended magnetohydrodynamics (XMHD) code developed by Charlie Seyler and Matt Martin [63, 46]. While some initial simulations were run by the author, many of the improvements to the code discussed in this thesis were tested and developed by Charlie Seyler.

4.1 Plasma Model

The basis for XMHD simulations is a set of velocity moment equations of the Vlasov equation

$$\frac{\partial f_\sigma}{\partial t} + \mathbf{v} \cdot \frac{\partial f_\sigma}{\partial \mathbf{r}} + \mathbf{a} \cdot \frac{\partial f_\sigma}{\partial \mathbf{v}} = \sum_{\sigma'} C_{\sigma\sigma'}(f_\sigma), \quad (4.1)$$

where f_σ is the velocity distribution function, the acceleration term is the Lorentz force, $\mathbf{a} = \frac{q_s}{m_s} (\mathbf{E} + \mathbf{v} \times \mathbf{b})$, and $\sum_{\sigma'} C_{\sigma\sigma'}(f_\sigma)$ is a term to model collisional effects in the plasma. We note that while the previous chapter was in CGS units to be consistent with previous literature, this chapter is in SI units since the publications on PERSEUS are in SI [63, 46]. We now define the density and the mean velocity of a single species, σ , as the zeroth and first moments of the dis-

tribution function

$$n_\sigma = \int f_\sigma(\mathbf{x}, \mathbf{v}, t) d\mathbf{v}, \quad (4.2)$$

$$\mathbf{u}_\sigma = \frac{\int \mathbf{v} f_\sigma(\mathbf{x}, \mathbf{v}, t) d\mathbf{v}}{n_\sigma}. \quad (4.3)$$

With any moment approach, it is possible to continue to take higher and higher moments of the Vlasov equation, each with a higher order effect on the resulting distribution function. A kinetic solution is reached when an infinite number of moments are taken. The main goal of an MHD or XMHD model is to be able to solve a system of equations that is simpler than the full kinetic solution, but includes enough moments, so that the solution to the problem of interest reasonably approaches the full kinetic solution. Therefore, the system of equations must be closed at some point. For most of the simulations performed in this work, the system was closed after the second moment by assuming that heat flow could be ignored and that the pressure was isotropic, $P_\sigma = n_\sigma k_B T_\sigma$. The zeroth (continuity equation), first (conservation of momentum), and second (conservation of energy) order moments for a single species, therefore, are

$$\frac{\partial n_\sigma}{\partial t} + \nabla \cdot (n_\sigma \mathbf{u}_\sigma) = 0, \quad (4.4)$$

$$\frac{\partial (m_\sigma n_\sigma \mathbf{u}_\sigma)}{\partial t} + \nabla \cdot \left(m_\sigma n_\sigma \mathbf{u}_\sigma \mathbf{u}_\sigma + \underline{\underline{\mathbf{I} P_\sigma}} \right) = q_\sigma n_\sigma (\mathbf{E} + \mathbf{u}_\sigma \times \mathbf{B}) + \sum_{\sigma'} R_{\sigma\sigma'}, \quad (4.5)$$

$$\frac{\partial \epsilon_\sigma}{\partial t} + \nabla \cdot [\mathbf{u}_\sigma (\epsilon_\sigma + P_\sigma)] = q_\sigma n_\sigma \mathbf{u}_\sigma \cdot \mathbf{E} + \sum_{\sigma'} K_{\sigma\sigma'}. \quad (4.6)$$

In these equations ϵ_σ is the energy density of the species,

$$\epsilon_\sigma = \frac{1}{2} m_\sigma n_\sigma \mathbf{u}_\sigma^2 + \frac{P_\sigma}{\gamma_\sigma - 1}, \quad (4.7)$$

with γ_σ being the adiabatic index, and $\sum_{\sigma'} R_{\sigma\sigma'}$ and $\sum_{\sigma'} K_{\sigma\sigma'}$ being the first and second moments of the collisional term, respectively. The adiabatic index for an ideal gas is 5/3, but for a partially-ionized plasma it is lower and was assumed to

be 1.15 for the aluminum plasma [46, 19]. In addition to the moment equations, above, we also need Faraday's and Ampere-Maxwell's law

$$\frac{\partial \mathbf{B}}{\partial t} = -\nabla \times \mathbf{E}, \quad (4.8)$$

$$\frac{\partial \mathbf{E}}{\partial t} = c^2 \nabla \times \mathbf{B} - \frac{1}{\epsilon_0} \mathbf{J}. \quad (4.9)$$

Above we have derived the standard two-fluid equations. XMHD and MHD models further simplify these equations by combining the two separate fluids into a single fluid. This allows us to define the total mass density, ρ , and center-of-mass velocity, \mathbf{u} , as

$$\rho = \sum_{\sigma} m_{\sigma} n_{\sigma}, \quad (4.10)$$

$$\mathbf{u} = \frac{1}{\rho} \sum_{\sigma} m_{\sigma} n_{\sigma} \mathbf{u}_{\sigma}. \quad (4.11)$$

In addition, the current density, \mathbf{J} , can be written as

$$\mathbf{J} = \sum_{\sigma} n_{\sigma} q_{\sigma} \mathbf{u}_{\sigma}. \quad (4.12)$$

Now the two-fluid equations (Eqs. 4.4-4.6) for each species can be combined together in order to get the standard MHD conservation equations

$$\frac{\partial \rho}{\partial t} + \nabla \cdot (\rho \mathbf{u}) = 0, \quad (4.13)$$

$$\frac{\partial (\rho \mathbf{u})}{\partial t} + \nabla \cdot (\rho \mathbf{u} \mathbf{u}) = -\nabla P + \mathbf{J} \times \mathbf{B}, \quad (4.14)$$

$$\frac{\partial \epsilon}{\partial t} + \nabla \cdot [\mathbf{u} (\epsilon + P)] = \mathbf{u} \cdot (\mathbf{J} \times \mathbf{B}) + \eta \mathbf{J}^2. \quad (4.15)$$

Here P and ϵ are the sum of the pressures and energies over all species, respectively, and η is the electrical resistivity. In addition to these equations, we also need the generalized Ohm's law (GOL) which is from the two-fluid electron

equation of motion, Eq. 4.5, with $\sigma = e$. Since $\mathbf{J}/n_e e = \mathbf{u}_i - \mathbf{u}_e$, and $\mathbf{u} \simeq \mathbf{u}_i$ all of the \mathbf{u}_e can be replaced by $\mathbf{u} - \mathbf{J}/n_e e$. The full GOL is

$$\frac{m_e}{n_e e^2} \left(\frac{\partial \mathbf{J}}{\partial t} + \nabla \cdot \left[\mathbf{u} \mathbf{J} + \mathbf{J} \mathbf{u} - \frac{\mathbf{J} \mathbf{J}}{n_e e} \right] \right) = \mathbf{E} + \mathbf{u} \times \mathbf{B} - \eta \mathbf{J} - \frac{\mathbf{J} \times \mathbf{B}}{n_e e} + \frac{\nabla P_e}{n_e e}. \quad (4.16)$$

We note that this is where the primary difference between XMHD and MHD codes exist. The electron inertial term (left hand side of the above equation) and Hall term ($\frac{\mathbf{J} \times \mathbf{B}}{n_e e}$) are computationally expensive due to the fast time scales needed to fully resolve them. Therefore, because of the belief that they are important only in low density plasma regions, MHD codes ignore these terms. However, both XMHD simulations and several HEDP experiments carried out at Cornell University have shown that these terms, primarily the Hall term, are important in plasmas previously believed to be well modeled by just MHD physics [9, 30, 31, 32]. PERSEUS, as well as other XMHD codes, must be able to efficiently handle both the electron inertial and Hall terms to be computationally competitive. In PERSEUS this is done by using a relaxation system that enables an implicit time advance of the electric field and the current density, which enables running simulations on a time scale similar to MHD simulations.

4.2 Simulation Method

The simulations presented in this thesis were all 2-D simulations that were carried out using one of 2 computational techniques. For both techniques we assumed the plasma to be azimuthally symmetric and modeled the r and z axis of the plasma, as shown in Fig. 4.1. The first modeling technique used was a finite volume (FV) method. We modeled the plasma on a grid of 20 mm (300 cells) in r by 20 mm (300 cells) in z , which resulted in a spatial resolution of 67 μm . Since

this is not high enough resolution to resolve the $15 \mu\text{m}$ foil, we had to scale the thickness of the foil to a single cell thickness in the axial direction, and make it less dense, $1.35 \times 10^{22} \text{ cm}^{-3}$, than solid density, $6 \times 10^{22} \text{ cm}^{-3}$, in order to match the mass and keep the ablation rate similar to experimental conditions. Other initial conditions were that everything started at a temperature of 0.026 eV, the background vacuum had a density of $6 \times 10^{13} \text{ cm}^{-3}$ singly charged Al ions, and the 2.5 mm radius center pin had a density of $6 \times 10^{22} \text{ cm}^{-3}$ which was masked to assure that the particles had no momentum within the pin, ensuring plasma would come only from the radial foil. This method also enabled separate temperatures for the electrons and the ions. The foil was placed 4 mm above the bottom of the computational grid. Current was driven through the foil by applying an azimuthal magnetic field along the bottom of the computational grid outside of the pin radius according to $B_\theta = \mu_0 I / 2\pi r$, where the sign of I determined the current polarity. The COBRA current pulse for these simulations was modeled by the following piecewise continuous function

$$I(t) = \begin{cases} I_{max} \sin^2\left(\frac{\pi t[\text{ns}]}{200}\right) & t < 110 \\ I_{max} \sin^2\left(\frac{\pi t[\text{ns}]}{200}\right) + 0.9 I_{max} \sin^2\left(\frac{\pi(t[\text{ns}] - 110)}{200}\right) & t \geq 110. \end{cases} \quad (4.17)$$

We used $I_{max} = 1.2 \text{ MA}$, and a comparison of this model with several short pulses produced by COBRA is shown in Fig. 4.2.

The other computational method used was discontinuous Galerkin (DG), which is significantly less numerically diffusive than the FV method. This code again ran 2D simulations, this time with 720 points in the r direction (20 mm) and 1080 points in the z direction (30 mm), which gave a spatial resolution of $27.8 \mu\text{m}$ as shown in Fig. 4.3. Switching to DG simulations, including the significantly higher resolution, enabled more details of the jet to be resolved. Howe-

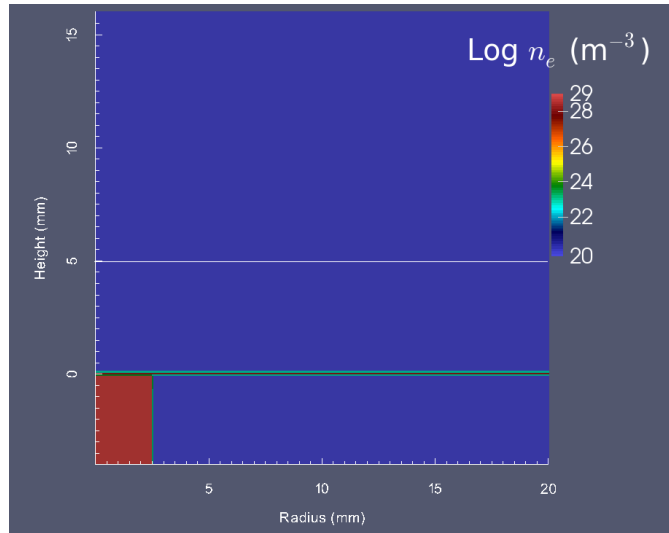


Figure 4.1: Diagram of the simulation space at the start of the FV simulation. The red region is the 2.5 mm radius pin, and the foil is 4 mm above the bottom of the simulation grid. The line across the grid at 5 mm represents the height of the Thomson scattering laser beam in the experiments.

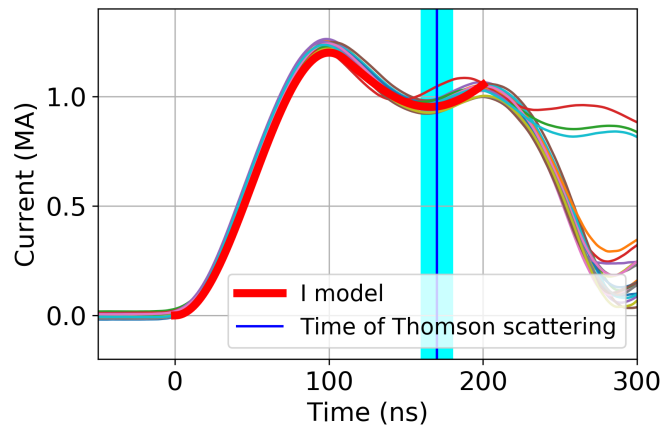


Figure 4.2: Comparison between experimental current traces and the computational model of the current (in red) from Eq. 4.17. We see that the shape agrees well with the experiment, though the intensity of the first peak could have been increased slightly. We also show the temporal range during which most Thomson scattering measurements were taken in the experiments.

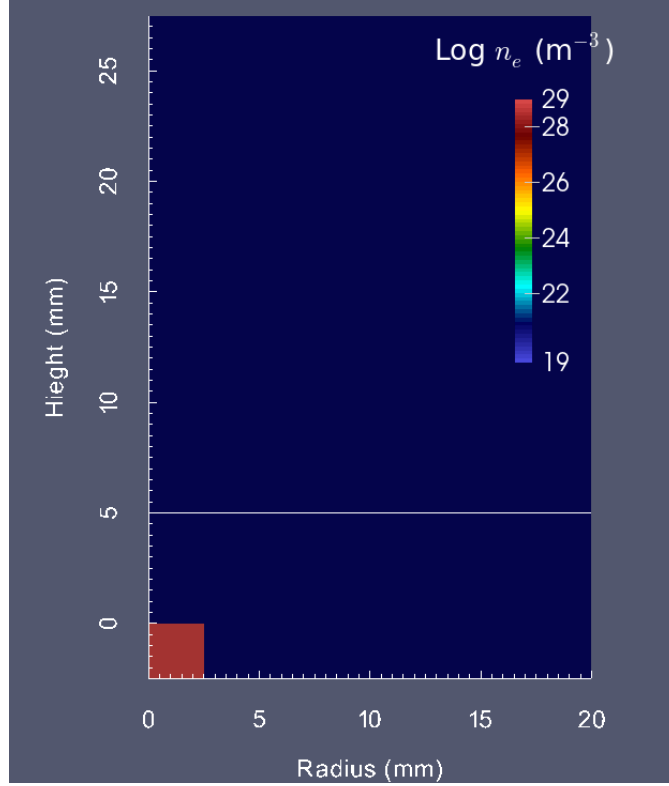


Figure 4.3: Diagram of the simulation space at the start of the DG simulation. The red region is the 2.5 mm radius pin, and the foil is 2.5 mm above the bottom of the simulation grid, at $z = 0$. The line across the grid at 5 mm represents the height of the Thomson scattering laser beam in the experiments.

ver, these simulations took days to run. The DG simulations also included more physics than the FV simulations as they included more accurate ionization, resistivity and transport models. However, it has a limitation not in the FV model, as it treated the plasma as a single temperature, instead of carrying separate ion and electron temperatures. Also, the current in the DG model was simpler than in the FV method

$$I(t) = \begin{cases} I_{max} \sin^2\left(\frac{\pi t[\text{ns}]}{200}\right) & t < 100 \\ I_{max} & t \geq 100, \end{cases} \quad (4.18)$$

and $I_{max} = 1 \text{ MA}$.

While we will present a detailed discussion on sources of possible errors in

these simulations when they are compared to experimental results in Sec. 5.5.2, some limitations of PERSEUS can be discussed currently. The first is that even with the detailed DG simulations, we were not able to fully resolve the foil. While the DG code does a better job at modeling the phase transitions of the foil, not fully resolving it is an obvious source of error. In addition, neither of these models included radiation effects, which, while expected to be small for these plasmas, will have some effect on the plasma parameters. Other sources of error include: closing the system after the second moment, the model for ionization, and the model for various transport effects.

CHAPTER 5
THOMSON SCATTERING RESULTS

5.1 Jet Rotation Measurements

The first major interest in using Thomson scattering on plasma jets was to measure the rotation of the jet when exposed to an external magnetic field [8]. This rotation is caused by the $J_r B_z$ component of $\mathbf{J} \times \mathbf{B}$ caused by the external magnetic field and the current density in the foil. This research was an expansion of earlier experiments using optical spectroscopy to measure the rotation of the plasma [62]. These early experiments did not resolve the rotation inside the jet, but were able to make measurements outside of the jet. In order to measure v_θ of the plasma, we needed to collect scattering from at least two different scattering angles using the method discussed in Sec. 3.3.1. To achieve this comparison of the shifts in the Thomson scattering profile, 3 scattering angles were used, two in a plane that was perpendicular to the axis of the jet, and at opposite 90° to the laser, and another looking straight down the axis of the jet. The first two fibers are in what we will call the $r - \theta$ plane, while the third fiber is in what we will call the $r - z$ plane. This setup, including the resulting \mathbf{k} vectors, is shown in Fig. 5.1. The two fibers in the $r - \theta$ plane can be used to measure v_r and v_θ through a comparison of the Doppler shifts. The single fiber in the $r - z$ plane can be used to measure v_r and v_z through the assumption of the jet being symmetric and comparing the Doppler shifts on each side of the jet. Figure 5.1a also shows the simulation results for the density of a magnetized jet in RP, showing how these jets are hollow on axis.

Sample spectra for the two fibers in the $r - \theta$ plane are shown in Fig. 5.2. As

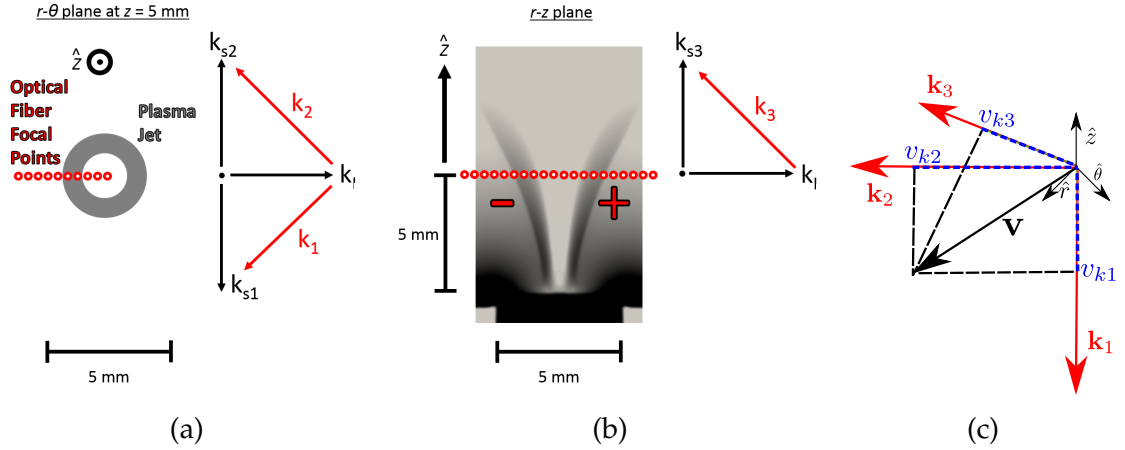


Figure 5.1: (a) shows an r - θ plane slice of the plasma at a height of 5 mm. It shows a representation of the alignment of the fibers in the r - θ plane relative to the jet and \mathbf{k} , \mathbf{k}_s , and \mathbf{k}_l in this plane. (b) shows the same jet, but now in the r - z plane. We see a representation of the alignment of the fibers that were along the z -axis, as well as all \mathbf{k} , \mathbf{k}_s , and \mathbf{k}_l that are in this plane. (c) shows the 3-D representation of \mathbf{k} for the 3 scattering directions, along with the representation of v_k along all three directions for an arbitrary ion velocity. Reproduced from [8], with the permission of AIP Publishing.

a reminder, v_r is obtained from a scaled average of the Doppler shifts of each profile, while v_θ is obtained from the scaled difference of the Doppler shifts. We see here that on some of the fibers there are significant differences in the centers of the profiles, indicating that there is indeed rotation in the plasma jet. Figure 5.3 shows the results of these measurements for a typical shot in RP. This measurement was taken 160 ns into the current pulse and the applied magnetic field was -0.9 ± 0.1 T (with the negative direction being defined as anti-parallel to the direction of jet propagation). For these figures $r = 0$ is defined as the center of the jet, $r < 0$ is the laser incoming side, and $r > 0$ is the laser exiting side. For all of these measurements, \hat{r} points outward from the center of the jet, while $\hat{\theta}$ points in the counter clockwise direction. We see that we measured within the jet a rotation of 15-20 km/s. Confirmation that we are indeed measuring the rotation of the jet is shown in Fig. 5.4. Here we see that

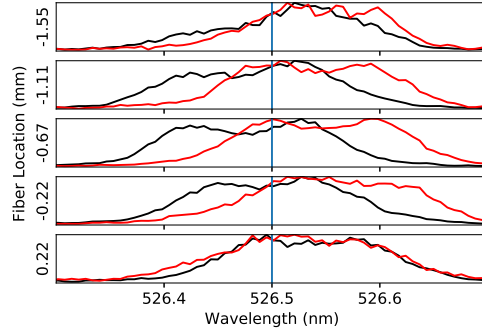


Figure 5.2: Here we show the raw spectra from the individual fibers for a typical shot in reverse polarity with $-0.9 \text{ T } B_z$. The plots show the spectrum from the fiber collecting scattering along \mathbf{k}_{s1} in black, while the fiber along \mathbf{k}_{s2} is in red, and the laser wavelength is in blue. Reproduced from [8], with the permission of AIP Publishing.

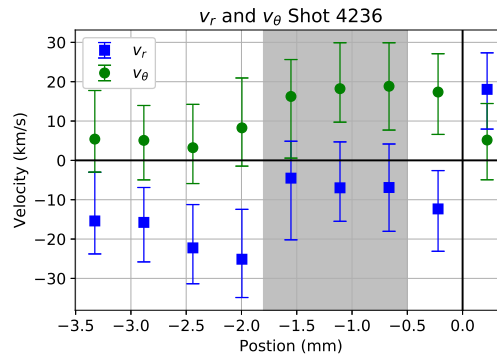


Figure 5.3: Shows the measured velocity components, v_r and v_θ , at $z = 5 \text{ mm}$, for a typical shot in reverse polarity with $-0.9 \text{ T } B_z$. The gray shaded regions in this figure represents the dense conical shell of the jet, estimated from fibers with increased Thomson scattering intensity. Reproduced from [8], with the permission of AIP Publishing.

the direction of the rotation changes sign, as expected, if either the direction of current flow or the magnetic field is switched. In addition, the region of rotation is significantly narrower for the SP jet, but that is expected as those jets diverge less. The directions of these rotations are consistent with the direction of the $J_r B_z$ component of the $\mathbf{J} \times \mathbf{B}$ force that is causing the rotation.

In addition to the ion flow velocities measured by fibers in the $r - \theta$ plane,

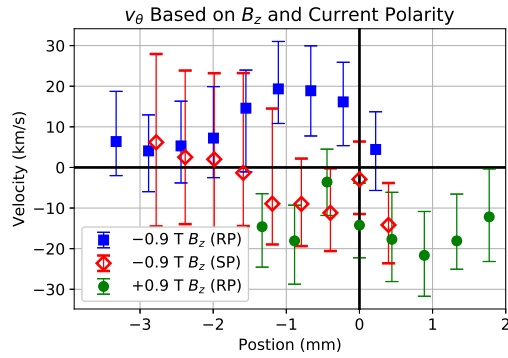


Figure 5.4: Here we see the effect on v_θ when changing either the direction of B_z or the polarity of the current. The blue squares show the same results as Fig. 5.3, and are in reverse polarity, RP, with -0.9 T B_z . The green circles show the results when B_z changes signs, $+0.9$ T B_z , and the red diamonds show the results of changing the current polarity (to standard polarity, SP, with a cathode pin). We see that both of these changes switch directions of the plasma rotation, consistent with the $J_r B_z$ component of the $\mathbf{J} \times \mathbf{B}$ force that causes the rotation. Reproduced from [8], with the permission of AIP Publishing.

a single fiber in the $r - z$ plane was used to measure v_r and v_z . Results for measurements of all three velocities for a reverse polarity shot is shown in Fig. 5.5. We see in this result that the two methods for measuring v_r agree and that the plasma in the jet is moving up at a speed of between 50 and 100 km/s. Outside the jet the plasma tends to be moving up faster while it slows down as the plasma approaches the axis. Comparing these results to simulations, Fig. 5.6, we see several noticeable differences. The major difference is that near the axis of the jet the simulation tends to predict a high axial and azimuthal velocity. These high velocities, however, occur at a significantly lower density than the rest of the jet. Measurements within the dense region as well as outside of the jet appear to be in reasonable agreement with the simulations.

If the simulation results on axis of the jet are physical, they are difficult to see experimentally due to the low density. Since the power scattered is proportional to the density of the plasma, scattering from a region that has a density of

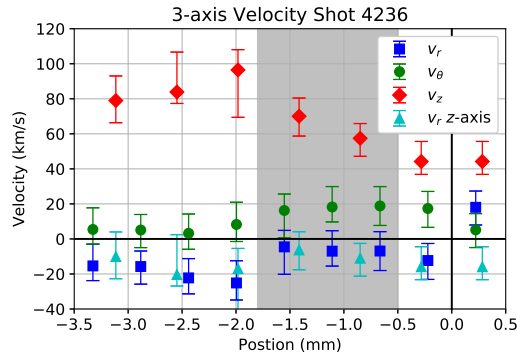


Figure 5.5: Measure of ion flow velocity at 160 ns along all 3 axes for shot 4236. We see that in the jet the ions are rotating at 15-20 km/s. Two measurements for the radial component are shown with blue squares and cyan triangles. The jet was moving upward at a velocity of between 40-90 km/s, with increasing velocity going away from the center of the jet. The gray shaded region represents the location of the jet. Reproduced from [8], with the permission of AIP Publishing.

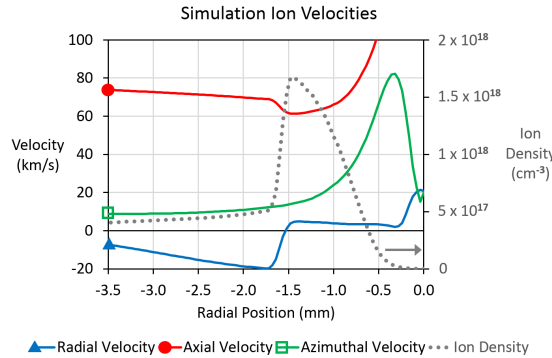


Figure 5.6: Simulation ion velocities in the radial, axial, and azimuthal directions for a lineout 5 mm above the foil at 160 ns after the start of current rise. Overlaid ion density (gray dotted line) helps to indicate the region of the jet. Reproduced from [8], with the permission of AIP Publishing.

only $\sim 5 \times 10^{16}$ compared to scattering from a region with a density of $\sim 5 \times 10^{18}$ will be significantly weaker. With our spot size, $340 \mu\text{m}$, if any of the higher density jet region is within the scattering volume it would overwhelm the scattering from the less dense region. Therefore, in order to test to see if this high velocity region is indeed true, both tighter laser focus and a smaller collection area would be needed. In addition, the smaller collection volume would incre-

ase the signal relative to the continuum, increasing the opportunity to be able to see the scattering at a lower density.

5.2 Preliminary Jet Heating

Though Thomson scattering is a very powerful diagnostic technique, ideally the laser should not perturb the plasma. This is an important limitation since if the laser perturbs the plasma, it can affect the measurements. Therefore, it is important to know which measurements are affected by the perturbation and which are not.

Early in our experiments, we noticed with other diagnostics that when the Thomson scattering laser passed through the plasma the jet showed a bubble as a result of the laser. An example from an XUV image of this effect is shown in Fig. 5.7. The bubble lasts for 10s of ns after the laser pulse and moves up and expands in time.

In order to see if we were perturbing the plasma on the time scale of the laser pulse, two different sets of experiments were performed. The first set of experiments used the full power of the Thomson scattering laser (10 J in 2.3 ns FWHM), while the second set of experiments did not use the last amplifier of the laser and operated at only 1 J. Results from the average velocity measurements in these experiments as well as the average temperature measurements are shown in Fig. 5.8. These graphs show the velocity measurements are largely unaffected by the laser, as they are comparable between the two laser energies. This means that the laser does not affect the overall fluid velocity and the results from the previous section can be trusted. The electron temperature, however, is

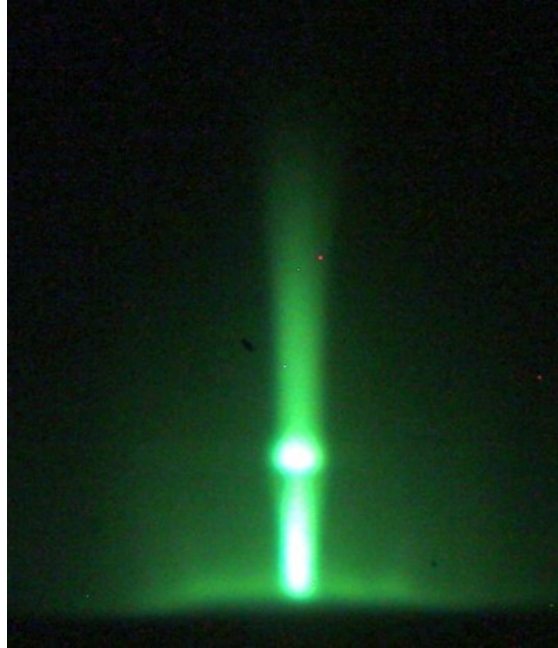


Figure 5.7: An XUV image of the plasma jet with the laser going through it. The intensity bubble in the image is a result of the laser perturbing and heating the plasma jet.

significantly different between the two probe laser energies. This means that the jet is heating up from the probe laser, and that effect occurs on the time scale of the laser pulse.

The primary mechanism for the laser to heat the plasma jets is known as inverse bremsstrahlung. This occurs because electrons that are accelerated by the laser's electric field collide with ions, which randomizes the electron motion, increasing the electron temperature. The ions will also be heated, but only by the newly hot electrons, so they are heated on the ion-electron energy transfer time, which is a few nanoseconds.

In order to see if it is reasonable for the laser to perturb the plasma jet by inverse bremsstrahlung, one needs to compare the energy density of the plasma jet and the energy density absorbed from inverse bremsstrahlung. If the ab-

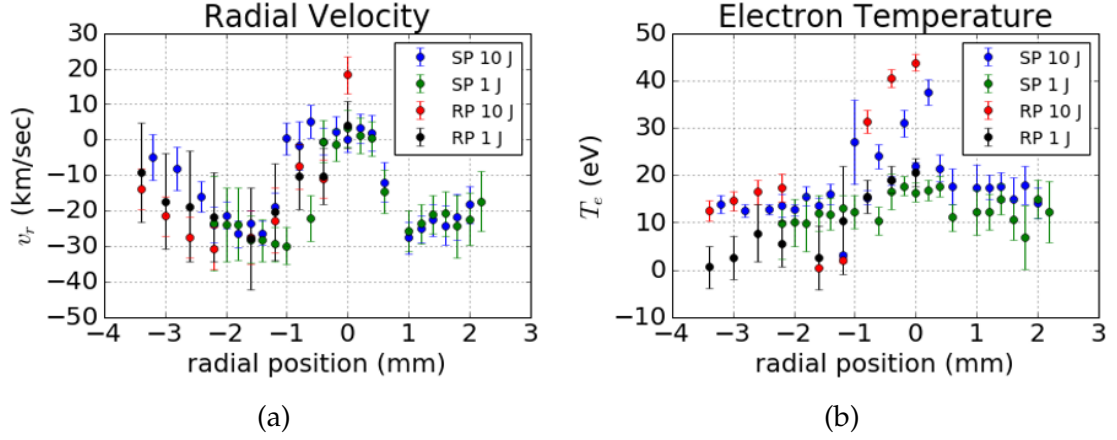


Figure 5.8: Averaged results showing the radial velocity as a function of position (a) and electron temperature (b) based on the probe laser energy and the current polarity. Though T_e is clearly affected by the input laser energy, there does not seem to be any effect on the radial velocity of the plasma.

sorbed energy density is at least a significant fraction of the energy density of the plasma jet, then the laser will influence the plasma. Since we are primarily concerned with the interaction and heating of the electrons, we will estimate the plasma electron energy density from $E = 3n_e T_e / 2$. If we use a density of $n_e = 5 \times 10^{18} \text{ cm}^{-3}$ and $T_e = 20 \text{ eV}$, the energy density is $2.4 \times 10^7 \text{ J/m}^3$. The absorbed laser energy density can be estimated from KE/A , where K is the inverse bremsstrahlung absorption coefficient defined by Dawson and Oberman [15, 16, 41], E is the input laser energy, and A is the cross section of the laser. The factor K term is given by [16, 41]

$$K = \frac{64\pi^3 Z^2 n_e n_i e^6 \ln \Lambda(\omega_l)}{3c\omega_l^2 (2\pi m_e k_b T_e)^{3/2} (1 - \omega_{pe}^2 / \omega_l^2)^{1/2}}, \quad (5.1)$$

where $\Lambda = \sqrt{1 + (b_{max}/b_{min})^2}$ with $b_{min} = Ze^2/k_b T_e$, as we are focusing on classical effects, and $b_{max} = v_{Te}/\omega_l$ [53]. This equation is in CGS units, with temperature in Kelvin, and k_b is Boltzmann's constant. We note that this is different from the traditional value for the Coulomb logarithm, $\ln \Lambda$, as we are using ω_l (the laser frequency) instead of ω_{pe} . Using the same parameters as used for the jet above,

we find that $K = .019 \text{ cm}^{-1}$. Then, taking $E = 10 \text{ J}$ and $A = 9.08 \times 10^{-4} \text{ cm}^2$ gives an energy density of $2.1 \times 10^8 \text{ J/m}^3$. This is clearly higher than the energy density estimated for the plasma, meaning that the laser will heat the plasma jet by inverse bremsstrahlung.

5.3 Time Resolved Jet Heating

One then would want to use the laser with a low enough energy to not perturb the jet, while providing a high enough signal-to-noise ratio (SNR) to measure the Thomson scattering. This could be done by going to lower laser energies, 1 J, but we were struggling to get enough SNR to make good measurements. In addition, we would not know if the jet was perturbed at 1 J without going to even lower laser energies. Instead, we decided to gather time resolved Thomson scattering, giving a time history of the plasma during the laser pulse.

These experiments were all performed with no magnetic field and at either 10 or 1 J of laser energy. The typical results for 10 J of laser energy is shown in Fig. 5.9. For fitting we used the $T_i = T_e$ method, used $n_e = 5 \times 10^{18} \text{ cm}^{-3}$, and calculated error bars by the MC method. Here the plasma is measured to heat from 25 eV up to 85 eV within the first 2 ns of the laser pulse before cooling down to 70 eV at the end of the laser pulse. This cooling occurs after the peak of the probe laser energy. We also compared the results of a time gated image taken on the same shot, and a time integration of the streak signal to see how the measured temperatures compare. In this case we see that the measured temperatures from the two viewing angles are different, though both show heating compared to the starting measured temperature of the plasma. These differen-

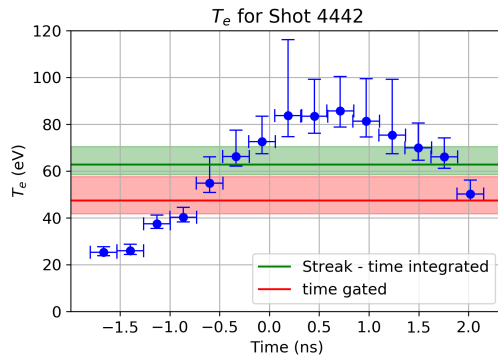


Figure 5.9: The electron temperature for a typical Al jet with 10 J of laser energy. Time zero for all these plots is the peak intensity of the scattered radiation, which in this figure is 170 ns after the start of the current pulse. The blue circles are the data for each time segment (time width of 270 ps), the green line and region is the best fit and error bars if the entire streak signal is time integrated, and the red region is the measurement from the gated camera. The y-axis error bars represent one sigma errors from the Monte Carlo simulation, while the x-axis error bars are the time period of a single measurement. [1]. ©2018 IEEE

ces could be due to slight differences in alignment, or the fact the streak camera had a field of view of $325 \mu\text{m}$ while for the gated camera, each fiber had a field of view of $150 \mu\text{m}$.

The mechanism for the heating has been discussed already, but the rapid decrease in measured temperature of the plasma is also important to discuss and there are two key contributions. The first is that the upward velocity of the plasma jet causes colder electrons to enter the scattering volume, and those may begin to dominate as the laser power decreases and heats the plasma less. The plasma is moving on the order of $100 \mu\text{m}/\text{ns}$, meaning that electrons pass through most of the scattering volume within a single laser pulse. The other possible cause for cooling is that, as explained by Dawson [16] and Basov and Krokhin [3], as a plasma is heated by a laser, it also expands, and in the long time limit, about 1/4 of the laser energy goes into heating the plasma, while the

rest of the energy goes into expansion. In addition, the plasma becomes more transparent to the laser as the density decreases and the temperature increases, causing energy to be coupled less efficiently into the plasma in the scattering volume. In this discussion it is important to remember that we are measuring the average value of T_e within the scattering volume.

To figure out which factor is more important to the cooling we can expand a model developed by Basov and Krokhin [3] and Dawson [16]. They modeled the plasma as an ideal gas of electrons and ions and found the average energy within the region of both plasma and laser assuming a uniform density and temperature. This enables the creation of the following equation for the conservation of energy

$$\frac{d}{dt} \left(\bar{M} \frac{\dot{r}^2}{2} + E \right) = Q, \quad (5.2)$$

where \bar{M} is the average mass of the plasma, \dot{r} is the rate of the gas expansion, E is the energy of the plasma, and Q is the absorbed power of the laser that is heating the plasma. In order to get an equation for motion for the plasma, we can set $Q = 0$ in the conservation of energy equation and have $\frac{dE}{dt} = P \frac{dV}{dt}$ which gives

$$\frac{d}{dt} \left(\bar{M} \frac{\dot{r}^2}{2} \right) - P \frac{dV}{dt} = 0. \quad (5.3)$$

Now assume that the plasma has a spherical volume, $V = 4\pi r^3/3$, that $P = (N_e T_e + N_i T_i)/V$, with N_e and N_i being the total number of electrons and ions, respectively, and that $E = 3/2(N_e T_e + N_i T_i)$. We have expanded on their model by using separate values for T_e and T_i and assuming that T_i will remain constant as the ions should heat up slower than the electrons due to the fact that the ion-electron energy transfer collision time is about 2 ns. These assumptions result in the following coupled equations (with the first from Eq. 5.2 and the second

from Eq. 5.3)

$$\bar{M}\ddot{r} + \frac{3N_e}{2}\dot{T}_e = Q \quad \text{and} \quad \bar{M}\dot{r}^2 = \frac{3(N_e T_e + N_i T_i)}{r}. \quad (5.4)$$

These two equations then can lead to an iterative numeric solution for both T_e and r that we can use to track the temperature of the plasma. The absorbed laser power is $Q = rKP_l$, where K is the absorption coefficient discussed earlier (Eq. 5.1), P_l is the power of laser, and we assume that r starts at the radius of the probe laser and uses r from the previous time step. As the laser pulse is Gaussian in time, we model P_l by

$$P_l = \frac{E_{tot}}{\sqrt{2\pi}\sigma_t} e^{-\frac{t^2}{2\sigma_t^2}}, \quad (5.5)$$

where E_{tot} is the total laser energy, σ_t is the FWHM of the pulse, and t is the time relative to the peak laser energy. In addition, we will account for the upward motion of the plasma by creating an array of cells in the z direction, such that the plasma will move up one cell in a single time step. Therefore both T_e and r will move one cell each time step, and the entering (initial) plasma conditions will be added to the bottom cell.

Tracking the average value for T_e over all cells for 100 time steps, assuming that $\bar{M} = N_i m_i$, $n_e = 1 \times 10^{19} \text{ cm}^{-3}$, $T_{e0} = 15 \text{ eV}$, $r_0 = 170 \text{ }\mu\text{m}$, and $v_z = 60 \text{ km/s}$, gives the results shown in Fig. 5.10a. In this figure we see the results of this calculation in red and the results from a typical shot in blue. There is remarkable agreement between the model and the experiment, including the cooling at the end of the laser pulse. Since we are interested here in the primary cause of the plasma cooling, we can change v_z to something very small, in this example dropping it by a factor of 100. The results for this change are shown in Fig. 5.10b. We see that even though there is a slight decrease in the heating of the plasma overall the shape is still the same. Therefore, the motion of the plasma does not

significantly affect the cooling of the plasma, which is primarily a result of the expansion from the laser heating.

The less heating for the slow-moving plasma can be explained by looking closer at the two cases. In the slow-moving case, all the plasma in the scattering volume is at the same expanded density and heated temperature. However, for the case of the faster moving plasma, there is consistently new (colder and denser) plasma entering the scattering volume. Since the absorbed laser energy scales by $n_e^2 T_e^{-3/2}$, the newer plasma will be heated more rapidly than the already hot expanded plasma, allowing more laser energy to be coupled into the plasma. If the plasma jet is moving with a velocity such that transverses the laser focus during the laser pulse, the extra heating from the new plasma adds more to the average temperature of the plasma than is lost to hot plasma moving out of the scattering volume. We note that there is very good agreement between the model, when using experimentally reasonable values, and the experiments. However, due to the simplicity of this model we have not attempted to use this model to make detailed comparison with experimentally measured plasma parameters or the measured laser focus.

In order to help confirm that this heating was indeed an effect of the 10 J laser interacting with the plasma, two additional tests were performed. The first (Fig. 5.11a) was to look about 20 ns later into the current pulse, at 190 ns. It is apparent that even 20 ns later the Thomson scattering result is very similar and, therefore, we are measuring an effect of the laser. In addition, shown in Fig. 5.11b, experiments were performed using only 1 J of laser energy. From these results it is clear that the plasma is not significantly heated when using 10 times less laser energy. In addition, the measured temperature is slightly less

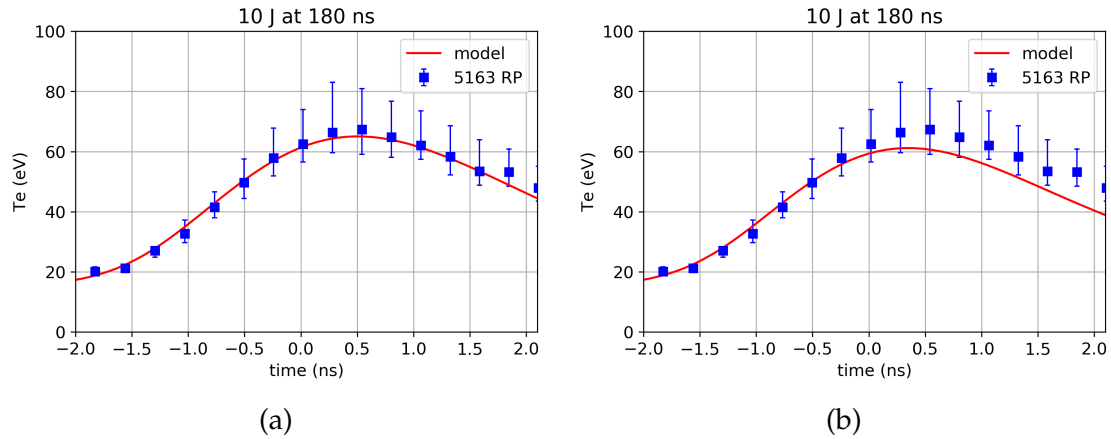


Figure 5.10: Comparison between experimental data (blue) and a model (red) of the laser heating the plasma. For part (a) the model had $v_z = 60$ km/s and for part (b) $v_z = 0.6$ km/s. Both graphs show similar cooling, which means that cooling is due to plasma expansion and not the heated plasma leaving the scattering volume.

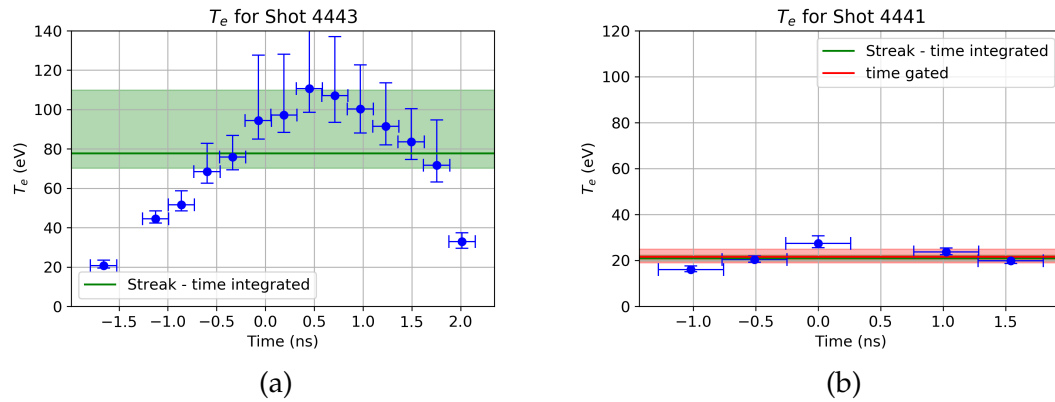


Figure 5.11: Results for a 10 J shot at 190 ns (a) and 1 J shot at 180 ns (b). The later time shot has a similar profile to that of the shot taken at 170 ns, showing that the plasma jets have similar plasma parameters over a time scale of 10s of ns. For the 1 J shot, the jet temperature stays relatively constant, unlike when using 10 J of laser energy [1]. ©2018 IEEE

than the initial temperature of the 10 J shot. This means that the plasma may be heated by the laser before we are even able to make our initial temperature measurement with a 10 J laser pulse.

5.3.1 Ti Results

In addition to the experiments performed with an Al foil, some of the initial streaked experiments were performed using a Titanium (Ti) foil. It was shown by Byvank *et al.* [10, 11] that the structure of the jet, at least in the presence of a magnetic field, can be significantly affected by the choice of foil material. Figure 5.12a shows T_e as a function of time from a typical experiment that used a Ti foil and 10 J of probe laser energy. We see that the Ti jet was heated more than a typical Al jet. Titanium jets started from 50 eV and rose to a peak electron temperature of 225 eV before leveling off at 150 eV. However, this 225 eV temperature measurement occurred during a time when there were complex features in the Thomson scattering signal, to be discussed shortly. When only 1 J of laser energy, such as is shown in Fig. 5.12b, was used the plasma was shown to be at about 50-70 eV. We note, however, that we are not able to measure T_e before the peak of the scattered radiation. This is due to a very sharp feature in the spectrum and not being able to see two clear peaks, see Fig 5.13. While this sharp feature will be discussed shortly, the IAW peaks do appear to be moving apart in time, indicating heating. This means that the even for 1 J we are heating the plasma, and that in the 10 J Ti shots we do not have enough SNR to measure T_e prior to the jet being perturbed by the laser. This suggests that there are significant differences in the laser heating of the plasma jet based on the material. One possible explanation of this is that the laser absorption coefficient, K , scales with the ionization state Z . FLYCHK tables predicts a higher Z for Ti than Al at comparable temperatures and densities (8.3 compared to 6.0 at $T_e = 23$ eV and $n_e = 1 \times 10^{19}$ cm⁻³) [13].

Another interesting feature of the Thomson scattering profile from the Ti

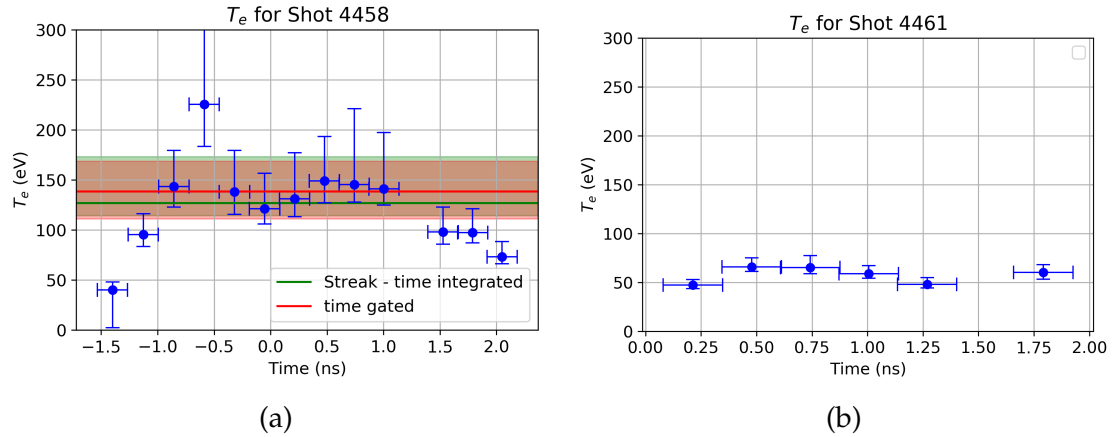


Figure 5.12: The electron temperature for a typical Ti jet with 10 J of laser energy in (a) and with 1 J of laser energy in (b) [1]. ©2018 IEEE

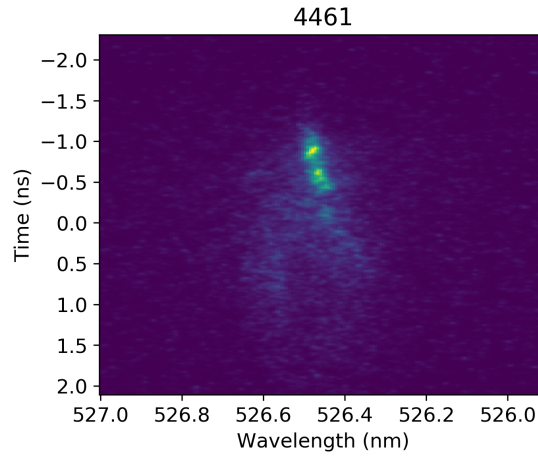


Figure 5.13: The raw data from the 1 J Ti shot. Shows that we have one bright sharp peak for the start of the laser pulse, making it impossible to make measurements of the electron temperature. Peaks could be moving apart at early times, suggesting we are even heating the plasma with 1 J.

plasma jet is that there are often very sharp scattering features that are not apparent in the Al spectrum. A comparison of typical scattering profiles is shown in Fig. 5.14. This could suggest several possible key differences between the plasmas created from these two materials. The first possibility is that T_i is significantly smaller for the Ti jets than the Al jets, since a lower ion temperature would cause weaker Landau damping, leading to sharper ion-acoustic peaks.

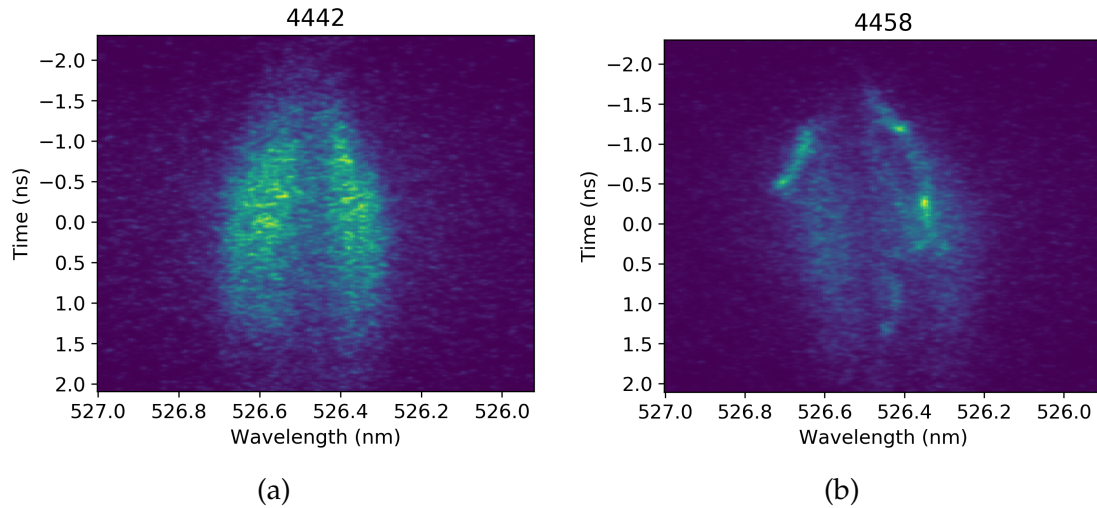


Figure 5.14: A comparison between the streaked spectra for an Al jet (a) and a Ti jet (b). During the first half of the laser pulse the Ti jet has significantly narrower ion-acoustic peaks than the Al jet does [1]. ©2018 IEEE

Another reason these peaks could be narrower is that the plasma outside the jet could be coming into the jet slower for Ti than Al, which would cause lower velocity gradients within the scattered volume and, therefore, narrow the peaks. Measuring this flow velocity for magnetized Al jets was already discussed, but further experiments are needed to compare the velocities of unmagnetized Al and Ti jets. A third possibility is a collisional difference between the two plasmas. Though a full collisional model is challenging to add to Thomson scattering, basic models show that collisions can significantly affect the width of the peaks [71]. Finally, since the sharp peaks in the Ti spectra last for a short period of time, they could be scattering from some complex wave within the plasma and not the result of traditional IAW Thomson scattering.

These sharp Thomson scattering features occur when the electron temperature appears to be rapidly increasing for the first nanosecond, before rapidly dropping to a more stable temperature. After these sharp peaks disappear from the spectrum, the electron temperature drops from 225 eV down to 150 eV. Look-

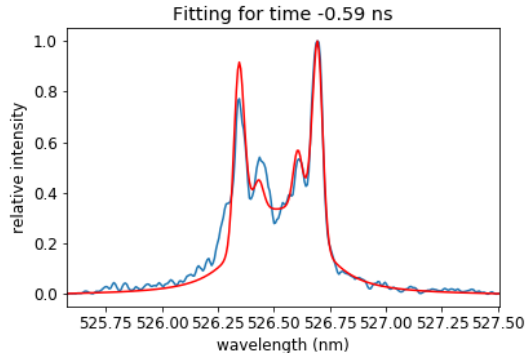


Figure 5.15: Results from a Ti shot where there were possibly four IAW peaks. This could suggest two different species in the scattering volume, or some complex wave. Assuming they are all IAW features, the resulting electron temperatures are 230 and 42 eV.

ing more closely at the region near the end of the sharp Thomson scattering feature, we see that there are actually two pairs of Thomson scattering peaks, Fig. 5.15. Fitting each pair of peaks with separate values for T_e results in the two electron temperatures being 230 and 42 eV. This continues to suggest that the sharp Thomson scattering peaks may be the result of some complex feature of the plasma, such as a non-linear wave or two species within the plasma. More experimental data, possibly looking at the jet from different angles, are needed to understand what is happening here.

5.4 Density Measurements

In addition to the measurements of electron temperature already discussed, it was also desired to use Thomson scattering to measure the density of the plasma. This would complement the interferometry measurements and address two weaknesses of those measurements. The first is that in interferometry the density measurements are limited by the ability to trace fringes. While in-

terferometry is fundamentally limited by the critical density, tracing complex fringe patterns can make measurements impossible well below the critical density. Thomson scattering is still limited by this critical density but should be able to measure significantly higher densities. In addition, interferometry measures the areal density of the plasma, i.e., line integrated density along the laser line of sight. Therefore, it requires an Abel transform in order to find the volumetric density, causing a limited capability near the axis of the plasma and the need for the plasma to be axisymmetric. Since Thomson scattering measurements are limited to the scattering volume, it makes a local measurement of the density and, therefore, does not have these line integration issues. We will now discuss two different techniques to use Thomson scattering to measure the density.

5.4.1 Ion Acoustic Wave Feature

The first technique used to attempt to measure the electron density was through the IAW feature. Looking back at the equation for peak separation, Eq. 3.103

$$\Delta\lambda_{iaw} \approx \frac{4}{c}\lambda_l \sin(\theta/2) \sqrt{\frac{T_e}{m_i} \left[\frac{Z}{1 + k^2\lambda_{De}^2} + \frac{3T_i}{T_e} \right]}, \quad (5.6)$$

we see that there is both a density and scattering angle dependence through the $k^2\lambda_{De}^2$ term. Therefore, by looking at two different wave vectors and comparing the peak separation, it may be possible to measure the density of the plasma [24]. These wave vectors can be created by using two scattering angles, or two different probing wavelengths. A key limitation with this approach, however, is that $k^2\lambda_{De}^2$ from the two scattering wave vectors must lead to a significant difference in the $(1 + k^2\lambda_{De}^2)^{-1/2}$ term. For our laser heated plasma jets, with $T_e = 50$ eV and $n_e \approx 5 \times 10^{18}$ cm⁻³, scattering from 60° and 150° results in a

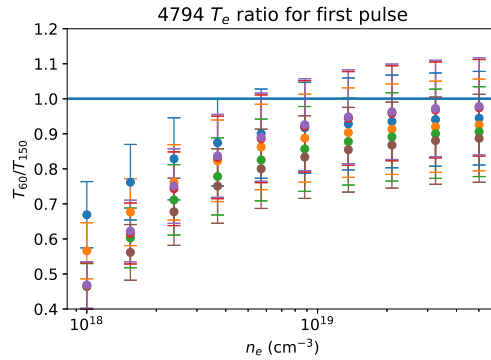


Figure 5.16: Comparison of the ratio of the best fit electron temperature between the two different scattering angles based on the assumed electron density. This data was taken with 2.5 J of laser energy and the different colors show the ratio at different times into the laser pulse. Reproduced from [2], with the permission of AIP Publishing.

10% difference in peak separation as $k_{60}^2 \lambda_{De}^2 = 0.0786$ and $k_{150}^2 \lambda_{De}^2 = 0.2934$.

In order to check the validity of this method for our plasma, we compared the ratio of the electron temperature fit from these two different scattering angles for various assumed densities, with sample results being shown in Fig. 5.16. The error bars assumed that the temperature fits had an error of 10%, and the various colors show the results from different times into the laser pulse. The density is found by looking at when the ratio is one, as that means that the fits from the two angles give the same electron temperature within error bars. We see that there is a problem of using this technique for our plasma: all of the ratios above $n_e = 3 \times 10^{18} \text{ cm}^{-3}$ overlap with one, and the ratio is relatively constant above $n_e = 1 \times 10^{19} \text{ cm}^{-3}$. This means that it is impossible to get an accurate measure of the plasma density. The reason is that $(1 + k^2 \lambda_{De}^2)^{-1/2}$ is not different enough from the two scattering angles in the density and temperature range explored here. The data over several shots, however, did suggest that the density was at least $2 \times 10^{18} \text{ cm}^{-3}$

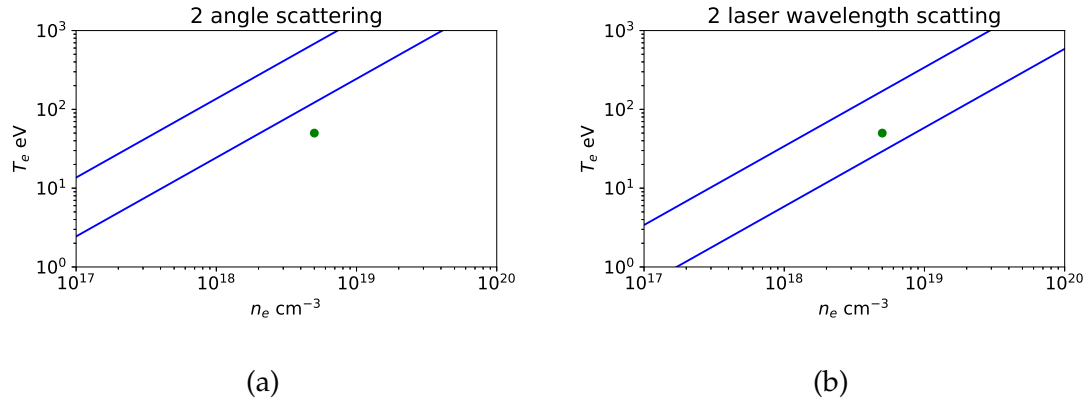


Figure 5.17: Plots showing the viability of using Thomson scattering from 2 different wave vectors in order to measure density of the plasma, with the viable region in between the two blue lines, and the green dot being our estimated plasma parameters. In (a) we see our current setup, using a laser wavelength of 526.5 nm and scattering angles of 60° and 150°. (b) shows a proposed set up that involves collecting from 2 different laser wavelengths (526.5 nm and 263.25 nm) both at 150°. Reproduced from [2], with the permission of AIP Publishing.

Though this technique clearly did not work for plasma jets, we can take what was learned here in order to form a boundary region of where this technique would be able to work. We know that $(1 + k^2 \lambda_{De}^2)^{-1/2} = (1 + 1/\alpha^2)^{-1/2}$ needs to be significantly different for the two wave vectors. As a reminder $k^2 \lambda_{De}^2 \propto k_l^2 \sin^2(\theta/2) \frac{T_e}{n_e}$. For a lower limit to $1/\alpha^2$, we can say the $(1 + k^2 \lambda_{De}^2)^{-1/2}$ term for two wave vectors must differ by at least 20%. For an upper limit we are limited by the fact that we need to be able to see the IAW feature, meaning that $\alpha > 0.5$. Figure 5.17a shows the region where this is valid as well as where our plasma currently resides, which we clearly see is out of the region of viability. In order to make this technique viable for our plasma, two different probing wave lengths could be used. An example of this is shown in Fig. 5.17b using a scattering angle of 150° and 526.5 and 263.25 nm for laser wavelengths, in which case the plasma parameters are in a valid region for this diagnostic.

5.4.2 Electron Plasma Wave Feature

Though using Thomson scattering from the IAW feature at two different angles did not result in accurate measurements of the density, the EPW feature of the Thomson scattering spectrum can give an accurate measure of the plasma density. While this is, in principle, a better way to measure the plasma density, it is difficult as the scattered intensity per unit wavelength from the EPW feature is on the order of 100 times smaller than that from the IAW feature, causing plasma continuum emission to be a problem. This means that careful design of the optical system is needed to maximize the amount of scattered laser light collected relative to the continuum. This encouraged the development of a significantly improved collection optical system using achromatic doublets as discussed in Sec. 2.3.3.

While we have not yet been able to record measurable EPW features inside of the jet on every shot, we do have a few shots with spectra that can be analyzed. We focus this discussion on a comparison between two different shots with jets in the SP current configuration. The raw data for the first of these shots is shown in Fig. 5.18; it was taken 170 ns into the current pulse. For a determination of the electron density, we are measuring the separation between the peaks on the opposite sides of the laser wavelength, which to first order is proportional to $\sqrt{n_e}$. Therefore, we see by eye that near the axis of the plasma, where the jet is, the plasma has a higher density than in regions outside of the jet. The density results from fitting each of the spectra in Fig. 5.18 are shown in Fig. 5.19. We see that outside of the jet the density is around $6 \times 10^{17} \text{ cm}^{-3}$, while in the jet region the density increases to $5 \times 10^{18} \text{ cm}^{-3}$.

Since the goal of this is to complement the interferometry measurements of

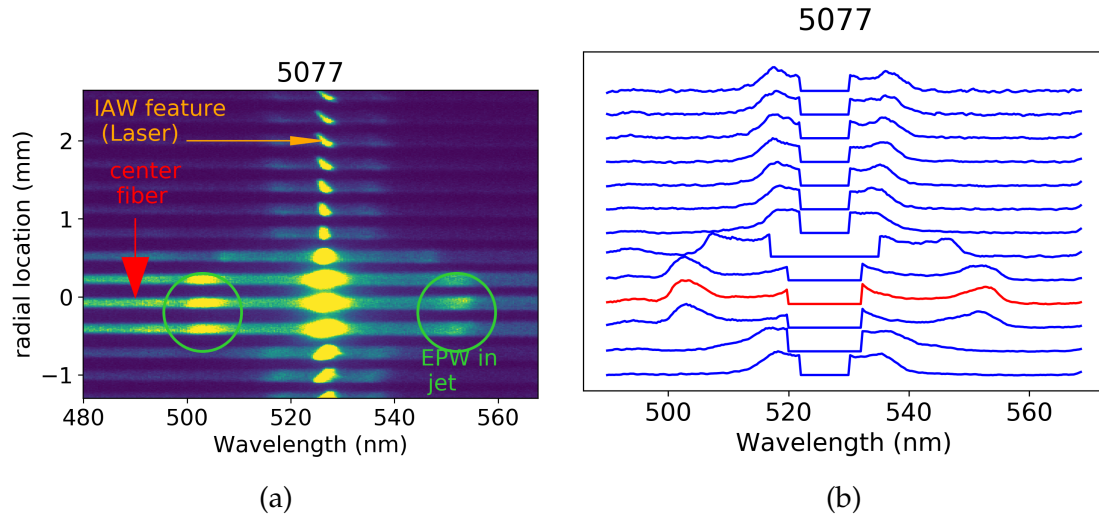


Figure 5.18: (a) is the raw data from a single SP shot where clear EPW waves were seen. We see that the density of the plasma increases as we approach the axis of the plasma jet, as the EPW peaks are further apart there. (b) shows the line outs from each fiber, with the red trace being on the axis of the plasma.

the electron density, we now will compare these two diagnostics, as shown in Fig. 5.20. Here we see reasonable agreement between the density value between the two measurement techniques. However, the interferometry suggests a wider jet than shown by the EPW feature. This could be either due to scale calibration errors in either of the measurements (though the EPW has error bars to try to account for them) or the fact that, based on post shot realignment, the Thomson scattering laser was not passing through the exact center of the jet, meaning that it would have a shorter path through the jet. For example, using a jet radius of 0.8 mm means that being off the jet axis by 0.5 mm, would cause the jet to appear to have a radius of about 0.65 mm. We also note that in the EPW feature there appears to be a dip in the density of prior to reaching the dense region of the jet.

The other shot that was studied was also a SP shot. The time was 15 ns later in the current pulse, 185 ns. The laser was realigned to ensure it was going

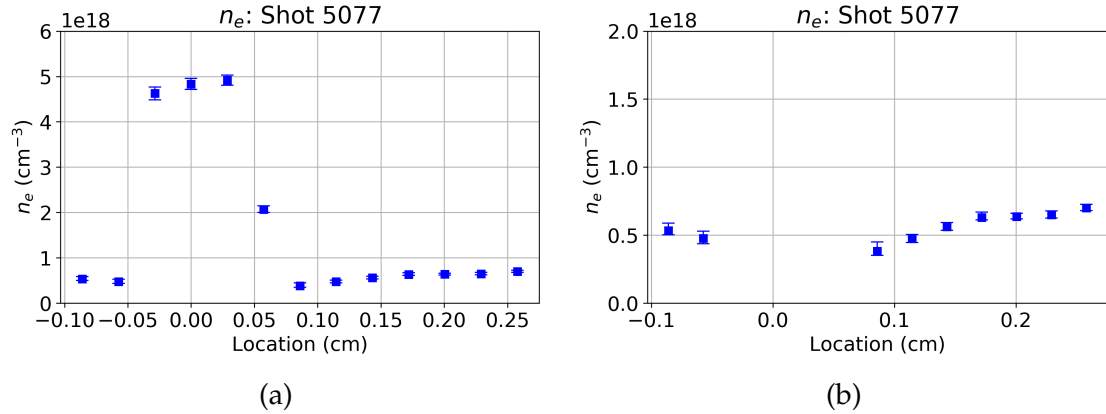


Figure 5.19: Results from fitting the data shown in Fig. 5.18. (b) is just a zoomed in version of (a) to focus on the low-density region. We see on axis, the density of the jet is $5 \times 10^{18} \text{ cm}^{-3}$, while outside of the jet the density is about $6 \times 10^{17} \text{ cm}^{-3}$.

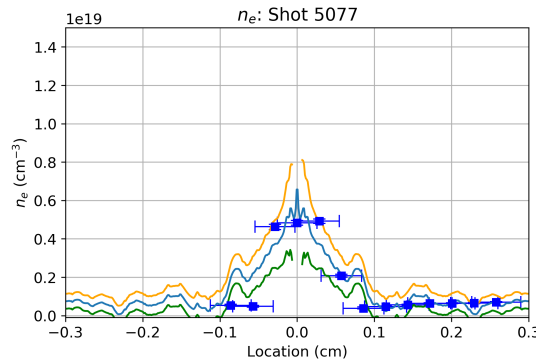


Figure 5.20: Results from both the EPW feature (blue dots) and the interferometry (solid lines). For the interferometry data the blue is the result of the fringe trace and the orange and green traces are the upper and lower error bars from the Abel inversion, which are removed near the axis. This is because Abel inversion struggles near the axis. We see reasonable agreement between the density measurements from the two diagnostic techniques.

through the center of the jet. The raw data is shown in Fig. 5.21, where the peaks are harder to see above the continuum; however, they are there, as shown in Fig. 5.21c. In the jet the peaks appear to be more spread out than the previous shot, suggesting a higher density. In addition, we see an interesting feature on the bottom fiber, where there appear to be two pairs of EPW peaks. An explanation for this is that for that fiber we are collecting scattered light over

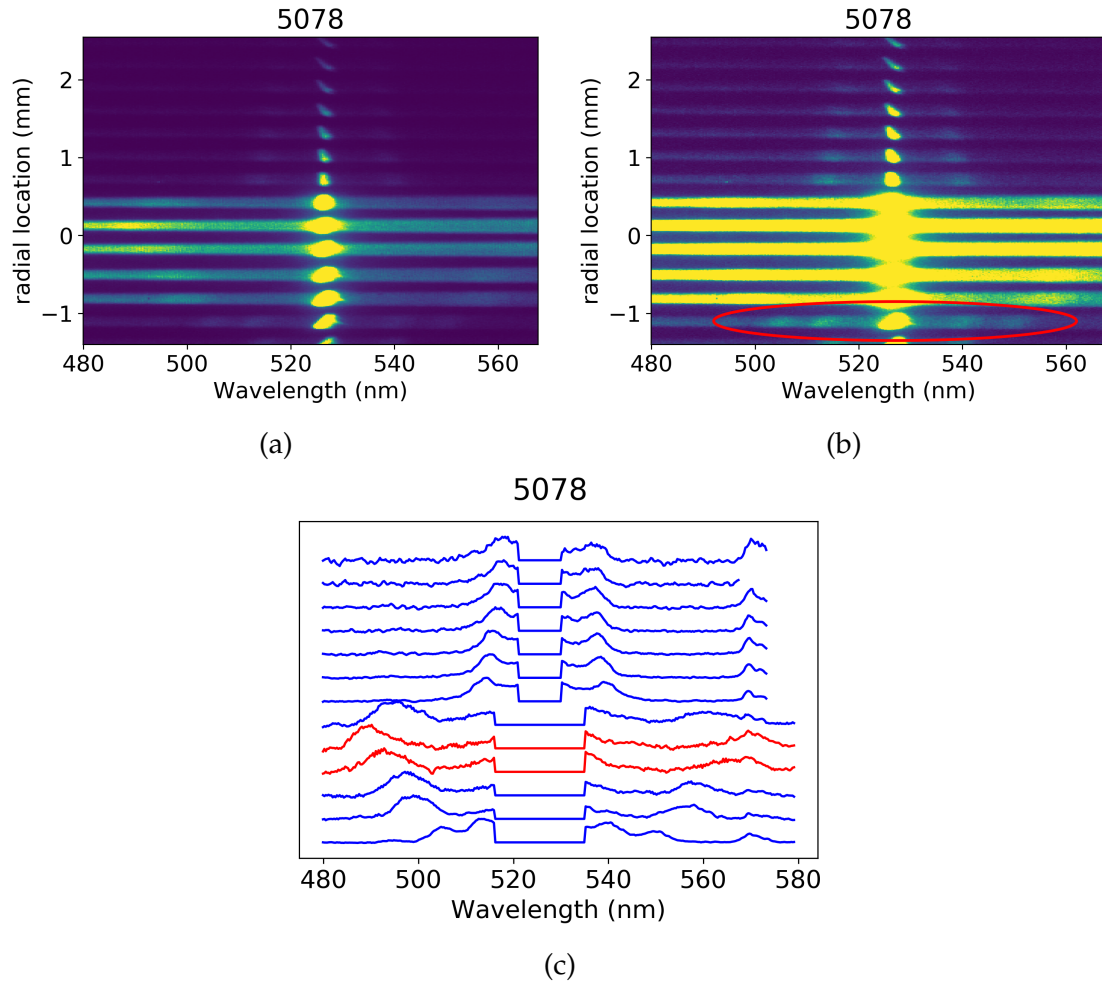


Figure 5.21: (a) shows raw data from a shot that was denser than the previous shot, however, the EPW feature was harder to see. (b) shows the same shot but with the intensity increased to emphasize the fact that one of the fibers appeared to have two sets of EPW peaks. (c) shows the line outs from each fiber, with the axis of the plasma being between the two red traces.

the boundary of the jet. This suggests that the edge of the jet has a very sharp boundary as we can clearly resolve the two peaks, i.e., they are not spread out into one very broad peak. The density measurements are shown in Fig. 5.22, where the fiber with two peaks has two densities.

The comparison to the interferometry measurement is shown in Fig. 5.23. We see from both interferometry and Thomson scattering that the density is cle-

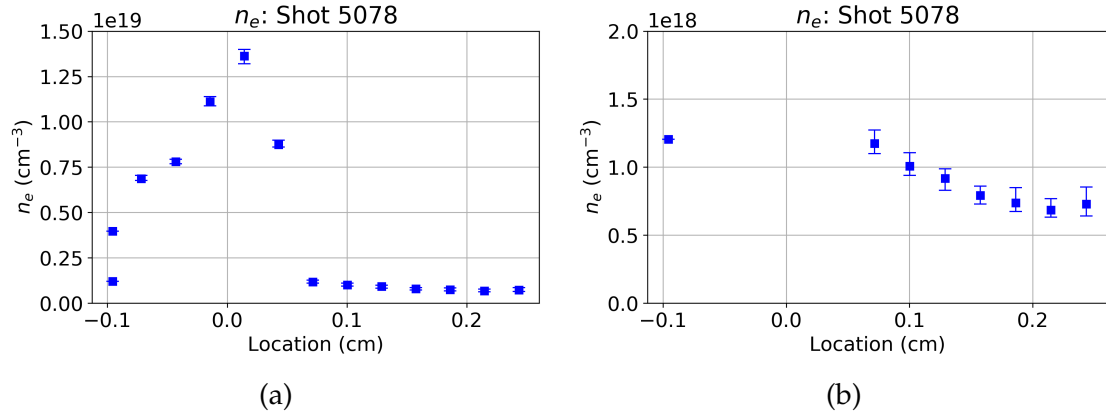


Figure 5.22: Results from fitting the data shown in Fig. 5.21. (b) is just a zoomed in version of (a) to focus on the low-density region. We see on axis, the density of the jet is higher than for shot 5077, over $1 \times 10^{19} \text{ cm}^{-3}$, but outside of the jet the density is still about $5 \times 10^{17} \text{ cm}^{-3}$.

arly higher than the previously discussed shot (shot 5077); however, Thomson scattering suggests a significantly higher density (up to $1.4 \times 10^{19} \text{ cm}^{-3}$) relative to the interferometry (only up to $8 \times 10^{18} \text{ cm}^{-3}$). This discrepancy could be caused by the fact that in this shot it appears that the Thomson scattering laser has already begun to perturb the jet, see Fig. 5.24. This makes making accurate measurements of the density of the plasma from interferometry difficult due to the complex fringe pattern. An additional note is that this shot again suggests differences in the width of the jet between the two different diagnostics. While we are more sure that we are going through the center of the jet, errors in the scaling or the magnification of the two different diagnostic could still be an issue. Further investigation is needed to resolve this discrepancy.

In addition to measuring the density of the plasma, it is also possible to use the EPW feature to measure the electron temperature through primarily a measure of the widths of the peaks. The results of these measurements are shown in Fig. 5.25a. The results from the on-axis streaked IAW feature is shown in Fig. 5.25b. T_e from both the EPW and IAW features was measured to be higher

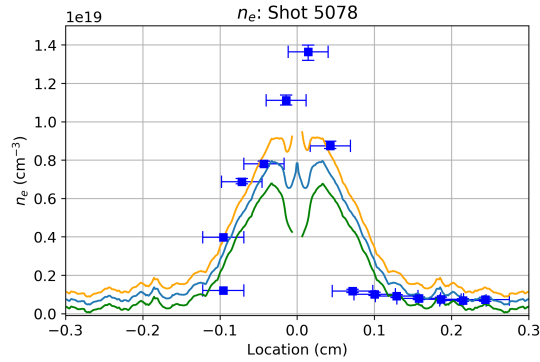


Figure 5.23: Results from both the EPW feature (blue dots) and the interferometry (solid lines). In this shot we see differences in the measured density from the two diagnostics, though both show higher density than shot 5077.

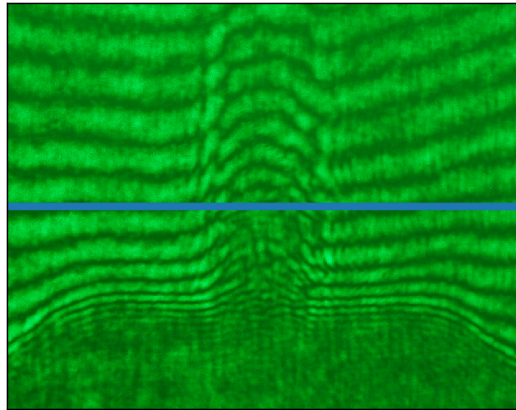


Figure 5.24: The raw interferogram from shot 5078, with the blue line being where we believe the Thomson scattering laser is. We see in this shot that in the region of the laser the fringes are complicated, suggesting that we have already perturbed the plasma, which would cause this diagnostic to be inaccurate.

for shot 5078, which is not surprising due to the higher density. However, for both shots the EPW feature measured a significantly higher temperature than the IAW feature.

There are several key sources of error that could cause either the EPW to overestimate the electron temperature or the IAW to underestimate it. The EPW is susceptible to errors caused by a gradient in the electron density. As discussed earlier, a density gradient would cause the peaks to broaden, and therefore,

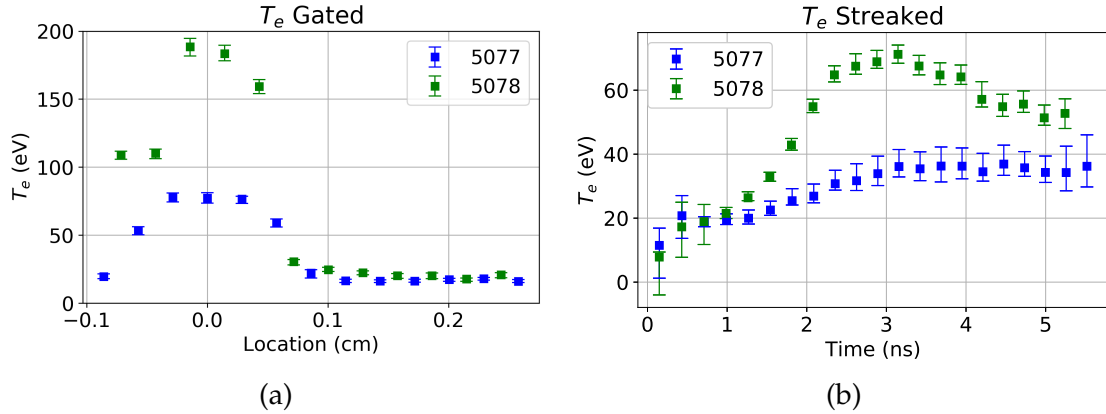


Figure 5.25: Comparison of the measured value for T_e between the EPW feature (a) and the IAW (b). The EPW was from 90° and was recorded on a gated camera. The IAW feature was recorded at 150° from the axis of the plasma jet and was streaked in time. While both diagnostics measured higher temperatures for shot 5078, the EPW spectral feature measured significantly higher temperatures compared to the IAW spectral feature.

cause us to overestimate the electron temperature while simultaneously underestimating the density. This density gradient could be caused by the expanding plasma that is being heated by the laser. Physical effects that could cause us to underestimate the electron temperature from the IAW feature are collisions and the rapid laser heating of the electrons. The latter effect will cause the ionization state to not agree with the NLTE model used for estimating Z . Since the primary EPW error causes an overestimation and the primary IAW errors causes an underestimation, and both of these errors are reasonable expectations in our plasma, the true value for T_e is somewhere between the two measurements.

Another interesting feature of the EPW scattering data is that the red and blue shifted EPW peaks had different relative peak intensities compared to basic Thomson scattering theory. We see in most of the data that the red shifted peak is about 0.7 to 0.8 times the intensity that it should be. This discrepancy between the data and theory is apparent both inside and outside of the jet. One possible cause is instrumental error as the spectrum was flattened by taking the slope

of the continuum radiation. As we are looking over a large wavelength range, the intensity of the continuum radiation will be affected by both the detector's sensitivity and the light emitted from the plasma. While the flattening of the spectrum is a good first order approximation, a more careful calibration that separated both factors could help to remove any instrumental errors. Another possible explanation would be a heat flow in the plasma [35, 36]. Heat flow could slightly modify the electron distribution function and, therefore, change the relative intensities between the two Thomson scattering peaks. Since we are collecting scattering in the $r-\theta$ plane, we would expect any effect from heat flow to decrease the red shifted peak on one side of the jet and the blue shifted peak on the other side of the jet. However, we consistently see that the red shifted peak is relatively weaker than expected, meaning that heat flow is probably not the cause of this discrepancy.

While we have shown that it was possible to collect scattering from the EPW feature, it was still difficult and has not been observed consistently. In addition, it has been tried by others on other plasma loads (S. Rocco with gas puffs) with no luck in seeing the EPW feature near pinch time. There are two major areas of improvement that could lead to more consistent collection of the EPW spectral feature. The first would be to tighten the focus of both the laser and the collection optics. Under the current setup both the laser and the collection fibers are focused down to a diameter of about $250\ \mu\text{m}$ at the center of the chamber. Assuming that the laser and the collection cross section stay matched, the scattered light in a collection volume scales by the focus size while the continuum radiation in the same volume scales by focal size squared. This means that if we decrease the focus diameter down to say like $125\ \mu\text{m}$ we could drop the continuum radiation by a factor of 2. As a note, this may not be as useful

for plasma jets as other loads, as the tighter focus will cause the plasma to heat up more rapidly. As the scattered radiation is polarized, we could also add a polarizer to help reduce the continuum radiation by a factor of 2. Both factors will increase the strength of the EPW feature relative to the continuum radiation. A factor currently preventing improvement of the focus is the size of the vacuum chamber, as we are currently using optics placed right outside of the chamber. Decreasing the focal spot size for both the laser and the fiber will require a lens closer to the plasma, meaning that optics would need to be used inside the chamber, which then would require protection for the optics.

The other major factor that is causing problems for resolving the EPW peaks is filamentation of the laser. If the laser power is above the critical power, then it can be shown to self-focus as it travels through the plasma. The critical power is found to be [48]

$$P_{cr} = 3 \times 10^7 \frac{T_e [\text{keV}]}{n_e/n_{cr}}. \quad (5.7)$$

For our laser $n_{cr} = 4 \times 10^{21} \text{ cm}^{-3}$, and assuming $T_e = 15 \text{ eV}$ and $n_e = 5 \times 10^{18} \text{ cm}^{-3}$, the critical power is 0.36 GW. Since our laser power is 3.3 GW we see that inside the plasma jet we are about a factor of 10 above the critical power, and therefore, are causing the laser to self-focus and filament as it travels through the dense region of the plasma. This filamentation is experimentally verified using a burn card placed on the exit window which shows the plasma significantly disrupts the incoming beam. While this will affect both the IAW and the EPW feature, we are primarily concerned about the amount of light lost from the collection optics focal volume by the filamentation and its effect on viewing the EPW feature. Going to lower power could avoid the filamentation, but as discussed above, we are already battling radiation from the continuum so cannot reasonably go down a factor of 10 in laser energy. One solution to this is to use a distributed

phase plate (DPP) which increases the critical power by a factor of around 100. This would allow using our current laser energy of 10 J without filamentation. At the time of this writing, discussions were in process with LLE for the help in the design and acquisition of a DPP, and so this will be an improvement to the system in the near future.

5.5 Current Polarity Effects

One of the primary physics interests of this work was to help validate PERSEUS simulations that showed differences in the plasma jet based on the direction of current through the foil. Though, as will be discussed, previous research has been done comparing the structure and density of the plasma jets, the electron temperature has not been studied in detail. By using an experimental arrangement that avoided laser perturbation, while still collecting a significant amount of light, we have been able to measure an unperturbed electron temperature, enabling comparison and improvements to the simulation.

5.5.1 Experimental Results

One noticeable difference between the two current polarities was the degree of laser heating of the plasma jets. A comparison of typical results from shots with 10 J of laser energy is shown in Fig. 5.26a for data at 180 ns into the current pulse and in Fig. 5.26b for data at 120 ns. Though all shots start out around 20 eV, the experiments at 180 ns heat up to 65 eV in RP and 45 eV in SP, while the shots at 120 ns have the RP shot heating to 50 eV and the SP shot heating only to

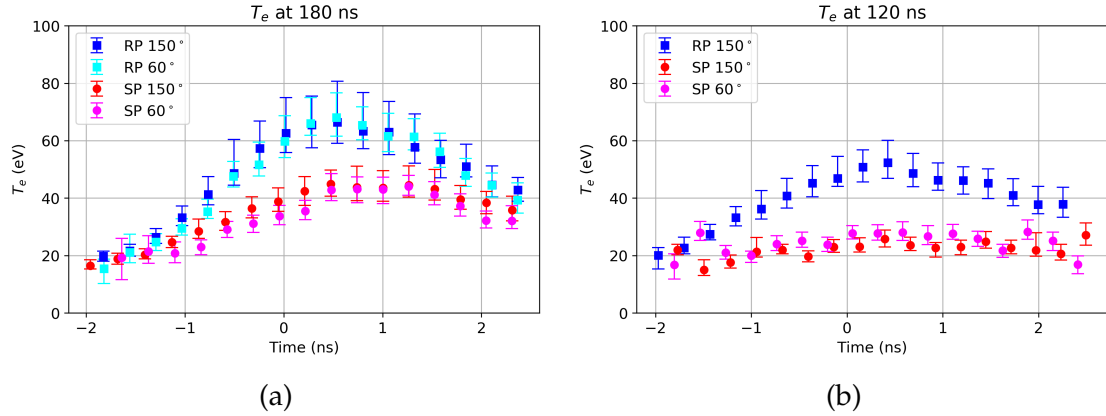


Figure 5.26: Comparison between T_e vs. time for standard and reverse polarity from Thomson scattering for shots centered at 180 ns (a) and 120 ns (b) into the current pulse. We see that the shots at 180 ns heat more than the shots at 120 ns and that at both times the jet in RP is heated more. In addition, we see relatively good agreement between the measured T_e from the two different scattering angles.

25 eV. Therefore, in both cases we see that the jet formed from RP appears to heat up more than the SP jet, suggesting differences in the amount of absorbed laser energy between the two plasma jets. Since the absorbed laser energy scales $Zn_e^2/T_e^{3/2}$, we expect the RP jets to be denser than SP jets. Looking at the results from the interferometry for these shots, Fig. 5.27, we can clearly see that the RP jets are more dense at both experimental times, which is in agreement with the scaling of the laser heating.

One other interesting thing is that, though the late time SP shot appears to be denser than the early time RP shot, it appears to heat less than the RP shot. While these experiments do occur at different times, the primary factors in determining the heating are T_e and n_e . Since the starting temperature appears to be similar, it could suggest that there are other important differences than just the density between the SP jet at 180 ns and the RP jet at 120 ns. Things to look at would be the ionization state and the upward velocity. However, more data would be needed to test for these differences.

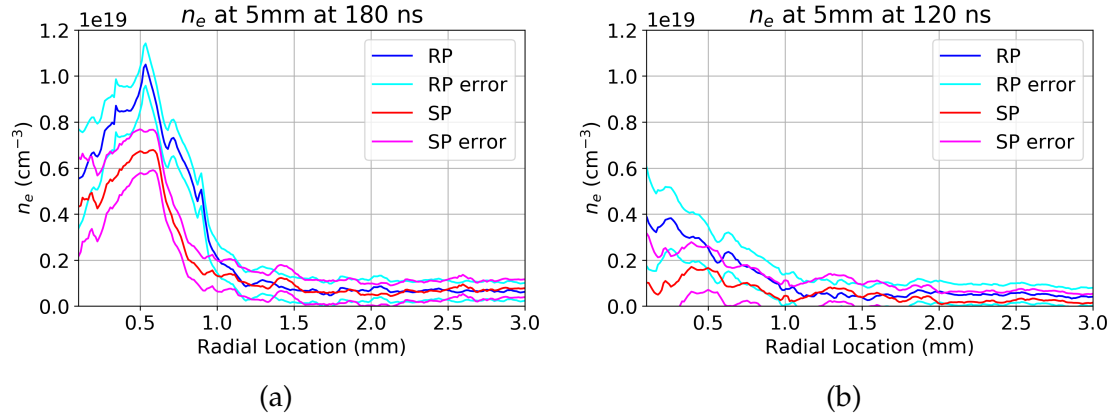


Figure 5.27: Results of the density from interferometry measurements for the same shots as shown in Fig. 5.26. We see that RP jets are denser than SP jets and that the density increases as time progresses. This density difference agrees with the difference we see in the heating of the jets. The cyan and magenta colors represent the error bars on the Abel inversion for the interferometry.

The density results can also be compared to earlier research that looked at plasma jets created from thinner foils ($5 \mu\text{m}$) and smaller diameter pins (1 mm) [30]. Even with these experimental differences, these experiments showed similar density trends as RP jets were denser than SP jets. One key difference between the earlier experiments and those reported here is that we found the RP jets to be wider than SP jets, which is opposite to the earlier research. This, however, could be due to the significant differences between the thickness of the foil as well as the pin size.

Though seeing the density differences using the amount of heating from the Thomson scattering laser is a good confirmation of earlier density measurements, the big advantage of the Thomson scattering diagnostic is that it enables accurate measurement of the temperature of the plasma if the plasma is not perturbed by the laser. To reduce the perturbation from the laser a significantly lower energy needs to be used than previous shots that clearly showed heating at 2.5 J. Previous work had shown some data at 1 J, however the SNR was not

great, and it was desired to try to go to even lower laser energies. This meant that more effective collection of light was needed throughout the entire system. While the collection optics between the load and the fiber had already been improved by using an achromatic doublet system, little work had been done in improving the coupling between the fibers and the spectrometer. This was clearly an issue as the fibers were $f/5$, while the spectrometer was $f/10$, meaning we were losing about $3/4$ of the light. By sacrificing some spectral resolution, the fiber could be coupled into the spectrometer using a 2:1 magnification, see Fig. 5.28, in order to couple all of the light into the spectrometer. As will be shown, this improvement enabled the recording of the IAW feature when only 0.5 J of laser energy was used.

In addition, a 200 μm acupuncture needle was used for alignment for each shot. The alignment was performed before loading the foil by mounting the needle on the center pin at the center of the load. The fiber bundle position was then adjusted to maximize the collected reflected light off this needle. By taking a picture of this needle on the shadowgraphy channels and comparing its location to that of the jet, we found that the center of the jet is normally within 100 μm of where we aligned the laser. This means that our scattering volume includes the center of the jet.

The results from these improvements are shown for 0.5 J in Fig. 5.29a and for 1 J in Fig. 5.29b. The first thing that is apparent is that T_e is about 15 eV for both current polarities. As T_e is consistent throughout the 0.5 J and 1 J shots, and does not change based on laser energy, we conclude that we are no longer in a region of detectable laser heating for 0.5 J of laser energy, and this may also be true for 1 J. This means that we can be relatively confident that the measured

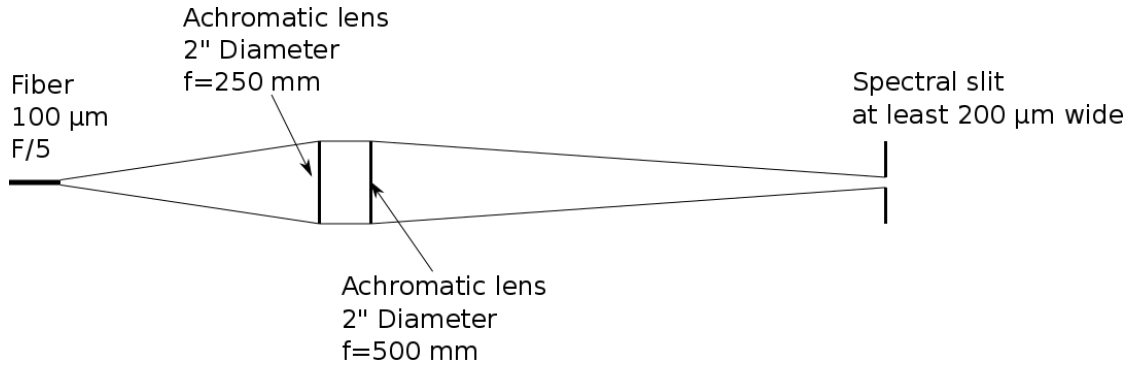


Figure 5.28: Schematic of the coupling system used to improve the coupling between the fiber bundle and the spectrometer in order to match the f-numbers. This setup significantly improves the light collection. However, it decreases the spectral resolution as the slit width is $200\ \mu\text{m}$ instead of $100\ \mu\text{m}$.

value of $15\ \text{eV}$ for T_e is the unperturbed temperature. We note that there is some variation in the measured T_e that is outside of the MC error bars, which is due to the challenges of fitting these low temperature IAW features as the two peaks are relatively close together. These variations though, are within the maximum possible range we expect for T_e discussed in the next section. If, however, we increase the laser energy to $2.5\ \text{J}$, see Fig. 5.30, we see that at least RP shots have clear heating, in agreement with previously discussed data. Figure 5.31 summarizes the data so far discussed in this section, by showing the T_e measurements if we bin in time the entire streak signal, effectively treating it as a gated camera with a $10\ \text{ns}$ gate width. We see that at low laser energies T_e agrees between RP and SP jets, but then, as the laser energy increases, T_e increases more rapidly for RP jets than for SP jets.

5.5.2 Comparison with Simulations

To compare the experimental T_e to the simulations, we will take results from a bin in time of the entire streak signal, effectively treating it as a gated camera,

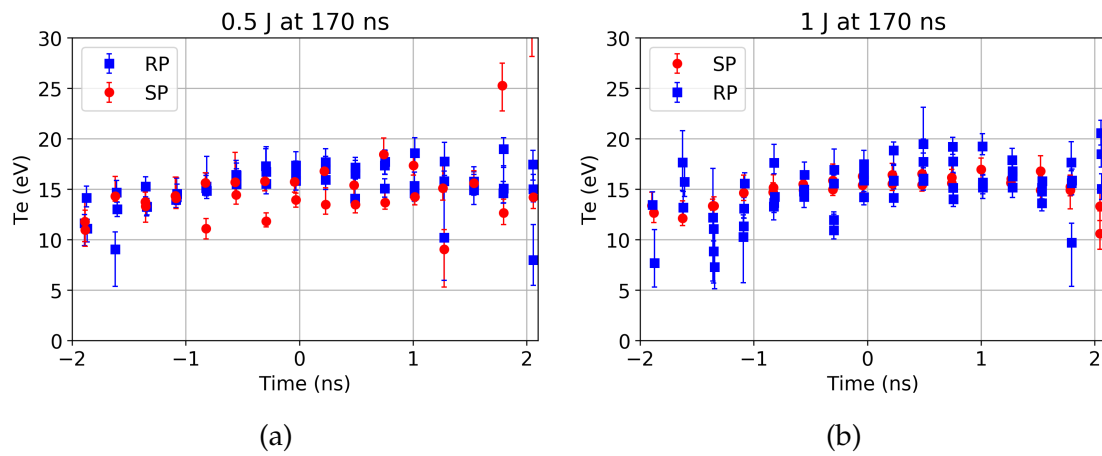


Figure 5.29: Results from T_e measurements with either 0.5 J (a) or 1 J (b) of laser energy for both current polarities. RP shots are shown in blue and SP shots are in red. Since the temperature is relatively constant throughout the laser pulse and the temperature is similar between the two laser energies, we are no longer in a region where the laser affects the measured value for T_e . We see that T_e is similar between the two jets and is about 15 eV.

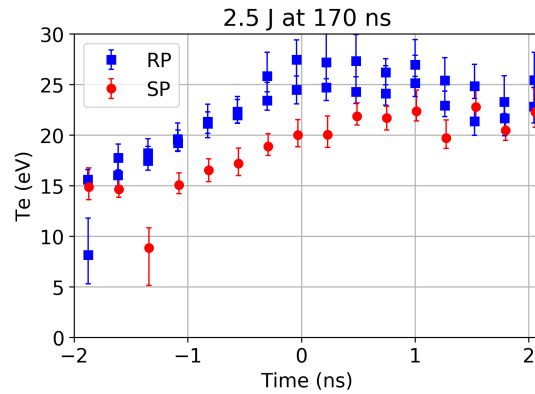


Figure 5.30: Results from T_e measurements with 2.5 J of laser energy for both current polarities. We see in this case we are heating the jet, and that the RP jets heat up more than the SP jet, which agrees with previous results.

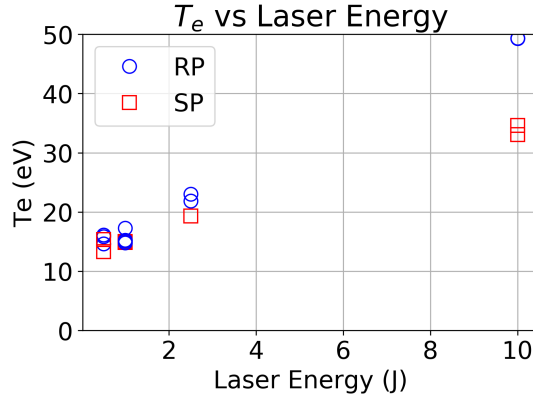


Figure 5.31: T_e measurements from an bin in time of the entire streak signal as a function of laser energy. We see for low laser energies the temperature of the two jets is very similar. As the laser energy increases both jets begin to heat up, but RP jets heat up more.

for the 0.5 J and 1 J experiments, as we have shown T_e to be constant throughout the laser pulse. Instead of using the MC error bars that have been used for the rest of the data, we will estimate the error bars using the possible range for T_e method (discussed in Sec. 3.5.3) to try to account for all possible sources of error, such as density, collisions, and T_i . Figure 5.32 shows these results, which gives us an experimental range for T_e to be between 7 and 23 eV, with the base model (which used $T_i = T_e$ and $n_e = 7 \times 10^{18} \text{ cm}^{-3}$) giving 15 eV. This range is larger than experimentally expected error as it tries to maximize the contribution of any possible error source, and therefore, we are confident that the true value for T_e is comfortably within this range

These electron temperature measurements of the plasma jet were compared to two different computational methods for PERSEUS simulations [63, 46]. The first method is finite volume (FV) which was discussed in Sec. 4.2. Full 2D images of n_e and T_e at 170 ns are shown in Fig. 5.33, and line outs from 5 mm above the foil with a comparison to the experimental data are shown in Fig. 5.34. Comparing T_e between the experiments and simulations, we see that

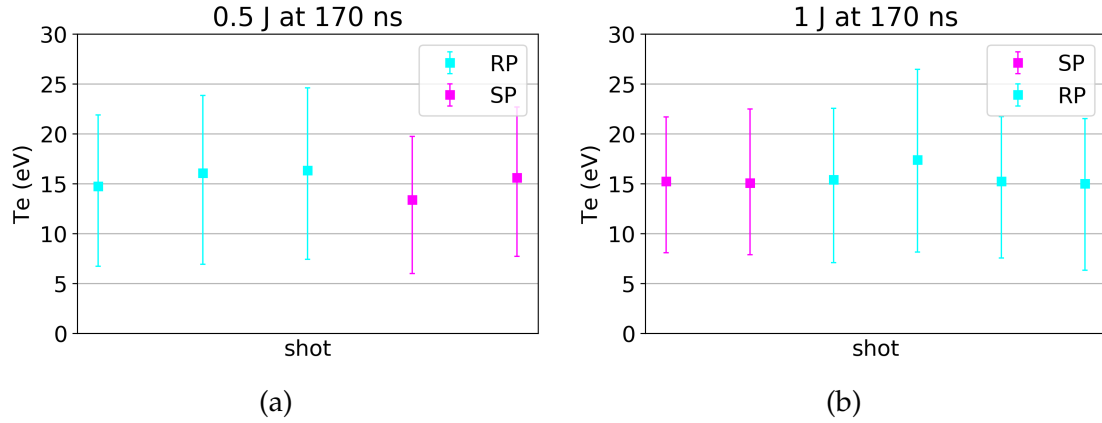


Figure 5.32: T_e measurements from time integrated streaked signals for 0.5 J (a) and 1 J (b). This data does not use the MC method for the error bar calculation, but instead tries to find the maximum and minimum possible value for T_e within a reasonable range of fitting methods.

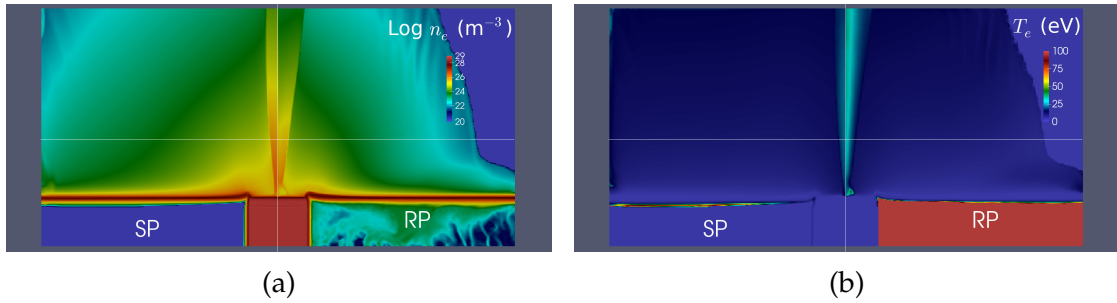


Figure 5.33: (a) shows n_e and (b) shows T_e for FV simulations of the two jets at 170 ns into the current pulse, with SP on the left and RP on the right. We clearly see in these simulations the RP jet is hotter and wider than the SP jet. The horizontal line is 5 mm above the pin, where we aligned the Thomson scattering laser.

the simulation suggests somewhat higher temperatures (22-29 eV) compared to the experiments (7-23 eV) and shows T_e to be higher in RP jets, which was not seen in experiments. While we see that the jet widths agree between the simulations and the experiments, the simulations suggest both types of jets to be significantly denser than the experiments. In addition, simulations find SP jets to be denser than RP jets, which is the opposite of what the experiments show.

In addition to the FV simulations, we also compared experimental data to

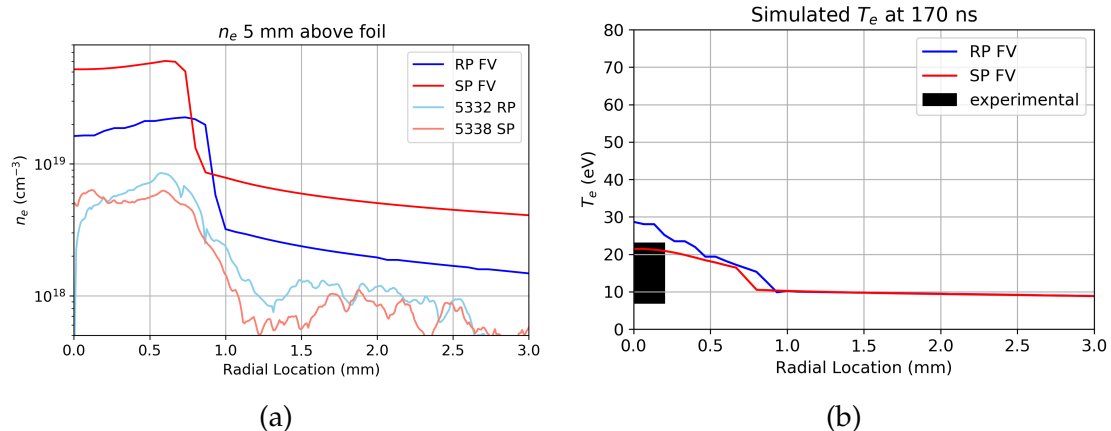


Figure 5.34: Plots comparing experiments and FV simulation at 170 ns and 5 mm above the pin with n_e in (a) and T_e in (b). We see that the jet widths are in good agreement, T_e is slightly higher in the simulations, and n_e is much higher in the simulations.

DG simulations. As discussed in Sec. 4.2, DG simulations were significantly higher resolution, less numerically diffusive, and included a more accurate model of EOS effects than FV simulations, however, at the cost of computational time and only having a single temperature. The 2D results are shown in Fig. 5.35 and line outs 5 mm above the foil are shown in Fig. 5.36, again at 170 ns. While near the axis of the plasma jet the temperature is significantly higher than what experiments or the FV simulations suggest (60-70 eV), looking about 300 μm off of the axis of the jet, but still in the jet region, suggests a temperature of only 20 eV which would be comparable to the experimental data. In addition, we note that the simulations now show significant differences in the widths of the jets, where the RP jet has expanded to be much wider than the experiments, while the SP jet is narrower than the experiments. Like the FV simulations, these simulations suggest significantly higher densities than the experiments, and that the SP jets are denser than RP jets.

Having seen how each simulation individually compares to the experiments,

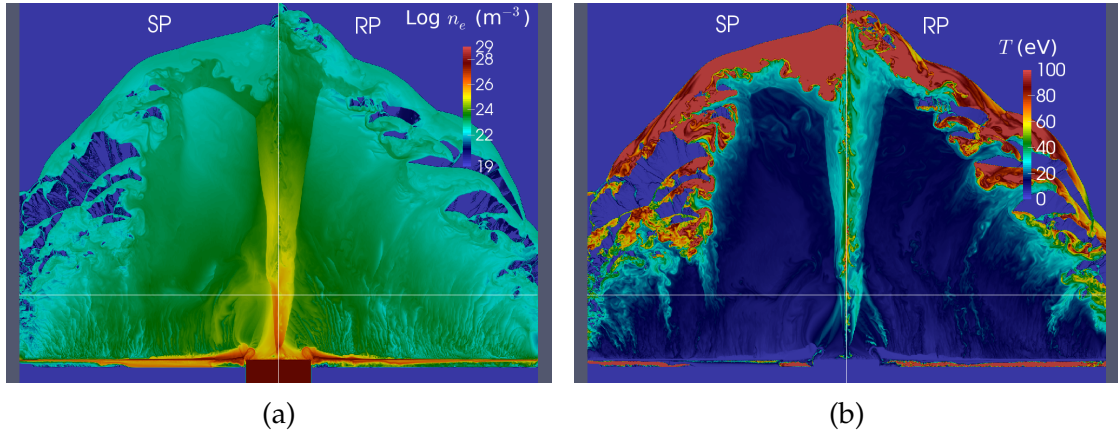


Figure 5.35: (a) Shows n_e and (b) shows T for the two jets at 170 ns into the current pulse from DG simulations, with SP on the left and RP on the right. We clearly see in these simulations that the RP jet is wider than the SP jet. The horizontal line is 5 mm above the pin, where we aligned the Thomson scattering laser.

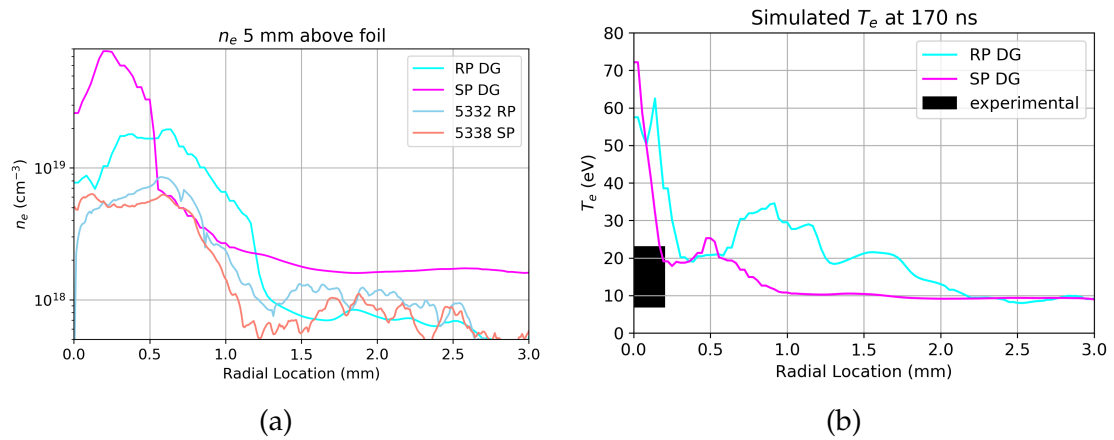


Figure 5.36: Plots comparing experiments and DG simulations at 170 ns and 5 mm above the pin with n_e in (a) and T in (b). We see jet widths, densities, and on-axis temperatures disagree between the simulations and experiments.

Fig. 5.37 now compares both simulations and the experiment simultaneously to get a better picture of what is happening in our plasma. Comparing the on-axis temperature of the jet between the two simulations, we see that the DG simulations significantly overestimates T_e . While the FV simulations are closer to the experiments, they are still an overestimation. Having T_e slightly higher in the simulations could be explained by a lack of a radiation model, as radiation

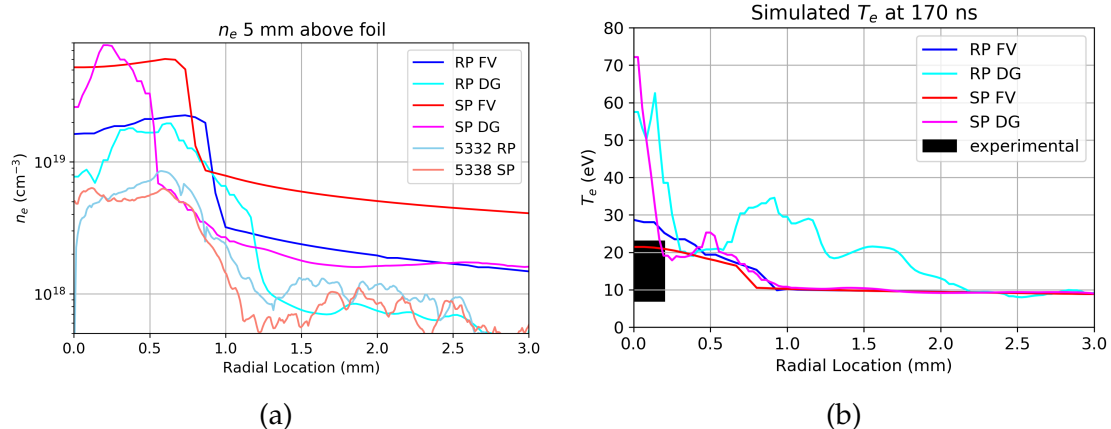


Figure 5.37: Plots comparing experiments, FV simulations, and DG simulations at 170 ns and 5 mm above the pin with n_e in (a) and T in (b). These results were shown separately in Fig. 5.34 and Fig. 5.36 but are repeated here for easy comparison between the two different simulation techniques.

cools plasma. However, incorporating a line radiation model in PERUSES based on a radiation model used in GORGON code at Imperial College [65] showed only very minor modifications to the plasma parameters. The DG simulations T_e discrepancy is much larger and likely could not be explained by radiation. As our scattering volume is comparable to, or even smaller than, the simulated hot region, and we have never experimentally seen temperatures this high, we doubt that the DG on-axis temperature is accurate for our plasmas. If we look at the density profile, we see that while both simulation methods overestimate the density in the jet, at least the FV simulations tend to match the widths of the jets, while the DG simulations do not. Therefore, it appears that the FV simulations captures the physics of our plasma jets better than the DG simulations.

The fact that the FV model appears to be better for our plasmas is interesting as one would normally think the DG method would be a better model. This is because DG simulations include most of the physics from the FV model, other than only having a single temperature, and have more accurate ionization, resis-

tivity, and transport models. In addition, the DG simulations shown have significantly higher resolution (28 vs 67 μm) and are much less numerically diffusive. There are two key areas that could be causing the DG to be less accurate than the FV model, the numerical diffusion and the single temperature. The single temperature could be causing issues if the electrons and ions are at significantly different temperatures. While FV simulations around peak current do show T_i to be 3-4 times higher than T_e , the temperatures from the DG simulations are even higher than that. Since we would expect the two-temperature model to put rough bounds on T for the single temperature model, we do not believe this is the primary reason for the high temperatures in the DG simulations.

The other possible cause for the discrepancy is numerical diffusion. The FV method can effectively capture some physical diffusion in the numerical diffusion inherent to that method, even though it does not physically model the diffusion. The DG method, as it is not numerically diffusive, is not able to capture physical diffusion that is not explicitly part of the code. Lack of diffusion being an issue is supported by the fact that DG simulations suggest more structure than these or other recent experiments seem to show. A possible source of this diffusion would be resistive diffusion. We believe that this is the primary issue with the DG code, and if so, then by identifying the physical sources of diffusion, and finding a way to account for them, the DG code may be able to create a more accurate picture of the plasma.

Since the FV model currently seems to be our best match to the data, we will now discuss possible sources of errors between this simulation and the experiments. The most obvious discrepancy is that the FV simulations suggest a higher density than the experiments, and that the current polarity with the den-

ser jet is opposite that of experiments. A possible reason for this discrepancy is the fact that plasma jets from radial foil loads are very challenging to simulate, primarily due to the sources of the $B_\theta J_r$ force that is important for jet formation. The J_r comes from the current flowing through the foil, and B_θ comes from the current within the pin. This magnetic field, therefore, must diffuse through the foil in order to be in the region above the foil and affect the formation of the plasma jet, which is challenging to model. Additional difficulties come from the fact that we do not resolve the foil or handle the initial phase transitions during the FV simulations, which could cause errors in the amount or rate of ablated plasma that is able to be swept up into the plasma jet region. These possible errors could result in differences in the amount of plasma being available to form the jet between the experiments and the simulations.

In a comparison of the widths of the jets, the simulations show the SP jets to be narrower but denser than RP jets, while experiments show SP jets to be narrower but less dense. If one can assume that a comparable amount of plasma is swept into the jet region, the more compressed (smaller radius) jet would have a higher density, which the simulations find but the experiments do not. As already mentioned, earlier experiments, which had a smaller pin and a thinner foil, showed RP jets to be narrower but also denser, which agrees with this assumption [30]. This means, for our current experiments, some physics must be causing more plasma to be available for RP jets. An explanation is XMHD effects, such as the Hall effect, affecting the amount of ablated plasma from the foil. The Hall effect can be very strong just above the foil and could lead to these results. Simulations failing to capture this can be explained by lack of resolution and not handling the initial phase transitions, as the region we are most interested in for this effect is just above the solid foil and likely relatively thin.

In addition to these density discrepancies, we also want to look more closely at the temperature between the FV simulations and the experiments. We see that the simulations overestimate the electron temperature. As already discussed, one cause of this is that the simulations do not include radiation, which would cool the plasma slightly. We also note that in general that higher density corresponds with lower temperatures, which can be seen in the DG simulations, Fig. 5.35, where T_e decreases as n_e increases. This is important, as the simulations have both a significantly higher density and a slightly higher temperature. This means that too much energy in the simulations is going into the jet region of the plasma. Therefore, when improving the FV simulations, we would want to look for physical mechanisms that would lower the density of the plasma without significantly changing the temperature or shape of the jet.

Overall, while we do not have a match between the simulations and experiments, comparison between the two have provided useful insights. We have shown that XMHD effects are important to our plasmas as both the density and width of the jet are affected by the direction of current flow, though not the electron temperature. These comparisons with simulations also suggest primary areas for improvement for future simulation work, which include accounting for physical diffusion in the DG model and accurately handling the early time plasma formation and magnetic diffusion. In addition, accounting for other effects could also improve the simulations. Some of the other primary areas of interest for code expansion include: radiation, ionization model, and 3D simulations.

CHAPTER 6

CONCLUSION

6.1 Conclusion

This thesis discussed the development of a Thomson scattering system and its use to study plasma jets formed on the COBRA (COrnell Beam Research Accelerator) pulsed power machine. While collective Thomson scattering is a very powerful diagnostic, it has been used rarely in pulsed-power-driven plasmas. This research focused on expanding our Thomson scattering diagnostic in order to get more information about the plasma and on developing a code base for analyzing the Thomson scattering spectra. This included recording Thomson scattering spectra as a function of time with a streak camera and recording the electron plasma wave (EPW) feature as a function of radius with a time-gated camera. By using a streak camera, we have been able to study the time evolution over a span of at least 3 ns. This was useful in the experiments to study the laser perturbation of the plasma, and has also been useful for pinch time measurements in gas puff z-pinch experiments (thesis research of S. Rocco) [56, 55]. The EPW feature enables measurement of the electron density but is harder to observe as it is significantly weaker than the ion acoustic wave (IAW) feature. While some effort is still needed to ensure that the EPW is recorded reliably, we have seen promising initial results from the EPW feature.

These developments in the Thomson scattering diagnostic were performed on plasma jets created from radial foils, which had interesting physics questions to address in addition to providing a good test bed for diagnostic development. The first area explored on radial foils was the azimuthal velocity in jets expo-

sed to an external axial magnetic field, which was discussed in Sec. 5.1. This rotation is due to the $B_z J_r$ force created by this magnetic field. We were able to successfully record the rotation near and inside the dense region of the plasma jet, and found it to be about 20 km/s. The direction of rotation also agreed with the direction of $B_z J_r$ and changed directions if either B_z or J_r changed sign. We compared the experimental velocity along all 3 axes to PERSEUS (Plasma as an Extended-MHD Relaxation System using an Efficient Upwind Scheme) simulations and saw reasonable agreement both outside and in the dense region of the jet. Simulations, however, seemed to suggest that the hollow center of the jet would have much higher axial and azimuthal velocities than seen in experiments. This discrepancy could be due to not having enough scattering from the low-density plasma in that region to see it over the nearby slower moving denser plasma.

We also explored a limit to the capabilities of the Thomson scattering diagnostic in Secs. 5.2 and 5.3. Here we showed that for our plasma jets the Thomson scattering laser had sufficient energy to heat the plasma by inverse bremsstrahlung, as the absorbed laser energy density was about 10 times that of the unperturbed plasma jet. While this was shown to affect the measured electron temperatures, it did not affect the measured velocity. Using a streak camera, the time resolved laser heating was recorded and showed the plasma jets to heat from 20 eV up to about 80 eV before cooling at the end of the laser pulse. This cooling was shown to be due to expansion caused by the laser heating of the plasma. We also explored the heating of Ti jets in Sec. 5.3.1. We showed Ti jets to heat more than Al jets from the Thomson scattering laser, likely due to the higher value for Z in Ti. The Ti jets also showed sharp Thomson scattering features early within the laser pulse that were not seen in Al jets. Though they were

in the spectral region of IAW features, their sharpness and relatively short life spans could suggest that they resulted from scattering off of some other wave or feature of the plasma.

Section 5.4 explores the results from two different techniques to measure the electron density. The first method tried to use a sensitivity to scattering angle in the IAW formula to measure the density by comparing the results from two different angles. We showed that there is a band of density and temperatures that this method can work. Our plasma did not fall in this band, so it was not able to provide more than a lower-limit of $2 \times 10^{18} \text{ cm}^{-3}$ in the plasma density. We also used the EPW scattering feature to measure the electron density. While this method has not been able to record analyzable scattered spectra consistently, we did obtain a few shots with useful spectra on them. These shots showed a plasma density between 5×10^{18} and $1 \times 10^{19} \text{ cm}^{-3}$. They also showed that the EPW feature (80-200 eV) measured higher electron temperatures than the IAW feature (30-70 eV), and, because of the primary causes of errors in the measurements using the two features, the two measurements bound the true temperature.

Finally, in Sec. 5.5 we compared results from experiments under different current polarities. These experiments used a range of laser energies to measure both perturbed and unperturbed plasma. We found that the reverse polarity (RP) jets, those with a radial outward current flow, heated up more at higher laser energies due to the higher densities of the jets. Lower laser energies showed that the two plasma jets had similar pre-laser-perturbation temperatures, about 15 eV.

These results were also compared to both finite volume (FV) and discontinuous Galerkin (DG) simulations in PERSEUS. We found that in general the FV

method compared better to experiments than the DG method, which we suggest it is due to the numerical diffusion in the FV method capturing some physical diffusion that is not captured in the non-diffusive DG method. The primary disagreement between experiments and FV simulation is that the simulations have significantly higher densities. We suggested that this disagreement could be due to either challenges in modeling the diffusion of the magnetic field through the foil or that the foil is not resolved. Comparisons like these are key to both improving simulation models and understanding experiments. They have contributed to improving our understanding of the physics we are trying to study.

6.2 Next Steps

6.2.1 Thomson Scattering Development

While this thesis research has laid the foundation for Thomson scattering to be a routine diagnostic on COBRA experiments, there are still several key areas of improvement that should be made for Thomson scattering to be an even more robust diagnostic. The first major improvements would be for more reliable recording of the EPW feature, which was discussed in detail at the end of Sec. 5.4.2 but will be summarized here for completeness. This would include adding a distributed phase plate (DPP) to the optical path between the laser and the final focusing lens, which would allow the Thomson scattering laser to operate at maximum energy within most of our plasmas without filamenting. The signal from the EPW can also be improved by collecting from a smaller scattering volume. This would require decreasing the focal spot of the Thomson scatte-

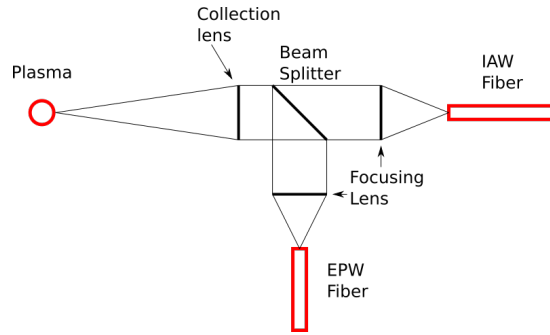


Figure 6.1: A possible setup to collect IAW and EPW spectral features from the same scattering volume. Using a beam splitter enables both spectral features to be recorded from the same line of sight. Each fiber takes the light to a different spectrometer.

ring laser and the fiber's collection volume, which would increase the amount of signal delivered to the spectrometer relative to the continuum.

If the EPW and IAW spectral feature could be both recorded routinely, then it would be possible to record spectra from the same scattering volume for both features, as shown in Fig. 6.1, giving a more complete picture of the plasma conditions. A similar setup could be done with a single fiber bundle from the load to the spectrometers and then a beam splitter between the fiber and the spectrometers. This would have the advantage of avoiding errors in aligning the two fibers with the load. However, in our lab there is limited space on the spectrometer table, so it would be more difficult than splitting the beam on the load side (Fig. 6.1). Having the EPW feature will give n_e of the plasma, which can be used to help improve the T_e measurements from the IAW, which could be further compared to T_e measured by the EPW feature. If the plasma was in a state that it could be well modeled by basic Thomson scattering theory (Maxwellian, non-collisional, and small gradients), we would have a good measure for Z of the plasma without having to base it on an outside table such as was done here with FLYCHK tables.

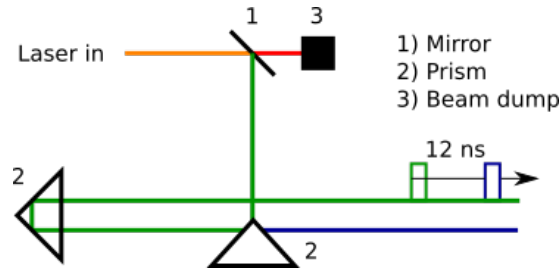


Figure 6.2: Figure demonstrating how we could split the beam into two pulses without wasting half of the laser energy. The first prism splits the beam in half, while the second prism acts as a retro reflector. This may have issues at focus as the beam profile is no longer circular, but would allow most of the laser energy to propagate along a nearly collinear path. To expand this system to enable 4 pulses, another pair of prisms would be needed, this time with the laser coming out of the page, which would split the laser into quarters.

While we presented in this thesis a setup to record two Thomson scattering pulses both with a laser energy of 2.5 J, plans have been discussed to try to take advantage of the full laser energy, enabling scattering of either two pulses at 5 J or four pulses at 2.5 J, as shown in Fig. 6.2. These setups use the full beam energy at the cost of degrading the quality of the beam by splitting it either in half or into quarters. This would enable the recording over a period of about 12 ns as one continuous pulse or spread out over time with gaps between the pulses. We believe that the sacrifice in beam quality is worth the extra energy, but tests would be needed to confirm this design. We also note, based on the latest improvements to the collection systems, that for at least some plasmas 1.25 J of laser energy is enough to get analyzable signal-to-noise ratio (SNR). Therefore, basically repeating the process used in this research one more time results in four beams all at 1.25 J with a non-degraded beam quality, as shown in Fig. 6.3. Either of these setups could be very useful to study plasmas that may be changing conditions over 12 ns, but are spatially in the same place, such as a z-pinch at pinch time, or only moving through the collection volume of a single fiber on that time scale.

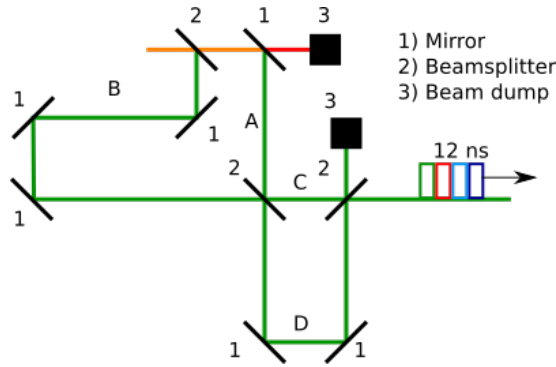


Figure 6.3: A setup that could be used to collect scattering from 4 pulses each at 1.25 J of laser energy. This setup has less energy than Fig. 6.2, but does not disrupt the shape of the beam. There would be 4 paths: AC, AD, BC and BD. A possible setup for this would be to make B 6 ns longer than A and D 3 ns longer than C to get a continuous 12 ns pulse.

In addition to the experimental side of the diagnostic, there can also be improvements to the analysis techniques of the plasma. For the research done here we focused primarily on non-collisional Maxwellian Thomson scattering, and briefly explored the effects of a super Gaussian electron distribution. However, there were clearly other effects on the IAW profiles, such as collisions, and we just accounted for them by using an extra Gaussian profile. By including a full collisional model [60], it would be possible to better understand the finer details of our Thomson scattering profiles. This would especially be important if research was continued in the plasma parameter range of this thesis, where collisions clearly affect the scattering spectrum. Even if the model does not run fast enough to be run on all the data, it would help to explain and track errors introduced by using a collisionless model. In addition, the effect of using an electron distribution function other than a Maxwellian could be done using the code discussed in Appendix B.

6.2.2 Thomson Scattering on Plasma Jets

There are also several areas of using Thomson scattering on plasma jets that could be explored in future research. Some exploration would be enabled by the advances discussed in the previous section, mainly by having a higher SNR with the EPW scattering feature, which would give more reliable information about the plasma. For example, it would be interesting to see the results from the EPW feature streaked in time, showing how the density of the plasma changes as it is heated by the laser. Going even further, streaking both the IAW and EPW features from the same scattering volume would give a very good picture of how the plasma jet changes as it is heated by the laser.

In addition, a wider area of the plasma jet could be explored, as these experiments were limited to 5 mm above the surface of the foil. By changing the height of the scattering volume above the pin, it would be possible to get a better map of plasma parameters in order to compare to simulations. In addition, since we now see experimentally that 0.5 J is low enough energy to not perturb the jet, these results could be recorded using multiple fibers on a gated camera, creating a rough 2D map of T_e for the plasma jet. This currently would have to be done over multiple shots, so only a limited number of heights could be explored, but it would still provide useful information for comparison to simulations. It may even be possible to do this in a single shot if the laser is focused into a plane along the axial direction with a cylindrical lens, and a fiber bundle is used that has a grid of fibers instead of a linear array.

Taking advantage of unperturbed jets from low laser intensity, it could also be useful to study other configurations, such as magnetized plasma jets, to make unperturbed measurements of the T_e in addition to the measurements of v_θ re-

ported here. These magnetized jets show drastic differences based on the current polarity and it would be very interesting to have data to compare to PERSEUS simulations to see if there are significant temperature differences between RP and SP jets when there is an applied magnetic field.

Thomson scattering could also be used to continue to explore differences between plasma jets formed from various material foils. We showed in this thesis that the plasma formed from Ti and Al jets had significant differences in the amount of heating and that the Ti jets had very interesting sharp features in their scattering profiles. Identifying the root cause of these sharp features could lead to better understanding of Thomson scattering theory, of the properties of the jet, or both. Experiments could study different material foils, different scattering angles, and different laser energies, to see when and where the sharp features form in the scattering spectra.

Overall, while plasma jets did serve as a good test bed for developing the Thomson scattering diagnostic, they do have their own challenges due to the low laser energies needed to make unperturbed measurements of the plasma jet. Before measurements were made at the lower laser energy it was difficult to have any unperturbed measurement other than the velocity of the plasma. While later experiments were able to avoid this issue, we note that we are close to the threshold for heating of the plasma jet. Therefore, any future experiments that tries to measure physics of plasma jets, or plasmas in a similar parameter range, will have to keep this limit in mind to avoid heating the plasma and perturbing what is being measured.

Finally, Thomson scattering is demonstrating itself to be a very useful diagnostic technique at these high energy densities, and the author hopes he has

positioned the lab to be able to use this to make measurements on many different types of plasmas. So far, in addition to the research presented in this thesis, experiments with our Thomson scattering system have also been done on gas puff z-pinches (S. Rocco and N. Qi) [56, 55], bow-shock experiments (S. Bott-Suzuki), and reconnection experiments (J. Greenly). We hope that it will continue to be used with these experiments and new ones not yet designed.

APPENDIX A

CODE FOR THOMSON SCATTERING PROFILE

This section contains the code used to generate non-collisional Thomson scattering spectral profiles with a Maxwellian distribution function, and includes 3 different programs. This code was based on the Matlab code found in Appendix D of D. Froula's book [25]. These programs were written in python 3.5. The first program (*Thomson*) is used to calculate the power scattered as defined by Eq. 3.40, but does not account for the input laser power P_l or the scattering length, L . Into this program at least an array for the scattered wavelength must be passed. In addition, any plasma parameter or Thomson scattering set up parameter can be modified when the program is called. While this program is calculating the scattered power it must calculate $W(x) = \frac{-Z'(x)}{2}$, which is done by the second program (*Zprime5*). This program calculates W using the interpolation from a table that is generated by the third program, or by using a limit approximation when outside of the table's range. The third program (*wtable*) must be run only once, and creates tables to calculate $W(x)$, using the method discussed in Sec. 3.4. These three programs are all that are needed to generate a synthetic non-collisional Thomson scattering profile.

```
1 """
2 Thomson
3 This file calculates the Thomson scattering form factor and requires
  the tables generated by dwtable2.py and function Zprime.py. It
  computes the Thomson scattering, per unit scattering volume, per
  unit solid angle, per freq/2pi i.e.  $n_e * r_e^2 (1 - \sin^2(\text{sa}) * \sin^2(\text{dphi})) S(k, \omega) (1 + 2 * \omega / \omega_{\text{gape}})$ . This code calculates the form
  factor for Thomson scattering and is based off the matlab version
  in appendix D of D. Froula's book.
```

```

4
5 All the parameters into the function their default values and meaning
6
7     lamdas : Array of wavelength values to find scattered single at [
           cm]
8     Te=1 : electron temperature [KeV]
9     Ti=1 : ion temperature [KeV]
10    Z=np.array([5]) : ionization level of plasma
11    A=np.array([27]) : atomic number
12    fract=np.array([1]) : fraction of each ion species
13    ne=1e18 : plasma density [cm(-3)]
14    V=0 : fluid velocity along k [cm/s]
15    ud=0 : relative drift velocity between the electrons and ions
           along k [cm/s]
16    gamma=0 : the angle between k and the drift velocity ud [degrees]
17    sa=90 : scattering angle [degrees ]
18    dphi=90 : angle between the plane of polarization and the
           scattering plane [degrees]
19    lamdaL=526.5*10**-7 : # laser wavelength [cm]
20 """
21
22 import numpy as np
23 import Zprime as Zprime
24
25 Zprime=Zprime.Zprime5
26 maxud=1e7 # A value to prevent ud from going to big when fitting
27
28 # Loads the tables for W(x)
29 rdWT=np.load('rdWT2.npy');
30 idWT=np.load('idWT2.npy');
31
32 def Thomson (lamdas, Te=1,Ti=1,A=27,Z=5,fract=np.array([1]),ne=1e18,V

```

```

=0,ud=0,gamma=0,sa=90,dphi=90,lamdaL=526.5*10**-7):
33 # checks to make sure various parameters are reasonable, change
    if needed
34 if (Te>0 and Ti>0 and abs (ud)<maxud):
35     #basic quantities
36     C=2.99792458e10; # velocity of light cm/sec
37     Me=510.9896/C**2; # electron mass KeV/C^2
38     Mp=Me*1836.1; # proton Mass KeV/C^2
39     Mi=A*Mp; # ion mass
40     re=2.8179e-13; # classical electron radius cm
41     e=1.6e-19; # electron charge
42     Esq = Me*C**2*re; # sq of the electron charge KeV-cm
43     constants = np.sqrt(4*np.pi*Esq/Me); # sqrt(4*pi*e^2/Me)
44     sarad=sa*2*np.pi/360; # scattering angle in radians
45     dphirad = dphi*2*np.pi/360; # dphi is the angle between the
        plane of polarization and the scattering plane
46     gammarad = gamma*2*np.pi/360; # the angle between k and the
        drift velocity ud
47
48     #calculating k and omega vectors
49
50     omgpe=constants*np.sqrt(ne); # plasma frequency Rad/s
51     omgL=2*np.pi*C/lamdaL # laser frequency Rads/s
52     kL=1/C*np.sqrt(omgL**2-omgpe**2) # laser wavenumber in Rad/
        cm
53
54
55     omgs=2*np.pi*C/lamdas #scattered frequency rad/s
56     ks=1/C*np.sqrt(omgs**2-omgpe**2) #scattered wave-number rad/
        cm
57     k=np.sqrt(ks**2+kL**2-2*ks*kL*np.cos(sarad))
58     kdotv=k*V

```

```

59     omg = omgs - omgL; # omega change between scattered and laser
60     omgdop=omg - kdotv; # Doppler shift in frequency
61
62     # plasma parameters
63
64     # electrons
65     vTe=np.sqrt (Te/Me); # electron thermal velocity
66     klde=(vTe/omgpe)*k; #k times debye lenght
67     alpha=1/klde
68
69     # ions
70     Zbar = sum(Z*fract); # average z
71     vTi=np.sqrt (Ti/Mi); # ion thermal velocity
72
73     #calculating normalized phase velocity (xi's) for electrons
74     xd = ud/ (np.sqrt (2.)*vTe)*np.cos (gammarad); #drift velocity
75     xie=omgdop/(k*np.sqrt (2.)*vTe) - xd; # find xi based on
76     doppler shift
77     Zpe = Zprime (xie,rdWT,idWT); # find Z' (xie)
78
79     #calculating normalized phase velocity (xi's) for ions
80     xii=1/np.transpose ((np.sqrt (2.)*vTi))*(omgdop/k); #find xii
81     Zpi = Zprime (xii,rdWT,idWT); # find Z' (xii)
82
83     # Formfactor
84     #the distribution is assumed to be Maxwellian
85     Ae = np.exp (-xie**2)*((1+alpha**2*Zbar*Te/Ti*Zpi [0])**2+(
86         alpha**2*Zbar*Te/Ti*Zpi [1])**2)
87     Ai = Zbar*(Mi*Te/(Me*Ti))**(1/2.)*np.exp (-xii**2)*((alpha**2*
88         Zpe [0])**2+(alpha**2*Zpe [1])**2)
89     epslon2=(1+alpha**2*(Zpe [0]+Zbar*Te/Ti*Zpi [0]))**2+(alpha**2*
90         Zpe [1]+alpha**2*Zbar*Te/Ti*Zpi [1])**2

```

```

87     a=np.sqrt (2*Te/Me)
88     FF = 2*np.sqrt (np.pi) / (k*a) * (Ae/epslon2+Ai/epslon2);
89
90     r = (1+2*omgdop/omgL)*ne*(1-np.sin(sarad)**2*np.cos(dphirad)
          **2)*FF*re**2*1/(2*np.pi);#correction for [sXsXE]^2
91     formfactor = r
92
93     return formfactor
94     return -10e100+0*lamdas

```

```

1  """
2  Zprime
3  This function calculates  $W(\xi)=-Z'(\xi)/2$  for a given an array of
   normalized phase velocities ( $\xi$ ). For values of  $\xi$  between -15 and
   15 a table is used that can be generated by running the script
   below dwtable2. Outside of this range the asymptotic approximation
   is used.
4
5  This is based on Zprime.m in appendix D of D. Froula's book note the
   direction is switched in general as we are increasing in lambda (
   decreasing in k).
6  """
7  import numpy as np
8
9  # returns  $Rw(\xi)$  and  $Iw(\xi)$  as defined in 5.2.7-.8 in D. Froula's
   book.
10 def Zprime5 (xi,rdWT,idWT):
11
12     ai=[]
13     bi=[]
14     npts = np.size(xi);
15     #check if part of xi is out of range

```

```

16     if np.amin(xi)<-15 :
17         for i in range(1,npts):
18             if xi[npts-i]>-15:
19                 ai=npts-i
20                 break
21     if np.max(xi)>15 :
22         for i in range(0,npts):
23             if xi[i]<15:
24                 bi=i
25                 break
26
27     rZp=np.zeros(npts)
28     iZp=np.zeros(npts)
29
30     #find the real and imaginary parts of W based on interpolation or
31     #approximations if out of range
32     if ((np.size(ai)==0) and (np.size(bi)==0)) :
33         rZp=np.interp(xi,rdWT[0],rdWT[1]);
34         iZp=np.interp(xi,idWT[0],idWT[1]);
35     elif np.size(ai)==0 :
36         rZp[bi:npts]=np.interp(xi[bi:npts],rdWT[0],rdWT[1]);
37         iZp[bi:npts]=np.interp(xi[bi:npts],idWT[0],idWT[1]);
38         rZp[0:bi]= xi[0:bi]**(-2)/2*-1;
39         iZp[0:bi]=0.0;
40     elif np.size(bi)==0 :
41         rZp[0:ai+1]=np.interp(xi[0:ai+1],rdWT[0],rdWT[1]);
42         iZp[0:ai+1]=np.interp(xi[0:ai+1],idWT[0],idWT[1]);
43         rZp[ai+1:npts] = xi[ai+1:npts]**(-2)/2*-1;
44         iZp[ai+1:npts]=0.0;
45     else:
46         rZp[bi:ai+1]=np.interp(xi[bi:ai+1],rdWT[0],rdWT[1]);
47         iZp[bi:ai+1]=np.interp(xi[bi:ai+1],idWT[0],idWT[1]);

```

```

47     rZp[ai+1:npts]= xi[ai+1:npts]**(-2)/2*-1;
48     iZp[ai+1:npts]=0.0;
49     rZp[0:bi]= xi[0:bi]**(-2)/2*-1;
50     iZp[0:bi]=0.0;
51     Zp=np.zeros((2,npts))
52     Zp[0] = rZp;
53     Zp[1] = iZp;
54     return Zp

```

```

1
2 # wtable
3 # This file creates an ascii table W(xi) as a function of xi=omega/(
   k*vt)/sqrt(2). This only needs to be run once to create the files.
   It is based on 5.2.8 and 5.2.9 in D. Froula's book.
4 import numpy as np
5 import matplotlib.pyplot as plt
6
7 xmin=-15;
8 xmax=15;
9 xi=np.linspace(xmin,xmax,(xmax-xmin)/.01+1)
10 L=np.size(xi);
11 N=4; # determines the precision of the numerical calculation (reduce
      if your system has a memory issue)
12
13 IPV=np.zeros(L);
14 RP=np.zeros(L);
15
16 for i in range (0,L):
17
18     # defining how close to get to singularity
19     phi=.01*np.abs(xi[i])+1e-6;
20

```

```

21 # integration step size is N times smaller than phi
22 dz=phi/N;
23
24 # defining arrays symmetrically around xi
25 zm=np.arange(xi[i]-phi,ximin-1,-dz);
26 zp=np.arange(xi[i]+phi,ximax+1,dz);
27
28 # performing integrals
29 Ip=dz*np.sum(zp*np.exp(-zp**2)/(zp-xi[i]));
30 Im=dz*np.sum(zm*np.exp(-zm**2)/(zm-xi[i]));
31
32 IPV[i]=Ip+Im;
33
34 #evaluating real pole contribution
35 RP[i]=2*phi*(1-2*xi[i]**2);
36
37 # putting together W(xii)
38 dW=1/np.sqrt(np.pi)*(IPV+np.exp(-xi**2)*(RP-1j*np.pi*xi))
39
40 # forming table
41 rdWT=np.matrix([xi, np.real(dW)]);
42 idWT=np.matrix([xi, -1*np.imag(dW)]);
43 plt.plot(xi,np.real(dW))
44 plt.figure()
45 plt.plot(xi,-1*np.imag(dW))
46 plt.grid()
47 np.save('rdWT2',rdWT)
48 np.save('idWT2',idWT)

```

APPENDIX B

CODE FOR SUPER GAUSSIAN THOMSON SCATTERING PROFILE

This section contains the code used to generate non-collisional Thomson scattering spectral profiles with a super Gaussian electron distribution function and is based on Matlab code from D. Froula's group at LLE. These spectral profiles were generated using 3 programs that were written in python 3.5. They follow the same general form as the code discussed in Appendix A, but now with an extra parameter, m , that indicates how super Gaussian the profile is. As was discussed in Sec. 3.5.1, it ranges between 2 and 5 for laser heated plasmas. However, we primarily focused on the 2 to 3 range based on the calculations in the main text. As a reminder the super Gaussian distribution function is

$$f_{e0}(\mathbf{v}) = \frac{m}{4\pi(C_m v_{Te})^3 \Gamma(3/m)} \exp \left[- \left(\frac{v}{C_m v_{Te}} \right)^m \right], \quad (\text{B.1})$$

with

$$C_m = \frac{3\Gamma(3/m)}{\Gamma(5/m)}, \quad (\text{B.2})$$

where $\Gamma(x)$ is the gamma function. Since, for Thomson scattering, we are interested only in the velocity distribution along the \mathbf{k} vector, we will integrate this over two of the velocity dimensions, which results in

$$f_{e0}(v) = \frac{1}{2C_m v_{Te} \Gamma(3/m)} \Gamma_{\frac{2}{m}} \left(\left| \frac{v}{C_m v_{Te}} \right|^m \right), \quad (\text{B.3})$$

where $\Gamma_m(x)$ is the upper incomplete gamma function defined as

$$\Gamma_m(x) = \int_x^\infty t^{m-1} e^{-t} dt. \quad (\text{B.4})$$

This function is the standard one-dimensional Gaussian distribution function if $m = 2$, but then goes super Gaussian as m increases. The first program

(*Thomsonsuper*) is pretty similar to *Thomson* used in the previous appendix, but now has separate tables for the different $W(x)$'s of the ions and electrons. We should also note here that in this code *xie* is $\frac{\omega}{kv_{Te}}$ instead of $\frac{\omega}{\sqrt{2}kv_{Te}}$ because of how Eq. B.3 scales the velocities. In order to calculate $W(x)$ we again call *Zprime5*, which either interpolates the appropriate table from the *wtablesuper* program or uses the large value limit for $-Z'(x)/2$ (which is equivalent to the Gaussian version of this function) if $x > 8$. The *wtablesuper* program finds the solution for $W(x)$ based on the distribution function. As a reminder, the general form for $W(x)$ is

$$W(x) = v_{Te}^2 \int_{-\infty}^{\infty} \frac{\mathbf{k} \cdot \frac{\partial f_e(\mathbf{v})}{\partial \mathbf{v}}}{\omega - \mathbf{k} \cdot \mathbf{v} - i\gamma} d\mathbf{v}. \quad (\text{B.5})$$

This can be simplified by the fact that we can take the velocity along \mathbf{k} and that $\gamma = 0$. Using the one-dimensional velocity profile this gives

$$W(x) = -v_{Te}^2 \int_{-\infty}^{\infty} \frac{\frac{\partial f_e(v)}{\partial v}}{v - \omega/k} dv. \quad (\text{B.6})$$

Further simplifying this, saying that $z = v/v_{Te}$ and $x = \omega/kv_{Te}$, results in

$$W(x) = - \int_{-\infty}^{\infty} \frac{\frac{\partial v_{Te} f_e(z)}{\partial z}}{z - x} dz. \quad (\text{B.7})$$

This can be solved similarly to Eq. 3.112, as discussed in Sec. 3.4, by breaking it into 3 separate problems, but now with the numerator being $\frac{\partial v_{Te} f_e(z)}{\partial z}$ instead of $\frac{e^{-z^2}}{\sqrt{\pi}}$, as in Eq. 3.113. In the code the *Xe1NonMaxw* and *Xe2NonMaxw* variables are the results of the integration not near the pole. The final variable, *Xe3NonMaxw*, contains the integration over the pole. This again contains the traditional value for integration over the pole and a correction term from the Taylor expansion, since the code can only get so close to the pole. This code generates a set of tables based on the m parameter, which currently ranges from $m = 2$ to $m = 3$ in steps of 0.01. The tables generated from this program are then called by the *Thomsonsuper* program based on what value for m was desired to be fit. To

study a different electron distribution *fnorm2* would need to be changed into the appropriate 1D distribution function, and a Gaussian profile function would need to be created for the ions as that is currently being done by *fnorm2* with $m = 2$.

```

1 """
2 Thomsonsuper
3 This file calculates the Thomson scattering form factor for a super
   Gaussian electron distribution and requires the tables generated
   by wtablesuper.m and the function Zprime.m. It computes the
   Thomson scattering, per unit scattering volume, per unit solid
   angle, per freq/2pi i.e.  $n_e * r_e^2 (1 - \sin^2(\text{sa}) * \sin^2(\text{dphi})) S(k, \omega) (1 + 2 * \omega / \omega_{pe})$ .
4 This code calculates the form factor for Thomson scattering and is
   based off the matlab version in appendix D of D. Froula's book as
   well as a Matlab code received from D. Froula's group.
5
6
7 all the parameters into the function their default values and meaning
8
9 lamdas : Array of wavelength values to find scattered single at [
   cm]
10 Te=1 : electron temperature [KeV]
11 Ti=1 : ion temperature [KeV]
12 Z=np.array([5]) : ionization level of plasma
13 A=np.array([27]) : atomic number
14 fract=np.array([1]) : fraction of each ion species
15 ne=1e18 : plasma density [cm(-3)]
16 V=0 : fluid velocity along k [cm/s]
17 ud=0 : relative drift velocity between the electrons and ions
   along k [cm/s]
18 gamma=0 : the angle between k and the drift velocity ud [degrees]

```

```

19     sa=90 : scattering angle [degrees ]
20     dphi=90 : angle between the plane of polarization and the
                scattering plane [degrees]
21     lamdaL=526.5*10**-7 : # laser wavelength [cm]
22     m=2 : super Gaussian parameter
23     """
24
25     import numpy as np
26     import ZprimesuperG as Zprime
27     from scipy.special import gamma, gammaincc
28
29     Zprime=Zprime.Zprime5
30
31     def fnorm2(x,m):
32         Cm=np.sqrt(3*gamma(3/m)/gamma(5/m))
33         preterm=1/(2*Cm*gamma(3/m))
34         integral=gammaincc(2/m,np.abs(x/Cm)**(m))*gamma(2/m)
35
36         return preterm*integral
37
38     def Thomson (lamdas, Te=1,Ti=1,A=27,Z=5,fract=np.array([1]),ne=1e18,V
                =0,ud=0,gamma=0,sa=90,dphi=90,lamdaL=526.5*10**-7,m=2):
39         #chackes to make sure varous parmeters are resonable, change if
                needed
40         if(Te>0 and Ti>0):
41
42             rdWTe=np.load('rdWT2m{:.2f}.npy'.format(m))
43             idWTe=np.load('idWT2m{:.2f}.npy'.format(m))
44
45             rdWTi=np.load('rdWT2m2.00.npy')
46             idWTi=np.load('idWT2m2.00.npy')
47

```

```

48     #basic quantities
49     C=2.99792458e10; # velocity of light cm/sec
50     Me=510.9896/C**2; # electron mass KeV/C^2
51     Mp=Me*1836.1; # proton Mass KeV/C^2
52     Mi=A*Mp; # ion mass
53     re=2.8179e-13; # classical electron radius cm
54     e=1.6e-19; # electron charge
55     Esq = Me*C**2*re; # sq of the electron charge KeV-cm
56     constants = np.sqrt(4*np.pi*Esq/Me); # sqrt(4*pi*e^2/Me)
57     sarad=sa*2*np.pi/360; # scattering angle in radians
58     dphirad = dphi*2*np.pi/360; # dphi is the angle between the
        plane of polarization and the scattering plane
59     gammarad = gamma*2*np.pi/360; # the angle between k and the
        drift velocity ud
60
61     #calculating k and omega vectors
62
63     omgpe=constants*np.sqrt(ne); # plasma frequency Rad/s
64     omgL=2*np.pi*C/lamdaL # laser frequency Rads/s
65     kL=1/C*np.sqrt(omgL**2-omgpe**2) # laser wavenumber in Rad/
        cm
66
67     omgs=2*np.pi*C/lamdas #scattered freqcy rad/s
68     ks=1/C*np.sqrt(omgs**2-omgpe**2) #scattered wavenumber rad/cm
69     k=np.sqrt(ks**2+kL**2-2*ks*kL*np.cos(sarad))
70     kdotv=k*V
71     omg = omgs - omgL;# omega change between scattered and laser
72     omgdop=omg - kdotv; # doppler shif in frequency
73
74     # plasma parameters
75
76     # electrons

```

```

77     vTe=np.sqrt (Te/Me); # electron thermal velocity
78     klde=(vTe/omgpe)*k; #k times debye lenght
79     alpha=1/klde
80
81     # ions
82     Zbar = sum(Z*fract); # average z
83     vTi=np.sqrt (Ti/Mi); # ion thermal velocity
84
85     #calculating normalized phase velocity (xi's) for electrons
86     xd = ud/ (vTe)*np.cos (gammarad); #drift velocity
87     xie=omgdop/(k*vTe) - xd; # find xi bassed on doppler shift
88     Zpe = Zprime(xie,rdWTe,idWTe); # find Z'(xie)
89     chiE=alpha**2*(Zpe[0]+1j*Zpe[1])
90
91     #calculating normilized phase velcoity (xi's) for ions
92     xii=1/np.transpose((np.sqrt(2.)*vTi))*(omgdop/k); #find xii
93     Zpi = Zprime(xii,rdWTi,idWTi); # find Z'(xii)
94     chiI=alpha**2*Zbar*Te/Ti*(Zpi[0]+1j*Zpi[1])
95
96     epsilon=1+chiE+chiI
97
98     # Formfactor
99     # uses Maxwellian for the ion and super Gaussian for the
100         electrons
101     Se = 2*np.pi/k*np.abs(1-chiE/epsilon)**2*fnorm2(xie,m)/vTe
102     Si = 2*np.pi*Z/k*np.abs(chiE/epsilon)**2*fnorm2(xii*np.sqrt
103         (2),2)/vTi
104     FF = Se+Si
105
106     #zero out the laser wavelength to see just EPW
107     # for i in range (0,np.size(lamdas)):
108     #     if(np.abs(lamdas[i]-lamdaL)<1e-7):

```

```

107 #             FF[i]*=0
108
109     r = (1+2*omgdop/omgL)*ne*(1-np.sin(sarad)**2*np.cos(dphirad)
        **2)*FF*re**2;#correction for [sXsXE]^2
110     formfactor = r
111
112     return formfactor
113 return -10e100+0*lamdas

```

```

1 """
2 Zprime
3 This function calculates W(xi) for a given an array of normalized
  phase velocities (xi). For values of xi between -8 and 8 a table
  is used that can be generated by running the script below,
  wtablesuper. Outside of this range the asymptotic approximation is
  used.
4
5 This is based on Zprime.m in appendix D of D. Froula's book note the
  direction is switched in general as we are increasing in lambda (
  decreasing in k).
6
7 """
8 import numpy as np
9
10 def Zprime5 (xi,rdWT,idWT):
11
12     ai=[]
13     bi=[]
14     npts = np.size(xi);
15     #check if part of xi is out of ranngce
16     if np.amin(xi)<-8 :
17         for i in range(1,npts):

```

```

18         if xi[npts-i]>-8:
19             ai=npts-i
20             break
21 if np.max(xi)>8 :
22     for i in range(0,npts):
23         if xi[i]<8:
24             bi=i
25             break
26
27 rZp=np.zeros(npts)
28 iZp=np.zeros(npts)
29
30 #find the real and imaginary parts of Z basd on interpolation or
31     approximation if out of range
32 if ((np.size(ai)==0) and (np.size(bi)==0)) :
33     rZp=np.interp(xi,rdWT[0],rdWT[1]);
34     iZp=np.interp(xi,idWT[0],idWT[1]);
35 elif np.size(ai)==0 :
36     rZp[bi:npts]=np.interp(xi[bi:npts],rdWT[0],rdWT[1]);
37     iZp[bi:npts]=np.interp(xi[bi:npts],idWT[0],idWT[1]);
38     rZp[0:bi]= xi[0:bi]**(-2)/2*-1;
39     iZp[0:bi]=0.0;
40 elif np.size(bi)==0 :
41     rZp[0:ai+1]=np.interp(xi[0:ai+1],rdWT[0],rdWT[1]);
42     iZp[0:ai+1]=np.interp(xi[0:ai+1],idWT[0],idWT[1]);
43     rZp[ai+1:npts] = xi[ai+1:npts]**(-2)/2*-1;
44     iZp[ai+1:npts]=0.0;
45 else:
46     rZp[bi:ai+1]=np.interp(xi[bi:ai+1],rdWT[0],rdWT[1]);
47     iZp[bi:ai+1]=np.interp(xi[bi:ai+1],idWT[0],idWT[1]);
48     rZp[ai+1:npts]= xi[ai+1:npts]**(-2)/2*-1;
49     iZp[ai+1:npts]=0.0;

```

```

49     rZp[0:bi]= xi[0:bi]**(-2)/2*-1;
50     iZp[0:bi]=0.0;
51     Zp=np.zeros((2,npts))
52     Zp[0] = rZp;
53     Zp[1] = iZp;
54     return Zp

```

```

1
2 # wtablesuper
3 # This file creates an ascii table W(xi) as a function of xi=omega/(
      k*vt), when the electron distribution is allowed to be super
      Gaussian. This only needs to be run once to create the file.
4 # Note that this function file creates a range of tables based on the
      m parameter, and currently setup to create tables from m=2 to 3
      in 0.01 steps.
5 # This was based on Matlab code form D. Froula's group.
6
7 import numpy as np
8 import matplotlib.pyplot as plt
9 from scipy.special import gamma, gammaincc
10
11 ximin=-8.1;
12 ximax=8.1;
13 Delta=.001
14 h=.001
15 xie=np.arange(-8.01,8.02+2*h,h)
16 L=len(xie)-2
17 m=np.arange(2,3.01,.01) #range of m values to make tables for
18
19 #1D super Gaussian disturbution
20 def fnorm2(x,m):
21     Cm=np.sqrt(3*gamma(3/m)/gamma(5/m))

```

```

22     preterm=1/(2*Cm*gamma(3/m))
23     integral=gammaincc(2/m,np.abs(x/Cm)**(m))*gamma(2/m)
24
25     return preterm*integral
26
27 #makes a table for each value in the m array
28 for j in range(len(m)):
29     Xe1NonMaxw=np.zeros(L);
30     Xe2NonMaxw=np.zeros(L);
31
32     #calculates the integral away from the pole region
33     for i in range(0,L):
34
35         lowerArray=np.arange(xie[i],ximin,-Delta)
36         lowerArray=np.flip(lowerArray)
37         upperArray=np.arange(xie[i]+Delta,ximax+Delta,Delta)
38
39         dfdv_Low=np.diff(fnorm2(lowerArray,m[j]))/(Delta*(lowerArray
40            [:-1]-xie[i]))
41         dfdv_Upp=np.diff(fnorm2(upperArray,m[j]))/(Delta*(upperArray
42            [:-1]-xie[i]))
43
44         Xe1NonMaxw[i]=Delta*np.sum(dfdv_Low)
45         Xe2NonMaxw[i]=Delta*np.sum(dfdv_Upp)
46
47     #the integral part near the pole
48     Xe3NonMaxw=-1*(2*Delta*np.diff(np.diff(fnorm2(xie,m[j]))/h)/h-np.
49         pi*1j*np.diff(fnorm2(xie[:-1],m[j]))/h)
50
51     ## putting together W
52     dW=-1*(Xe1NonMaxw+Xe2NonMaxw+Xe3NonMaxw)

```

```
51     ## forming table
52     rdWT=np.matrix([xie[:-2], np.real(dW)]);
53     idWT=np.matrix([xie[:-2], np.imag(dW)]);
54
55     #saves the tables if you need more percision than 0.01 steps in m
        need to change the naming scheme
56     np.save('rdWT2m{:.2f}'.format(m[j]),rdWT)
57     np.save('idWT2m{:.2f}'.format(m[j]),idWT)
```

BIBLIOGRAPHY

- [1] J. T. Banasek, T. Byvank, S. V. R. Rocco, W. M. Potter, B. R. Kusse, and D. A. Hammer. Time-Resolved Thomson Scattering on Laboratory Plasma Jets. *IEEE Transactions on Plasma Science*, pages 1–5, 2018.
- [2] J. T. Banasek, S. V. R. Rocco, W. M. Potter, T. Byvank, B. R. Kusse, and D. A. Hammer. Multi-angle multi-pulse time-resolved Thomson scattering on laboratory plasma jets. *Review of Scientific Instruments*, 89(10):10C109, 2018.
- [3] N G. Basov and O. N. Krokhin. Conditions for Heating up of a Plasma by the Raditation from an Optical Generator. *J. Exptl. Theoret. Phys. (U.S.S.R.)*, 19(46):171–175, 1964.
- [4] Paul M. Bellan. *Fundamentals of Plasma Physics*. Cambridge University Press, New York, 2006.
- [5] I. C. Blesener. *Initiation, ablation, precursor formation, and instability analysis of thin foil copper liner Z-pinch*s. PhD thesis, Cornell University, 2012.
- [6] S. I. Braginskii. Transport Processes in a Plasma. *Reviews of plasma physics*, 1:205–311, 1965.
- [7] A. V. Brantov, V. Yu. Bychenkov, and W. Rozmus. Electrostatic Response of a Two-Component Plasma with Coulomb Collisions. *Physical Review Letters*, 108(20):205001, may 2012.
- [8] T. Byvank, J. T. Banasek, W. M. Potter, J. B. Greenly, C. E. Seyler, and B. R. Kusse. Applied axial magnetic field effects on laboratory plasma jets: Density hollowing, field compression, and azimuthal rotation. *Physics of Plasmas*, 24(12):122701, 2017.
- [9] T. Byvank, J. Chang, W. M. Potter, C. E. Seyler, and B. R. Kusse. Extended Magnetohydrodynamic Plasma Jets With External Magnetic Fields. *IEEE Transactions on Plasma Science*, 44(4):638–642, apr 2016.
- [10] Tom Byvank. *Applied Axial Magnetic Field Effects on Extended Magnetohydrodynamics Laboratory Plasma Jets : Experiments and Simulations*. PhD thesis, Cornell University, 2018.
- [11] Tom Byvank, Nathaniel Hamlin, Levon Atoyian, Charles E. Seyler, and Bruce R. Kusse. Plasma Jet Formation Disruption From a Critical App-

- lied Uniform Axial Magnetic Field. *IEEE Transactions on Plasma Science*, 47(7):3204–3213, jul 2019.
- [12] David Chalenski. *a Parametric Study of Polarity , Contact and Current Risetime Effects on Wire Array Z-Pinches*. PhD thesis, Cornell Univeritsy, 2010.
- [13] H.-K. Chung, M.H. Chen, W.L. Morgan, Y. Ralchenko, and R.W. Lee. FLYCHK: Generalized population kinetics and spectral model for rapid spectroscopic analysis for all elements. *High Energy Density Physics*, 1(1):3–12, 2005.
- [14] Cameron J. Dasch. One-dimensional tomography: a comparison of Abel, onion-peeling, and filtered backprojection methods. *Applied Optics*, 31(8):1146, mar 1992.
- [15] John Dawson and Carl Oberman. High-Frequency Conductivity and the Emission and Absorption Coefficients of a Fully Ionized Plasma. *Physics of Fluids*, 517(5):517, 1962.
- [16] John M. Dawson. On the Production of Plasma by Giant Pulse Lasers. *Physics of Fluids*, 7(7):981, 1964.
- [17] A. W. DeSilva and G. C. Goldenbaum. *Plasma diagnostics by light scattering*, volume 9. Academic Press, New York, 1970.
- [18] J. P. Dougherty and D. T. Farley. A Theory of incoherent scattering of radio waves by a plasma. *Proceedings of the Royal Society A*, 259(1296):79–99, nov 1960.
- [19] R. Paul Drake. *High-Energy-Density Physics*. Shock Wave and High Pressure Phenomena. Springer, Berlin, 2006.
- [20] D. E. Evans and J. Katzenstein. Laser light scattering in laboratory plasmas. *Reports on Progress in Physics*, 32:207–271, 1969.
- [21] R. K. Follett, J. A. Delettrez, D. H. Edgell, V. N. Goncharov, R. J. Hennen, J. Katz, D. T. Michel, J. F. Myatt, J. Shaw, A. A. Solodov, C. Stoeckl, B. Yaakobi, and D. H. Froula. Two-Plasmon Decay Mitigation in Direct-Drive Inertial-Confinement-Fusion Experiments Using Multilayer Targets. *Physical Review Letters*, 116(15):155002, apr 2016.

- [22] R. K. Follett, J. A. Delettrez, D. H. Edgell, R. J. Henchen, J. Katz, J. F. Myatt, and D. H. Froula. Plasma characterization using ultraviolet Thomson scattering from ion-acoustic and electron plasma waves (invited). *Review of Scientific Instruments*, 87(11):11E401, nov 2016.
- [23] B. D. Fried and S. D. Conte. *The Plasma Dispersion Function*. Academic Press, New York, 1961.
- [24] D. Froula, P. Davis, L. Divol, J. Ross, N. Meezan, D. Price, S. Glenzer, and C. Rousseaux. Measurement of the Dispersion of Thermal Ion-Acoustic Fluctuations in High-Temperature Laser Plasmas Using Multiple-Wavelength Thomson Scattering. *Physical Review Letters*, 95(19):195005, nov 2005.
- [25] Dustin Froula, Siegfried H. Glenzer, Neville C. Jr. Luhmann, and John Sheffield. *Plasma Scattering of Electromagnetic Radiation: Theory and Measurement Techniques*. Elsevier Ltd, Amsterdam, second edition, 2011.
- [26] S. H. Glenzer, W. E. Alley, K. G. Estabrook, J. S. De Groot, M. G. Haines, J. H. Hammer, J.-P. Jadaud, B. J. MacGowan, J. D. Moody, W. Rozmus, L. J. Suter, T. L. Weiland, E. A. Williams, J. S. De Groot, M. G. Haines, J. H. Hammer, J.-P. Jadaud, B. J. MacGowan, J. D. Moody, W. Rozmus, L. J. Suter, T. L. Weiland, and E. A. Williams. Thomson scattering from laser plasmas. *Physics of Plasmas*, 6(5):2117, may 1999.
- [27] S. H. Glenzer, W. Rozmus, B. J. MacGowan, K. G. Estabrook, J. D. De Groot, G. B. Zimmerman, H. A. Baldis, J. A. Harte, R. W. Lee, E. A. Williams, and B. G. Wilson. Thomson Scattering from High- Z Laser-Produced Plasmas. *Physical Review Letters*, 82(1):97–100, jan 1999.
- [28] P.-A. Gourdain, I. C. Blesener, J. B. Greenly, D. A. Hammer, P. F. Knapp, B. R. Kusse, and P. C. Schrafel. Initial experiments using radial foils on the Cornell Beam Research Accelerator pulsed power generator. *Physics of Plasmas*, 17(1):012706, jan 2010.
- [29] P.-A. Gourdain, J. B. Greenly, D. A. Hammer, P. F. Knapp, B. R. Kusse, S. A. Pikuz, P. C. Schrafel, and T. C. Shelkovenko. The Impact of Cathode Diameter on Radial Foil Explosions. *IEEE Transactions on Plasma Science*, 38(12):3363–3369, dec 2010.
- [30] P.-A. Gourdain and C. E. Seyler. Impact of the Hall Effect on High-Energy-Density Plasma Jets. *Physical Review Letters*, 110:015002, 2013.

- [31] P.-A. Gourdain and C. E. Seyler. Modeling of strongly collimated jets produced by high energy density plasmas on COBRA. *Plasma Physics and Controlled Fusion Plasma Phys. Control. Fusion*, 56:35002–9, 2014.
- [32] P.-A. Gourdain, C. E. Seyler, L. Atoyán, J. B. Greenly, D. A. Hammer, B. R. Kusse, S. A. Pikuz, W. M. Potter, P. C. Schrafel, and T. A. Shelkovenko. The impact of Hall physics on magnetized high energy density plasma jets. *Physics of Plasmas*, 21:056307, 2014.
- [33] J. B. Greenly, J. D. Douglas, D. A. Hammer, B. R. Kusse, S. C. Glidden, and H. D. Sanders. A 1 MA, variable risetime pulse generator for high energy density plasma research. *The Review of scientific instruments*, 79(7):073501, jul 2008.
- [34] Jack D. Hare, James MacDonald, Simon Bland, Jakub Dranczewski, Jack Halliday, Sergey V Lebedev, Lee Suttle, Eleanor Tubman, and Wojciech Rozmus. Two-colour interferometry and Thomson scattering measurements of a plasma gun. *Plasma Physics and Controlled Fusion*, may 2019.
- [35] R. J. Henchen, M. Sherlock, W. Rozmus, J. Katz, D. Cao, J. P. Palastro, and D. H. Froula. Observation of Nonlocal Heat Flux Using Thomson Scattering. *Physical Review Letters*, 121:125001, 2018.
- [36] R. J. Henchen, M. Sherlock, W. Rozmus, J. Katz, P. E. Masson-Laborde, D. Cao, J. P. Palastro, and D. H. Froula. Measuring heat flux from collective Thomson scattering with non-Maxwellian distribution functions. *Physics of Plasmas*, 26:32104, 2019.
- [37] C. L. Hoyt. *Scattering Diagnostic Development Based on a Titanium Hybrid X-Pinch X-Ray Source*. PhD thesis, Cornell University, 2015.
- [38] S. C. Hsu, T. J. Awe, S. Brockington, A. Case, J. T. Cassibry, G. Kagan, S. J. Messer, M. Stanic, X. Tang, D. R. Welch, and F. D. Witherspoon. Spherically Imploding Plasma Liners as a Standoff Driver for Magnetoinertial Fusion. *IEEE Transactions on Plasma Science*, 40(5):1287–1298, may 2012.
- [39] I. H. Hutchinson. *Principles of Plasma Diagnostics*. Cambridge University Press, Cambridge, 2002.
- [40] John D. Jackson. *Classical Electrodynamics*. John Wiley & Son, inc, Hoboken, 3rd edition, 1999.

- [41] T. W. Johnston and J. M. Dawson. Correct values for high-frequency power absorption by inverse bremsstrahlung in plasmas. *The Physics of Fluids*, 16:722, 1973.
- [42] J. Katz, R. Boni, C. Sorce, R. Follett, M. J. Shoup, and D. H. Froula. A reflective optical transport system for ultraviolet Thomson scattering from electron plasma waves on OMEGA. *Review of Scientific Instruments*, 83(10):10E349, 2012.
- [43] A. Bruce Langdon. Nonlinear Inverse Bremsstrahlung and Heated-Electron Distributions. *Physical Review Letters*, 44(9):575–579, mar 1980.
- [44] J. M. Lerner and A. Thevenon. "Optics of Spectroscopy Tutorial" <http://www.horiba.com/us/en/scientific/products/optics-tutorial/>.
- [45] John Lindl, Otto Landen, John Edwards, Ed Moses, and NIC Team. Review of the National Ignition Campaign 2009-2012. *Physics of Plasmas*, 21(2):020501, feb 2014.
- [46] Matthew Ryan Martin. *Generalized Ohm's Law at the Plasma-Vacuum Interface*. PhD thesis, Cornell University, 2010.
- [47] J. P. Matte, M. Lamoureux, C. Moller, R. Y. Yin, J. Delettrez, J. Virmont, and T. W. Johnston. Non-Maxwellian electron distributions and continuum X-ray emission in inverse Bremsstrahlung heated plasmas. *Plasma Physics and Controlled Fusion*, 30(12):1665–1689, nov 1988.
- [48] Claire Ellen Max. Strong self-focusing due to the ponderomotive force in plasmas. *The Physics of Fluids*, 19:74, 1976.
- [49] D S Montgomery and R P Johnson. Design considerations for fiber-coupled streaked optical spectroscopy. *Review of Scientific Instruments*, 72(1):979, 2001.
- [50] J. F. Myatt, W. Rozmus, V. Yu. Bychenkov, and V. T. Tikhonchuk. Thomson scattering from ion acoustic waves in laser plasmas. *Physical Review E*, 57(3):3383–3391, mar 1998.
- [51] R. Pasqualotto, A. Sardella, A. Intravaia, and L. Marrelli. Improved performance of the Thomson scattering system in RFX. *Review of Scientific Instruments*, 70:1416, 1999.

- [52] N. J. Peacock, D. C. Robinson, M. J. Forrest, P. D. Wilcock, and V. V. Sannikov. Measurement of the Electron Temperature by Thomson Scattering in Tokamak T3. *Nature*, 224(5218):488–490, nov 1969.
- [53] G. J. Pert. Inverse bremsstrahlung in strong radiation fields at low temperatures. *Physical Review E*, 51(5):4778, 1995.
- [54] S. A. Pikuz, V. M. Romanova, N. V. Baryshnikov, Min Hu, B. R. Kusse, D. B. Sinars, T. A. Shelkovenko, and D. A. Hammer. A simple air wedge shearing interferometer for studying exploding wires. *Review of Scientific Instruments*, 72(1):1098–1100, jan 2001.
- [55] S. V. R. Rocco, J. T. Banasek, W.M. Potter, and D. A. Hammer. Time-Resolved Thomson Scattering on Gas-Puff Z-Pinch Plasmas at Pinch Time. *IEEE Transactions on Plasma Science*, pages 1–6, 2018.
- [56] Sophia V. R. Rocco, Jacob T. Banasek, William M. Potter, and David A. Hammer. Time-resolved and multiple-angle Thomson scattering on gas-puff Z-Pinch plasmas at pinch time. *Review of Scientific Instruments*, 89(10):10C117, 2018.
- [57] J. S. Ross, P. Datte, L. Divol, J. Galbraith, D. H. Froula, S. H. Glenzer, B. Hatch, J. Katz, J. Kilkenny, O. Landen, A. M. Manuel, W. Molander, D. S. Montgomery, J. D. Moody, G. Swadling, and J. Weaver. Simulated performance of the optical Thomson scattering diagnostic designed for the National Ignition Facility. *Review of Scientific Instruments*, 87(11):11E510, nov 2016.
- [58] J. S. Ross, D. H. Froula, A. J. Mackinnon, C. Sorce, N. Meezan, S. H. Glenzer, W. Armstrong, R. Bahr, R. Huff, and K. Thorp. Implementation of imaging Thomson scattering on the Omega Laser. *Review of Scientific Instruments*, 77(10):10E520, 2006.
- [59] J. S. Ross, S. H. Glenzer, J. P. Palastro, B. B. Pollock, D. Price, G. R. Tynan, and D. H. Froula. Thomson-scattering measurements in the collective and noncollective regimes in laser produced plasmas (invited). *Review of Scientific Instruments*, 81(10):10D523, oct 2010.
- [60] W Rozmus, A Brantov, C Fortmann-Grote, V Yu Bychenkov, and S Glenzer. Electrostatic fluctuations in collisional plasmas. *Physical Review E*, 96:043207, 2017.
- [61] E. E. Salpeter. Electron Density Fluctuations in a Plasma. *Physical Review*, 120(5):1528–1535, dec 1960.

- [62] Peter Schrafel, Kate Bell, John Greenly, Charles Seyler, and Bruce Kusse. Magnetized laboratory plasma jets: Experiment and simulation. *Physical Review E*, 91(1):013110, jan 2015.
- [63] C. E. Seyler and M. R. Martin. Relaxation model for extended magnetohydrodynamics: Comparison to magnetohydrodynamics for dense Z-pinches. *Physics of Plasmas*, 18(1):012703, jan 2011.
- [64] S. A. Slutz, M. C. Herrmann, R. A. Vesey, A. B. Sefkow, D. B. Sinars, D. C. Rovang, K. J. Peterson, and M. E. Cuneo. Pulsed-power-driven cylindrical liner implosions of laser preheated fuel magnetized with an axial field. *Physics of Plasmas*, 17(5):056303, may 2010.
- [65] F. Suzuki-Vidal, M. Bocchi, S. V. Lebedev, G. F. Swadling, G. Burdiak, S. N. Bland, P. De Grouchy, G. N. Hall, A. J. Harvey-Thompson, E. Khoory, S. Patankar, L. Pickworth, J. Skidmore, R. Smith, J. P. Chittenden, M. Krishnan, R. E. Madden, K. Wilson-Elliot, A. Ciardi, and A. Frank. Interaction of a supersonic, radiatively cooled plasma jet with an ambient medium. *Physics of Plasmas*, 19(2):022708, feb 2012.
- [66] G. F. Swadling, S. V. Lebedev, G. N. Hall, S. Patankar, N. H. Stewart, R. A. Smith, A. J. Harvey-Thompson, G. C. Burdiak, P. de Grouchy, J. Skidmore, L. Suttle, F. Suzuki-Vidal, S. N. Bland, K. H. Kwek, L. Pickworth, M. Bennett, J. D. Hare, W. Rozmus, and J. Yuan. Diagnosing collisions of magnetized, high energy density plasma flows using a combination of collective Thomson scattering, Faraday rotation, and interferometry (invited). *Review of Scientific Instruments*, 85(11):11E502, nov 2014.
- [67] B. A. Trubnikov. Particle Interactions in a Fully Ionized Plasma. In *Reviews of Plasma Physics*, page 105. Consultants Bureau, New York, 1965.
- [68] Eric W. Weisstein. "Gamma Function." From MathWorld—A Wolfram Web Resource. <http://mathworld.wolfram.com/GammaFunction.html>.
- [69] Yuhong Xu. A general comparison between tokamak and stellarator plasmas. *Matter and Radiation at Extremes*, 1(4):192–200, jul 2016.
- [70] Jian Zheng, C. X. Yu, and Z. J. Zheng. Effects of non-Maxwellian (super-Gaussian) electron velocity distribution on the spectrum of Thomson scattering. *Physics of Plasmas*, 4:2736, 1997.
- [71] Jian Zheng, C. X. Yu, and Z. J. Zheng. The dynamic form factor for ion-collisional plasmas. *Physics of Plasmas*, 6(2):435, 1999.